Universidade de São Paulo
Instituto de Química de São Carlos

Ricardo Sgarbi de Moraes

Metal-N-C Electrocatalysts: Physical and Chemical Aspects on the Activity and Durability towards Oxygen Reduction Reaction

Eletrocatalisadores Metal-N-C: Aspectos Físicos e Químicos na Atividade e Durabilidade frente à Reação de Redução do Oxigênio

São Carlos

2020

Ricardo Sgarbi de Moraes

Metal-N-C Electrocatalysts: Physical and Chemical Aspects on the Activity and Durability towards Oxygen Reduction Reaction

Eletrocatalisadores Metal-N-C: Aspectos Físicos e Químicos na Atividade e Durabilidade frente à Reação de Redução do Oxigênio

Thesis presented to the Graduate Program in Chemistry at the Instituto de Química de São Carlos (Universidade de São Paulo) to obtain the degree of Doctor in Science

Concentration area: Physical Chemistry

Supervisor: Prof. Dr. Edson Antonio Ticianelli

Exemplar revisado

O exemplar original encontra-se em
acervo reservado na Biblioteca do IQSC-USP

São Carlos
2020

To my parents, Neusa and José Luiz,
and my daughter, Lara.

Acknowledgments

I acknowledge my parents Neusa and José Luiz, my daughter Lara, my brothers Rodrigo, Fábio and Fernando for their support and encouragement.

I express my gratitude to my supervisor Professor Edson Antonio Ticianelli, for his guidance, disposal, constructive criticism and for the opportunity to work at Electrochemistry Group. Also, I am thankful for the Coordenação de Aperfeiçoamento de Pessoal de Nível Superior (CAPES), Brazil (grant number: 1614344), CAPES/COFECUB program (grant numbers: 88887-187755/2018-00 and Ph-C 914/18) and the São Paulo State Research Foundation (FAPESP – grant number: 2013/16930-7).

Je suis trés reconnaissaint le chercheur Frédéric Maillard qui m'ai accueilli et guidé parfaitement pendant un an à son laboratoire (Laboratoire d'Electrochimie et de Physico-chimie des Matériaux et des Interfaces – LEPMI). Aussi pour ton amitié au terrain de foot, bar, stade, parc où meme au laboratoire. Je remercie Marian Chatenet et Frédéric Jaouen (IGCM - Institut Charles Gerhardt Montpellier) pour notre beau travail ensemble et Laetitia Dubau pour de l'aide en microscopie.

Je remercie la postdoctorante Kavita Kumar pour sa collaboration em ma thesis et pour la amitié quotidienne y compris en boire un verre. Je remercie mes potes Eris et Victor ! Aussi mes colleagues du LEPMI, Monsieur Sofyane, César, Marion, Clémence, Marine, Guillaume, Vincent, Sedik, Youcef, Delphine, Vivien, François, Raphael, Fabien, Juan et Marie.

Je remercie les bons et vainqueur temps avec l'équipe de foot du LEPMI. Nous somme champions du Tournois Interlabo !

J'adresse mes remerciements mon coloc Otto pour l'amitié et bons moments dans presque toute la France.

I acknowledge the laboratory professionals involved in my daily routine at Electrochemistry Group and *Instituto de Química de São Carlos* (*IQSC*): Mauro Fernandes, Jonas Garcia, Gabriel da Silva, Valdecir Paganin, Paulo Beatrice and Marcelo Calegaro.

I am very thankful to *IQSC* coworkers and friends: Amaury, Wanderson, Carlos, Enrique, James, Elenice, Diego, Carlos André, Nicolas, Anelisse, Nelson, Thiago, Rodrigo, Rafael, Ana, Bott, Maykon, Adriana, Marcelo, Alfredo, Gabriel, Paula, Rapher, Loriz, Thairo and Pedro.

I am very grateful to my flatmates/friends: Arthur, Rodrigo, Matheus, Daniel and Raul for the great adventures, good talks, barbecues, weekends and many good stories at 304 apartment.

Contents

Abstract

Metal-N-C electrocatalysts (where the Metal is Fe or Co) have been investigated for mitigating the dependence on platinum-group-metals (PGM), when catalyzing the oxygen reduction reaction (ORR) in acidic or alkaline for fuel cell technologies. This thesis relates the activity, durability and poisoning resistance with the physicochemical properties of such electrocatalysts with iron and cobalt. The investigated materials contain two main active groups: (i) atomically-dispersed metals attached to nitrogen-doped carbon networks (M-N_xC_y active sites) and (ii) metal nanoparticles encased on nitrogen-doped carbon shells (M@N-C active sites). Regarding the activity, Fe-N-C is more active than the Co-based catalysts, either at low and high pHs. Fe-N_xC_y sites present the highest ORR activity in acid media, amplified by an adequate energy binding between the metallic center and oxygenated reaction intermediates. In contrast, Fe@N-C core-shell sites present maximum ORR mass activity in alkaline media, promoted by a synergistic effect involving catalyst particles with metallic iron in the core and nitrogen-doped carbon in the shell. The durabilities tests have shown two main degrading processes that may occur on the catalyst: (i) oxygenated and nitrogen functional groups interconversion and/or oxidation and (ii) demetallation of the metallic center. Iron nanoparticulated catalyst centers undergo more severe carbon degradation and nitrogen/oxygenated functional groups interconversion (and/or oxidation) than the atomically dispersed iron centers. But, this latter catalyst losses metal severely, which is re-deposited growing *in situ* Fe-based nanoparticles after accelerated stressing tests under O_2 atmosphere, more at 25 °C than at 60 °C. As a consequence, the atomically dispersed iron-based nanoparticles drop the ORR mass activities less intensely. Further, the atomically dispersed Fe- and Co-containing electrocatalysts have better BH_4^--tolerance than bare Fe and Co nanoparticles. The atomically dispersed iron electrocatalysts, the material with the highest micropores area, present slight advantage of ORR mass activity in the presence of BH_4^- anions. Finally, these features place the atomically-dispersed iron as a promising candidate for the investigations in direct borohydride fuel cell (DBFC) and as an excellent candidate for application in the cathode of anion-exchange membrane fuel cell (AEMFC).

Keywords: Metal-nitrogen–doped carbons (M–N–C) catalyst, Fe-N-C, Co-N-C, Oxygen reduction reaction, Anion-exchange membrane fuel cell

Resumo

Eletrocatalisadores Metal-N-C (Metal: Fe ou Co) têm sido investigados para a diminuição da dependência de metais do grupo da platina na catálise da reação de redução de oxigênio (RRO) em células a combustível sob condições ácida e alcalinas. Esta tese relaciona as propriedades físico-químicas destes eletrocatalisadores com a atividade, durabilidade e resistência ao envenamento. Os materiais investigados consistem de dois principais grupos: (i) átomos metálicos dispersos em uma matriz de carbono dopado com nitrogênio (sítios ativos: $M\text{-}N_xC_y$) e (ii) nanopartículas metálicas encapsuladas por uma camada de carbono dopado com nitrogênio (sítios ativos: M@N-C). Ao considerar a atividade, os eletrocatalisadores Fe-N-C são os mais ativos em baixo e alto valores de pH. Sítios ativos $Fe\text{-}N_xC_y$ possuem as maiores atividades frente à RRO em meio ácido, sendo amplificadas pelas energias de ligação entre entre o centro metálico e os intermediários oxigenados. De maneira oposta, sítios Fe@N-C alcançam altas atividades mássicas em meio alcalino, favorecido pelo efeito sinérgico entre as nanopartículas metálicas e o envólucro de carbono dopado com nitrogênio. Os testes de durabilidade mostraram dois principais processos de degradação que podem ocorrer no catalisador: (i) a interconversão e/ou oxidação dos grupos funcionais oxigenados e nitrogenados e (ii) a demetalação dos centros metálicos. O catalisador de ferro nanoparticulado sofre uma mais severa oxidação e/ou interconversão dos grupos funcionais nitrogenados e oxigenados que a dispersão atômica do ferro. No entanto, este último catalisador perde maior quantidade de metal, o qual é re-depositado formando nanopartículas à base de ferro *in situ* em maior proporção após testes de degradação acelerada a 25 °C se comparado à 60 °C sob atmosfera de O_2. Assim, o ferro atomicamente disperso com nanopartículas à base de ferro sofre uma diminuição na atividade mássica da RRO menos intensa. Além disso, eletrocatalisadores atomicamente dispersos contendo Fe e Co apresentam maior tolerância aos íons BH_4^- em comparação às respectivas nanopartículas metálicas encapsuladas. A tolerância aos íons BH_4^- é maximizada pela presença do centro metálico de ferro e pela maior área dos microporos do catalisador atomicamente disperso. Estas características colocam o eletrocatalisador de ferro disperso atomicamente como um promissor candidato para a investigação numa célula a combustível de borohidreto direta (*DBFC*) e um excelente candidato a aplicação em célula a combustível alcalina de troca aniônica (*AEMFC*).

Palavras-chave: Catalisador metal carbon dopado com nitrogênio (M-N-C), Fe-N-C, Co-N-C, Reação de redução do oxigênio, Célula a combustível alcalina de troca aniônica

Preamble

This thesis consists of studies accomplished in the University of São Paulo (São Carlos Institute of Chemistry – IQSC - Electrochemistry Group) and University of Grenoble Alpes (*Laboratoire d'Electrochimie et de Physico-chimie des Matériaux et des Interfaces – LEPMI*) and contains most of the experimental results that were obtained and analyzed during three years.

Focusing on the replacement of platinum-group metals for cathodic materials in fuel cell dispositive, this thesis studied four different catalysts based on the model Metal-N-C (where Metal is Fe or Co). Results were grouped into three chapters consisting of the investigations of the activity, durability and poisoning of the electrocatalysts for the oxygen reduction reaction (ORR). Briefly, Chapter 1 shows the pH effect on the ORR electrocatalysis using synthesized catalysts featuring M-N_xC_y or M@N-C active sites. In Chapter 2, the electrocatalysts were evaluated against their corrosion resistance under alkaline degradant conditions, simulating load cycles of alkaline electrolyte membrane fuel cell (AEMFC) cathodes. Chapter 3, displays the tolerance of the electrocatalysts towards the presence of $NaBH_4$ in promoting the ORR.

All chapters involve the establishment of correlations between activity, durability and poisoning resistance and the catalysts' physicochemical properties. To access these physicochemical properties the following techniques were considered: X-ray absorption spectroscopy (XAS), Raman spectroscopy, ^{57}Fe Mössbauer spectroscopy, transmission electron microscopy (TEM), X-ray diffraction (XRD), Brunauer–Emmett–Teller (BET) theory, inductively coupled plasma-mass-spectrometry (ICP-MS), energy-dispersive X-ray spectroscopy (X-EDS) and X-ray photoelectron spectroscopy (XPS). As electrochemical techniques, cyclic voltammetry (CV), rotating disk electrode (RDE) and rotating ring-disk electrode (RRDE) were employed.

Chapter 1

Oxygen Reduction Reaction Mechanism and Kinetics on M-N_xC_y and M@N-C Active Sites Present in Model M-N-C Catalysts under Alkaline and Acidic Conditions

This chapter has been adapted with permission from Springer Nature (Journal of Solid State Electrochemistry, 2019, DOI: 10.1007/s10008-019-04436-w)

1.1 Introduction

The oxygen reduction reaction (ORR) electrocatalysis plays a key role in the development of sustainable and clean energy technologies, particularly when related to energy storage and conversion devices. Among these devices, fuel cells that convert the chemical energy of a fuel into electricity rely on air reducing cathodes. Depending on the choice of electrolyte, fuel cells are operated in a broad range of pH, from acidic to neutral and alkaline conditions, as represented by the proton exchange membrane (PEMFC) and microbial (MFC) and alkaline exchange membrane (AEMFC) fuel cells, respectively[1, 2]. Catalysts based on platinum (Pt) and platinum-group metals (PGM) reach high activity and selectivity for ORR to water in acidic conditions [3], in the same way as several PGM catalysts exhibit good performances for ORR, with relative tolerance to fuel contamination, in alkaline media [4]. However, the high cost and the CO poisoning of PGM-based catalysts have been pointed out as unsolved problems for the wide-scale implementation of these devices [2, 5, 6].

Two classes of PGM-free catalysts have been widely investigated focusing on eliminating PGM for the ORR electrocatalysis: (i) metal-free carbon-nitrogen (N-C) composites and (ii) transition metal-incorporated carbon-nitrogen matrices (referred to as M-N-C, with M = Fe or Co) [7–9]. Recently, an extraordinary expectation towards the use of M-N-C catalysts for ORR electrocatalysis has grown, due to the recent and rapid progress in the field over the past 10 years, regarding improvement in the electrocatalytic activity, power performance, tolerance to CO, and, although more challenging, improvements in stability and durability as well,observed in both high and low pH conditions [10–14]. However, a better understanding of the nature and the number of the different active sites in pyrolyzed M-N-C materials and correlations with the ORR electrocatalysis at different pH values is still required for an optimized choice of such catalysts as a function of the operating conditions, in particular regarding the operating pH of the fuel cell device.

When the pH changes from acidic (PEMFC, pH~1) to alkaline (AEMFC, pH~13) conditions, the overall four-electron O_2 reduction changes from $O_2 + 4H^+ + 4\ e^- \rightarrow 2\ H_2O$ to $O_2 + 2\ H_2O + 4\ e^- \rightarrow 4\ OH^-$, in acid and alkaline conditions, respectively, with implications on the mechanism, selectivity, and intrinsic activity of different catalytic sites. The ORR mechanism can also proceed indirectly, first involving 2 electrons leading to H_2O_2 or HO_2^- peroxide intermediate release ($O_2 + 2\ H^+ + 2e^- \rightarrow H_2O_2$ and $O_2 + H_2O + 2e^- \rightarrow HO_2^- + OH^-$) followed by a second sequential 2-electron transfer, whereby H_2O_2 or HO_2^- is reduced to H_2O

or OH^-, at the same or at a different active site ($H_2O_2 + 2\ H^+ + 2e^- \rightarrow 2\ H_2O$ and $HO_2^- + H_2O + 2\ e^- \rightarrow 3\ OH^-$). Chemical disproportionation of H_2O_2 and HO_2^- may also be considered in both media [1, 15]. In addition to the different roles of H^+ and OH^- species and different intermediate species in the two different electrolytes, the pH difference can also modify the double-layer structure, resulting in different possibilities of electron transfer mechanisms: inner- and outer-sphere [16, 17].

Many studies have investigated the nature of the different ORR active sites in M-N-C catalysts [18–20], and three main types of active sites have been proposed: N_xC_y, M-N_xC_y, and M@N-C [7], where N_xC_y sites are nitrogen functional groups in a carbon matrix, M-N_xC_y are atomically dispersed nitrogen bonded metal centers embedded in a N-doped carbon matrix, and M@N-C sites are nanoparticulated metallic centers surrounded by a N-doped carbon shell (itself free of M-N_xC_y sites). In tuning the intrinsic ORR activity of these structurally and chemically different active sites, another important parameter is the nature of the metal (M), with all works reported since the 1990s pointing to iron (Fe) and cobalt (Co) as universally leading to the most active PGM-free metals, regardless of the nature of the metal-based sites, M-N_xC_y or M@N-C [21–23].

Regarding Co-N-C catalysts, Co-N_xC_y moieties have been pointed as the main active centers that catalyze the ORR, either in alkaline or acidic conditions [24–26]. Meanwhile, Co@N-C sites have shown ORR activity, with the N-C matrix providing protection of the metallic core, that would otherwise be rapidly leached out in acidic medium [26]. Along the same lines, the high ORR activity of Fe-N-C catalysts has been clearly linked to the content of Fe-N_xC_y sites, especially in low pH conditions [7, 27]. However, it has been recently reported that Fe-N-C catalysts containing Fe@N-C core-shell structures (without Fe-N_xC_y moieties) also can exhibit good ORR activity, either in high or in low pH conditions [19, 28, 29]. In summary, it is well-established that optimized M-N-C catalysts can achieve high activities towards ORR electrocatalysis, sometimes approaching those of PGM-based materials. However, it is still unclear which are the truthful activities of M-N_xC_y and M@N-C sites, when the catalysts are used in different pH conditions.

Herein, we study the ORR electrocatalytic activity and mechanism of two M-N-C catalysts exclusively comprising metal as M-N_xC_y sites (Fe or Co), two other M-N-C catalysts exclusively comprising metal as M@N-C core-shell structures (Fe or Co), and one N-C baseline material synthesized similarly as the other four materials but without addition of Fe or Co precursor under both acidic and alkaline conditions. The catalysts were characterized by transmission electron microscopy (TEM) and X-ray absorption spectroscopy (XAS). Their electrochemical activity was evaluated in acidic (0.1 mol L^{-1} H_2SO_4) and alkaline (0.1 mol L^{-1} NaOH) conditions using rotating ring-disk electrode (R(R)DE). This study demonstrates that changing the pH from acidic to alkaline results in a switch of the ability of Ar pyrolized M-N_xC_y and M@N-C sites to reduce O_2; while M-N_xC_y sites (Fe-N_xC_y > Co-N_xC_y) are most active in acidic conditions, M@N-C (Fe@N-C > Co@N-C) reach a higher mass activity (powder mass) in alkaline conditions.

1.2 Experimental Section

1.2.1 Electrocatalyst Synthesis

The electrocatalysts were synthesized using the method described by Zitolo *et al.* [24], in which the zinc(II) zeolitic imidazolate framework ZIF-8 (purchased from BASF, Basolite Z1200), metal(II) acetate (Fe or Co), and 1,10-phenanthroline were mixed via dry planetary ball milling in optimized ratio of 200 mg phenanthroline, 800 mg ZIF-8, and either 0.5 wt.% or 5.0 wt.% of metal (Fe or Co) to the overall mass of the three precursors. The dry mixed powder of the catalyst precursor was then heated under Ar flow with a ramp rate of 5 °C min^{-1} to 1050 °C, and held at that temperature for 1 h, at which point the split-hinge oven was opened and the quartz tube and boat quenched to room temperature while still flowing Ar. The amount of Fe or Co before pyrolysis was either 0 (for N-C), 0.5, or 5.0 wt.% in relation to the total mass of metal salt, phenanthroline, and ZIF-8. Due to about 2/3 mass loss of phenanthroline and ZIF-8 during the pyrolysis, the Fe or Co content after pyrolysis is *circa* three times higher than in the catalyst precursor before pyrolysis. The catalysts are labeled as M_x, where M is Fe or Co and x is the wt.% metal in the catalyst precursor before pyrolysis, either 0.5 or 5.0. As a benchmark catalyst, Pt nanoparticles (40 wt.%) supported on graphitized carbon (TEC10EA40E) was utilized, purchased from Tanaka Kikinzoku Kogyo (TKK).

1.2.2 Preparation of Inks and Layers

Inks for the formation of PGM-free catalyst layers were prepared by dispersing the catalytic powders (10 mg) with a 5 wt.% Nafion solution (50 µL, Sigma-Aldrich), isopropanol (854 µL, Carl Roth), and ultrapure water (372 µL, Millipore, 18.2 MΩ cm), followed by ultrasonic homogenization, as described by Kumar *et al.* [30]. For the benchmark catalyst, the ink was prepared in a similar way, consisting of Pt/C powder (5 mg), 5 wt.% Nafion solution (54 μL), isopropanol (1446 μL), and ultrapure water (3600 μL). Then, the desired aliquot of each prepared ink was dropped onto glassy carbon disk substrate of the RDE or RRDE (0.196 cm^2 for both), followed by drying with hot air under controlled rotation speed. The total loadings were in the range of 0.1 to 0.8 mg_{powder} cm^{-2} for PGM-free catalysts and 20 $\mu g_{Pt/C}$ cm^{-2} (on RDE) or 10 $\mu g_{Pt/C}$ cm^{-2} (on RRDE) for the Pt/C benchmark catalyst.

1.2.3 Electrochemical measurements

Before any electrochemical experiment, the glassware, polytetrafluoroethylene (PTFE)–based materials, and electrodes were cleaned with a 50% v/v solution of H_2SO_4 (Merck, Suprapur 96 wt.%)/H_2O_2 (Carl Roth, 30% w/w) followed by rinsing in ultrapure water (MQ grade, 18.2 MΩ cm, 1–3 ppm TOC) and hot ultrapure water. All glassy carbon disks were polished with 3 and 1 μm diamond polishing paste (Presi). Fresh Ar-saturated electrolytes were prepared from NaOH (Alfa Aesar, 50% w/w aq. soln.), H_2SO_4, and ultrapure water to obtain an electrolyte concentration of 0.1 mol L^{-1}.

The electrochemical measurements were performed using three-electrode electrochemical cells with the temperature-controlled at 25 °C. A glass cell was used for acid medium and PTFE cell for alkaline medium. A commercial reversible hydrogen electrode (RHE, Gaskatel GmbH) connected to the cell by Luggin capillary was used as the reference electrode. To filter the high-frequency electrical noise, a Pt-wire immersed in the electrolyte was connected to the reference electrode. In each electrolyte, the counter electrode was a carbon sheet and the working electrode was glassy carbon coated with the investigated catalyst, with loading varying depending whether RDE or RRDE measurements were performed, as described below.

RRDE or RDE measurements were performed with Autolab PGSTAT302N and PGSTAT12 potentiostat, respectively. For RDE measurements, a homemade glassy carbon cylinder (glassy carbon Sigradur® from HochtemperaturWerkstoffe GmbH) embedded in a PTFE cylinder, coupled to a commercial system for controlling the rotation rate (Origalys), was utilized as the working electrode. For RRDE measurements, a Pt-ring and a glassy carbon disk tip (Pine Research) embedded in a PTFE rod was used.

For both RDE and RRDE measurements, electrochemical break-in of the thin-film electrodes was performed by applying 50 cyclic voltammograms (CVs) between 0.0 and 1.0 V *vs.* RHE at 100 mV s^{-1} in Ar-saturated 0.1 mol L^{-1} H_2SO_4 or 0.1 mol L^{-1} NaOH. Then, the CVs of the thin films were recorded in the same conditions at 10 and 5 mV s^{-1}. The ORR polarization curves were recorded at 5 mV s^{-1} in O_2-saturated electrolyte at 1600 rpm. All measurements were dynamically corrected from ohmic drop.

The kinetic current density for ORR (i_k) was determined according to Koutecky Levich (Equation 1.1):

$$i_k = -\frac{(i_L . i)}{(i_L - i)} \tag{1.1}$$

where i_L is the oxygen diffusion–limited current density at 0.2 V *vs.* RHE and i is the Faradaic current after ohmic drop correction and capacitive current subtraction.

Consequently, the mass activity (i_{MA}) was calculated using the equation below:

$$i_{MA} = \frac{i_k}{m} \tag{1.2}$$

where m is the catalyst mass on the glassy carbon electrode.

For RRDE measurements, the same initial steps as described for RDE measurements were followed. Additionally, the catalyst loading was 0.1 mg_{powder} cm^{-2} except for the Pt catalyst for which 10 $\mu g_{Pt/C}$ cm^{-2} was utilized. To detect H_2O_2 or HO_2^- produced during ORR, the Pt-ring was polarized at 1.2 V *vs.* RHE. The peroxide quantification further requires the value of the collection efficiency (N), which was determined experimentally using the Fe^{3+}/Fe^{2+} redox couple from $K_3Fe(CN)_6$ salt, as described before [31]. The experimental value was found to be N = 0.24. The equations below were utilized for determining the number of electrons transferred along the ORR (n_{e-}, Equation 1.3) and the peroxide percentage (Equation 1.4):

$$n_{e-} = \frac{4 i_d}{i_d + \left(\frac{i_r}{N}\right)} \tag{1.3}$$

$$\%H_2O_2 \text{ or } \%HO_2^- = \frac{2\frac{\mathrm{i_r}}{\mathrm{N}}}{(\frac{\mathrm{i_r}}{\mathrm{N}}) + \mathrm{i_d}} \text{ x } 100 \tag{1.4}$$

where i_d and i_r are the currents at the disk and Pt-ring, respectively.

1.2.4 Physicochemical characterizations

TEM images of the electrocatalysts were recorded using a JEOL 2010 TEM instrument operated at 200 kV with a point-to-point resolution of 0.19 nm. Acquisition of Co and Fe *K*-edge X-ray absorption spectra were made at room temperature, in transmission mode at SAMBA beamline of the Synchrotron SOLEIL (Gif-sur-Yvette, France), with a focusing Si(220) monochromator. Pellets were prepared by mixing an adequate catalyst amount with PTFE powder so as to get an optimal absorption signal. The Athena software was employed for XAS data analysis, comprising the XANES (X-ray absorption near edge structure) spectra and the Fourier transforms of the EXAFS (extended X-ray absorption fine structures) signals [32].

1.3 Results and discussion

Detailed physicochemical characterization of the catalysts using XAS, Raman and ^{57}Fe Mössbauer spectroscopy, TEM, X-EDS, and XRD analyses [30, 33] have been presented in previous studies published by Zitolo *et al.* [33] and Kumar *et al.* [30]. In brief, the important observations previously reported are that the catalysts with 5 wt.% metal contents ($M_{5.0}$) comprise metallic or metal carbide nanoparticles surrounded by a shell of N-doped graphitic carbon (here referred to as M@N-C), while catalysts with low metal content ($M_{0.5}$) comprise metal cations that are atomically dispersed in the N-doped carbon matrix and coordinated by nitrogen atoms (here referred to as M-N_xC_y). Moreover, metal-based particles in the $Fe_{5.0}$ and $Co_{5.0}$ catalysts were found to be exclusively Fe_3C and metallic Co, respectively. Other important findings are related to the presence of more graphitic carbon structure in the neighborhood of the metal-based nanoparticles for $M_{5.0}$ catalysts, as well as the presence of smaller graphite crystallites in $M_{0.5}$.

Figure 1.1 displays physicochemical characterizations of $Fe_{0.5}$, $Fe_{5.0}$, $Co_{0.5}$, and $Co_{5.0}$. TEM images shown in Figure 1.1 (a)–(d) evidence that the synthesized catalysts exhibit two different carbon nanostructures: stacked graphitic layers (mainly for $Fe_{5.0}$ and $Co_{5.0}$) and sheet-like layers with poorly structured carbon, for both metal contents. This indicates that the initial highly structured and organized ZIF-8 carbon and nitrogen precursor was significantly modified during pyrolysis. As reported previously [26, 29], these results confirm that the catalysts present particular characteristics denoting the existence of two distinct zones: (i) in one case, the presence of segregated metallic-based nanoparticles (10–40 nm) is seen, as confirmed by the dark spots in the images of the higher metal load materials ($Fe_{5.0}$ and $Co_{5.0}$), and (ii) a zone containing the metals atomically dispersed over the carbon-nitrogen matrix ($Fe_{0.5}$ and $Co_{0.5}$).

Figure 1.1 (e) and (f) show XANES spectra for both types of catalysts at the Fe (energy = 7112 eV) and Co (energy = 7709 eV) K-edges, respectively, where reference spectra for Fe and Co foils and Fe_3C were included for comparison. The high similarities between the XANES signals obtained for $Fe_{5.0}$ and $Co_{5.0}$ with those shown for Fe_3C and metallic Co foils, respectively, clearly indicate that the black spots in Figure 1.1 (b) and (d) for these samples are essentially zero-valent Fe and Co species [30]. In the cases of $Fe_{0.5}$ and $Co_{0.5}$, the shift towards higher energy of the edge with respect to that of the metal foil and the large hump peaking at ca. 20 eV above the energy of the metal edge is unequivocally evidencing that the Co and Fe atoms are present in oxidized states [24, 30, 33].

Fourier transforms of the EXAFS signals, either for the samples as well as for the metallic standards, are shown in Figure 1.1 (g) and (h). First, it should be noted that the x-axis positions of the several peaks are related to the distance between the X-ray absorbing metal atoms and neighboring atoms present in the different coordination shells surrounding the element under investigation. However, the radial distances do not exactly correspond to the atomic distances, since a phase shift correction must be applied to precisely estimate the interatomic distance and this correction depends on the nature of the backscattering elements [33]. Here, in the case of the Fe-containing materials (Figure 1.1 (g)), the presence of the Fe-Fe coordination (peak next to 2.1–2.2 Å) is only detected for $Fe_{5.0}$, as concluded from comparisons with the features of the Fe_3C [34] and results reported by Zitolo *et al.* [33]. In this case, a weak shoulder is also observed at radial distance near to 1.6–1.7 Å, and this may be related to the existence of some Fe-C or Fe-N interatomic distances in the second coordination sphere, possibly assigned to Fe-C interatomic distance in Fe_3C or to Fe-C interatomic distance from a small amount of $Fe\text{-}N_xC_y$ moieties. However, ^{57}Fe Mössbauer transmission spectra for the same material (catalyst named as $Fe_{5.0}RP$ in that work) performed in our former work [30] revealed the presence of only one sextet component with Mössbauer parameters exactly matching those of Fe_3C. The ^{57}Fe Mössbauer spectra confirmed the conclusions drawn from XANES and EXAFS signals, and thus, it may be concluded that $Fe_{5.0}$ does not contain Fe-N bonds from $Fe\text{-}N_xC_y$ moieties. This is also in line with the absence of EXAFS signal for $Fe_{5.0}$ at a radial distance of ca. 1.0 Å, typical for Fe-N distance in $Fe\text{-}N_xC_y$ moieties. For the $Fe_{0.5}$ material, the main peak located at 1.4 Å and the less-intense peak at 2.4 Å might be assigned to Fe-N and Fe-C backscatterings, respectively [33]. It should also be noted that the signals for more distant shells are only clearly observed for the Fe foil, indicating the absence of long distance ordered coordination shells in Fe-containing samples, particularly for $Fe_{0.5}$. This observation is in agreement with usual propositions that, for these kind of systems, metal species are atomically dispersed in the carbon-nitrogen matrix for $Fe_{0.5}$ and, mainly as Fe_3C for $Fe_{5.0}$. Finally, the EXAFS of the

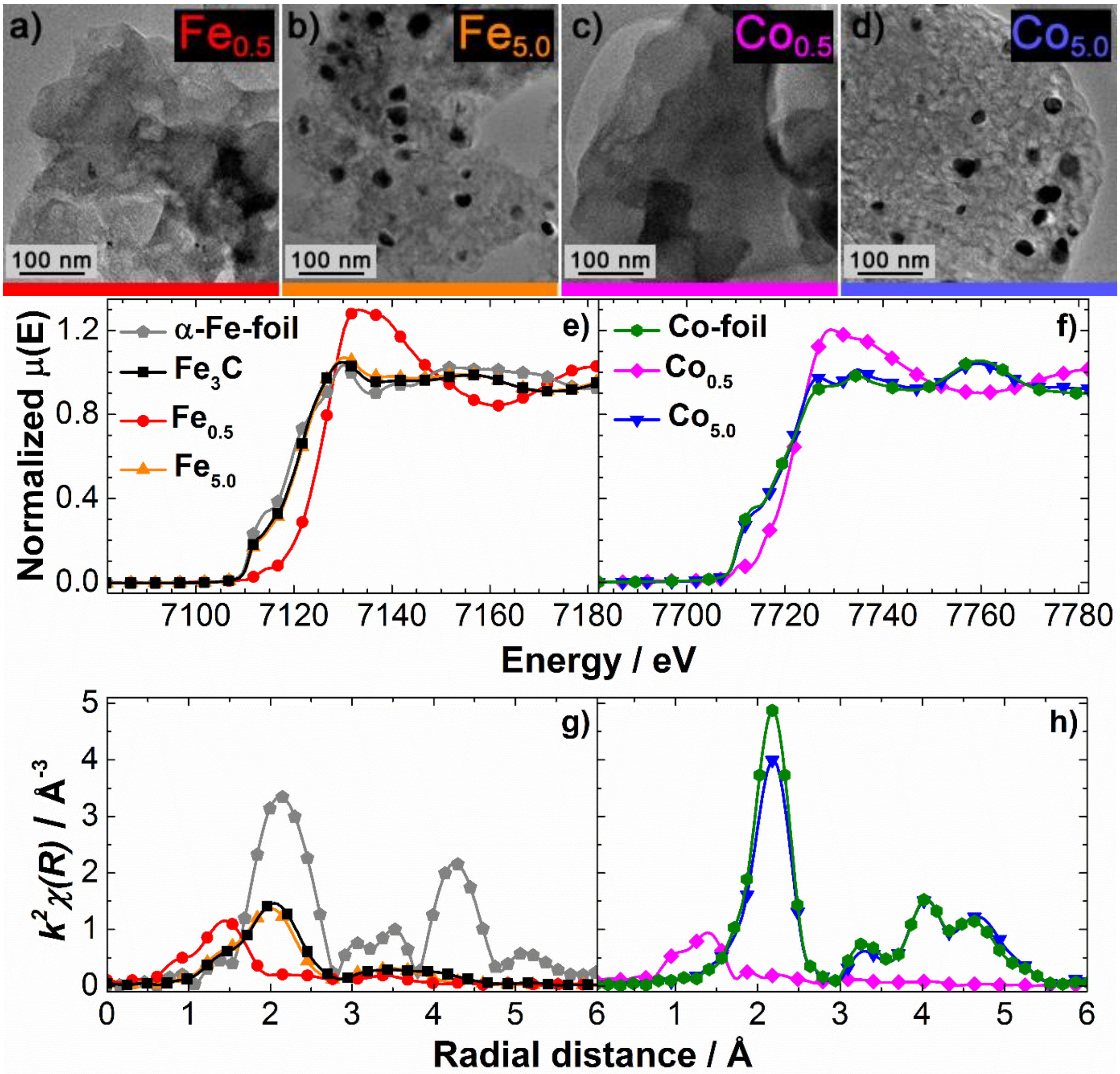

Figure 1.1 Physical and chemical properties of metal-N_xC_y and metal@N-C catalysts. **(a–d)** Representative transmission electron microscopy images, **(e, f)** XANES, and **(g, h)** Fourier transforms of the EXAFS spectra measured at Co or Fe *K*-edge. Adapted from ref. [30] with permission from The American Chemical Society.

Co-based catalysts evidence two main differences with respect to the Fe-based catalysts: (i) in the case of $Co_{5.0}$, the Co-Co coordination extends to much longer shells resembling that of the Co foil, confirming that metallic Co is present as a principal species; (ii) in the case of $Co_{0.5}$, the XANES is similar to that of $Fe_{0.5}$ and calculations of XANES spectra for different model sites showed that a good match could be obtained with either porphyrinic (CoN_4C_{12}) or defective porphyrinic structures (e.g., CoN_3C_{10}) [24].

Figure 1.2 (a) and (b) show ohmic-drop corrected CVs for all four catalysts at a fixed loading in the thin-film electrode in acid and alkaline electrolytes, respectively. Results for a Fe and Co-free N-doped carbon prepared otherwise similarly (labeled M_0) are included for comparison. For the $M_{5.0}$ and M_0 catalysts and either in acid or alkaline electrolytes, the CV features are those typically found for large capacitance systems, so that the currents are mostly related to charge accumulation in the double layer (non-faradic and non-redox process) at the catalyst|electrolyte interface. This general trend differs in the case of $Fe_{0.5}$ in acid medium, for which a redox pair, consistent with the Fe^{3+}/Fe^{2+} couple, is apparent at ca. 0.7 V *vs.* RHE. Results in Figure 1.2 (a) also show that the CV profiles exhibit similar current intensities, except for the $Fe_{0.5}$ catalyst, for which the intensities are unequivocally higher than the others, which we relate to a larger carbon-specific surface area [30], and/or features associated to the presence of surface defects, as compared with the other cases. Another aspect is that $Co_{0.5}$ has a larger surface area than $Fe_{0.5}$ [30], yet results in a CV that is distinct from that of $Fe_{0.5}$ and more similar to those of the other catalysts with lower BET area. This may be explained by the presence of too narrow micropores in this case, which do not effectively contribute to the charge accumulation in the double layer, and/or to the more organized structure of the carbon phase, leading to a lower content of surface groups (N or O) and thereby decreased capacitive currents [35]. The absence of redox peak assigned to Co cations in $Co_{0.5}$ is explained by the fact that the Co^{2+}/Co^{3+} redox in a similar Co-N-C catalyst (flash pyrolyzed) was found at potentials well above the upper limit of the CVs presented here [24]. However, we noticed anodic current at high potential values for $Co_{5.0}$ in alkaline electrolyte, which indicates that Co nanoparticles are progressively covered by a thin passivating layer of $Co(OH)_2$ followed by the oxidation of $Co(OH)_2$ to Co_2O_3 and CoOOH species, in agreement with the literature [36, 37].

Finally, the absence of Fe redox features for the $Fe_{5.0}$ catalyst in acidic conditions is consistent with previous results showing that in this case all Fe is present as encapsulated metal carbide nanoparticles [30]. This implies that these species, even when present in the catalyst, have no direct contact with the electrolyte.

Polarization curves for the ORR were constructed by subtracting the capacitive currents of CV (at 5 mV s^{-1}) in Ar-saturated electrolytes from those related to the ORR, and employed to evaluate the ORR activity of the catalysts (M_0, $M_{0.5}$, and $M_{5.0}$). These results are shown in Figure 1.2 (c) and (d), for the acid and alkaline electrolytes, respectively, while results obtained for a Pt/C catalyst were included for comparison. Generally, results show that all onset potentials are higher for Fe-N-C than for Co-N-C catalysts, denoting the higher activity of Fe-N-C materials for the ORR electrocatalysis. Following previous descriptors for the ORR activity on M-N-C catalysts, these differences in activity can be discussed in terms of the possibility that the reaction may occur involving inner- and outer-sphere electron transfer processes in alkaline media [16, 17], and also in terms of the binding energy of O_2 on M^{2+} active metal species in acid media [21], as detailed below.

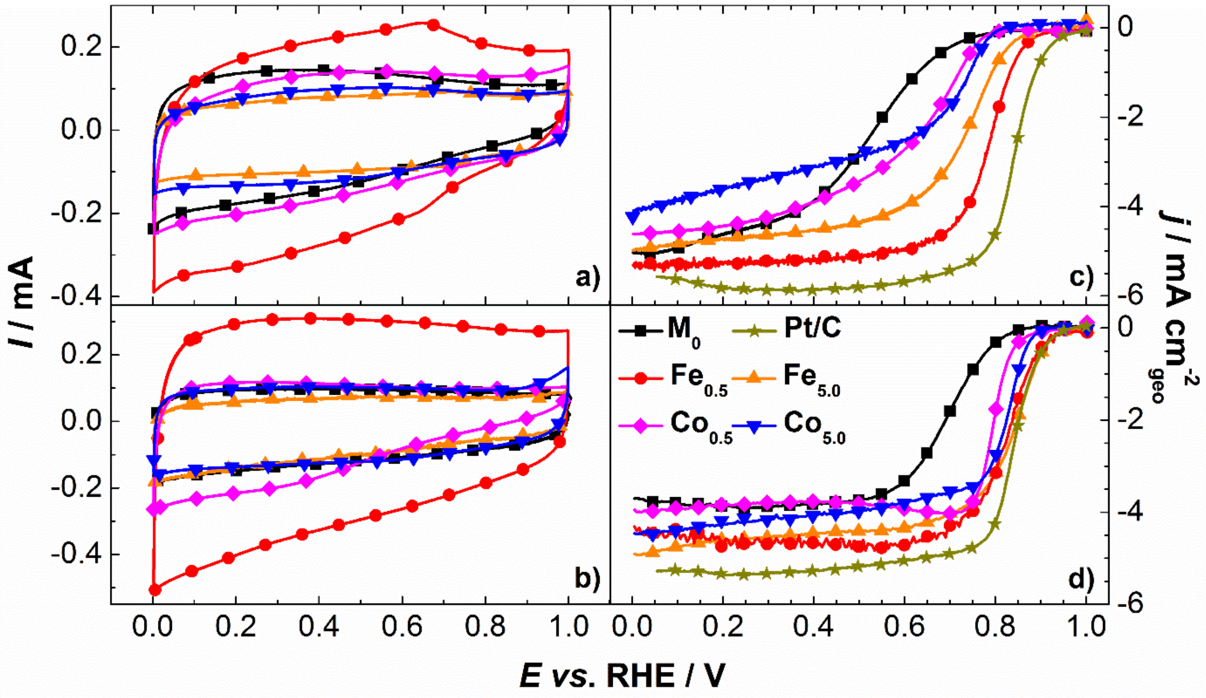

Figure 1.2 Electrochemical properties of Fe-N-C and Co-N-C catalysts in alkaline and acid media. CVs in Ar-saturated electrolyte 0.1 mol L^{-1} **(a)** H_2SO_4 and **(b)** NaOH at 10 mV s^{-1}; ORR polarization curves in O_2-saturated electrolyte 0.1 mol L^{-1} **(c)** H_2SO_4 and **(d)** NaOH at 5 mV s^{-1} and 1600 rpm. For all measurements: 0.8 mg$_{powder}$ cm^{-2} and 25 °C. For comparison, Pt/C (20 μg$_{Pt/C}$ cm^{-2}) and M_0 (N-C without Fe or Co) catalysts were utilized. Measurements were repeated at least three times leading to the same results (all results and errors are tabulated in the Appendix 1 – Table A1.1 and A1.2)

In alkaline conditions, both outer- and inner-sphere electron transfer processes can co-exist in the same electrocatalyst at different potentials [16, 17]. At potentials > 0.8 V *vs.* RHE, the outer-sphere electron transfer is essentially inoperant and the reaction can occur by the direct adsorption of desolvated O_2 on the active sites, thus following the inner-sphere electron transfer [17]. In this case, the onset potential for the ORR is dependent on the binding energy between

O_2 and the active metallic center (M^{2+}), which in turn is directly related to the M^{3+}/M^{2+} redox potential [17, 18, 21, 38]. Based on the fact that the redox potential of Co^{3+}/Co^{2+} ($E^o = 1.92$ V) is much higher than that of Fe^{3+}/Fe^{2+} ($E^o = 0.77$ V) [39], the O_2 molecule adsorbs much weakly and/or to a lesser extent on Co^{2+}, and in this way, the ORR onset potential for Co-N-C would be smaller than that for Fe-N-C catalysts, as observed in Figure 1.2 (d). In acidic conditions, inner-sphere electron transfer is the only possibility for the ORR electrocatalysis [16, 17]. Therefore, the causes of the differences in the ORR onset potentials on different metallic centers are explained similarly to the alkaline medium.

Figure 1.2 (c) shows that in acidic conditions, $Fe_{0.5}$ reaches the highest onset potential among all catalysts (0.92 ± 0.01 V), being only 0.04 V smaller than that of Pt/C (see details in the Appendix 1 – Table A1.2). The behavior of this catalyst confirms the high importance of having atomically dispersed Fe-N_xC_y active sites for allowing the occurrence of the Fe^{3+}/Fe^{2+} oxi-reduction process, as detected by CV. This couple seems to be the cause of the enhanced ORR electrocatalysis [40, 41] compared with the other catalysts. As already discussed in the literature [5, 17, 21], the active sites first generate Fe^{2+} from the reduction of Fe^{3+} (Equation 1.5), which next promotes the displacement of adsorbed H_2O by O_2, accompanied by an electron transfer of Fe^{2+} to O_2 (Equation 1.6); the $[Fe^{3+}\text{-}OH^-]_{ads}$ species would be regenerated in the following reaction step, so that the process becomes cyclically repeated:

$$[Fe^{3+}\text{-}OH^-]_{ads} + H^+ + e^- \rightleftharpoons [Fe^{2+}\text{-}OH_2]_{ads} \tag{1.5}$$

$$[Fe^{2+}\text{-}OH_2]_{ads} + O_2 \longrightarrow [Fe^{3+}\text{-}O_2^-]_{ads} + H_2O \tag{1.6}$$

In acid media, other studies have shown that the onset potential for the ORR is directly related to the redox potential of the metal in the M-N_xC_y sites [17, 21, 28]. Here, such a redox process was only evident for $Fe_{0.5}$; it was not seen for $Fe_{5.0}$ because in this case the only catalyst metal phase is formed by Fe_3C particles surrounded by a nitrogen-carbon shell (Fe@N-C). Finally, in the case of the Co-N-C catalysts in acid media, although results in Figure 1.2 show that $Co_{0.5}$ presents the same atomic distribution as $Fe_{0.5}$, the corresponding CV does not evidence the occurrence of redox processes. This is because the presence of redox features of Co only appears at potentials well above the onset of the ORR, as is the case of Co^{3+}/Co^{2+}. From the results in Figure 1.2 (c), it is seen that the activity of the Co-N-C catalysts for the

ORR is in fact not so much superior to that of M_0, which demonstrates the smaller role of Co-N_xC_y and Co@N-C for the promotion of the ORR electrocatalysis.

In alkaline medium, for the Fe-N-C catalysts (Figure 1.2 (d)), results show that the ORR onset potentials are very close (or equal, in the case of $Fe_{5.0}$) to those of Pt/C (0.97 ± 0.01 V), that is, 0.97 ± 0.01 V for $Fe_{5.0}$ and 0.95 ± 0.01 V for $Fe_{0.5}$. This high catalytic activity of $Fe_{5.0}$ evidences that in this medium, the Fe@N-C sites are active for the ORR, in contrast to the acid medium. Although substantially smaller than those of the Fe-N-C materials, the same catalytic phenomena are seen for the Co@N-C and Co-N_xC_y materials, for which the values of onset potential are 0.84 ± 0.01 V and 0.82 ± 0.01 V, respectively. In fact, a similar enhancement of catalytic activity is also seen in the absence of metallic centers (M_0). The higher activity of the Fe@N-C active sites in alkaline medium can be assigned to the enhancement of electrical conductivity of nitrogen-carbon and a synergistic effect between the metallic centers and the nitrogen-carbon shell. This is in line with recent results demonstrating that a higher degree of graphitization of carbon is beneficial to the electrical conductivity [42] and that synergies between the nitrogen-carbon shell and metallic centers contribute to efficient ORR electrocatalysis [19, 28, 43–46]

Another aspect to be discussed is the cause of the positive shift on the onset potential when the pH is changed from low to high values. This fact may be related to the OH_{ads} coverage and its desorption to regenerate the active metallic center M^{2+} [5, 18, 21]. Thus, a higher concentration of OH^- species in the electrolyte (alkaline media) seems to favor high coverages of OH_{ads}. In contrast, the effective OH_{ads} coverage in acidic conditions requires more energy due to the much smaller OH^- availability to generate and regenerate the M^{2+} active center, as shown above (Eqs. 1.5–1.6); also Fe^{3+} species can be poisoned by strong adsorption of H_2O, blocking the generation of Fe^{2+} species active for ORR [47].

Interestingly, the change in pH from acid to alkaline leads to a lower increase of the onset (half-wave) potentials by 30 mV (30 mV) for $Fe_{0.5}$ and 100 mV (70 mV) for $Fe_{5.0}$. This indicates that the activity of the Fe-N_xC_y sites in the present case is little affected by the pH, so that the $Fe_{0.5}$ catalyst can promote the ORR electrocatalysis with similar efficiency, either at high or at low H^+/OH^- concentrations. In contrast, results for Fe@N-C sites denote larger variations of onset/half-wave potentials, but the shift is smaller in the case of the half-wave potential, possibly indicating some occurrence of inner- and outer-sphere electron transfer mechanisms in alkaline medium, depending on the electrode potential. These behaviors were not found in Co-N-C catalysts, and, then this feature is exclusively related to Fe-N-C catalysts.

For the investigation of PGM-free catalyst loading effects on the mass activity for ORR electrocatalysis, the $Fe_{0.5}$ catalyst was selected in both pH conditions. Then, that catalyst loading effect was evaluated for $Fe_{0.5}$ in the range of 0.1 to 0.8 mg_{powder} cm^{-2} in 0.1 mol L^{-1} H_2SO_4 and 0.1 mol L^{-1} NaOH electrolytes, and the results are shown in Figure 1.3. CV profiles in Figure 1.3 (a) and (b) exhibit the expected proportional increase of the capacitive currents from low to high catalyst loadings in both pH conditions. For example, at 0.4 V, the capacitive currents increase linearly with the catalyst loading (see Figure A1.1 – Appendix 1). This is mainly caused by the increase in the electrochemically available area, which is more pronounced in acidic conditions due to some contributions of currents related to redox processes of Fe^{3+}/Fe^{2+} and of oxygen functional groups present in the carbon matrix. As described in the literature [48], the oxidative process of carbon causes changes in the magnitude of the capacitive current at low pHs, while in alkaline media, the graphitic structures are less functionalized because they become hydrophilic enough for releasing some carbon functional groups.

In Figure 1.3 (c) and (d), the results evidence a displacement of the ORR onset and half-wave potentials to higher values and increased oxygen diffusion–limited current densities (in the range of 0.0 V to 0.55 V) with the increase of the catalyst loading, with the effects being higher in the acid medium. This increase in the oxygen diffusion–limited current densities with the increase of the catalyst loading is probably related to the increased residence time of reactant/intermediate species [49, 50], like OH^-, O_2, H_2O_2, or HO_2^- inside the catalyst layer, enhancing their further reduction to complete the 4-electron process. Moreover, a sufficient number of active sites are necessary to catalyze the ORR efficiently [49, 50]; otherwise, no oxygen diffusion–limited currents appear, which in acid media seems to be the case for loadings $\leq$ 0.2 mg_{powder} cm^{-2}. In alkaline electrolytes, this effect may be minimized by the electrostatic interaction of anionic HO_2^- species with the Fe^{2+} cation from $Fe\text{-}N_xC_y$ active sites [16, 17, 40], thus driving the ORR to OH^- even in thin catalyst layers (as also observed in Figure 1.4) [51].

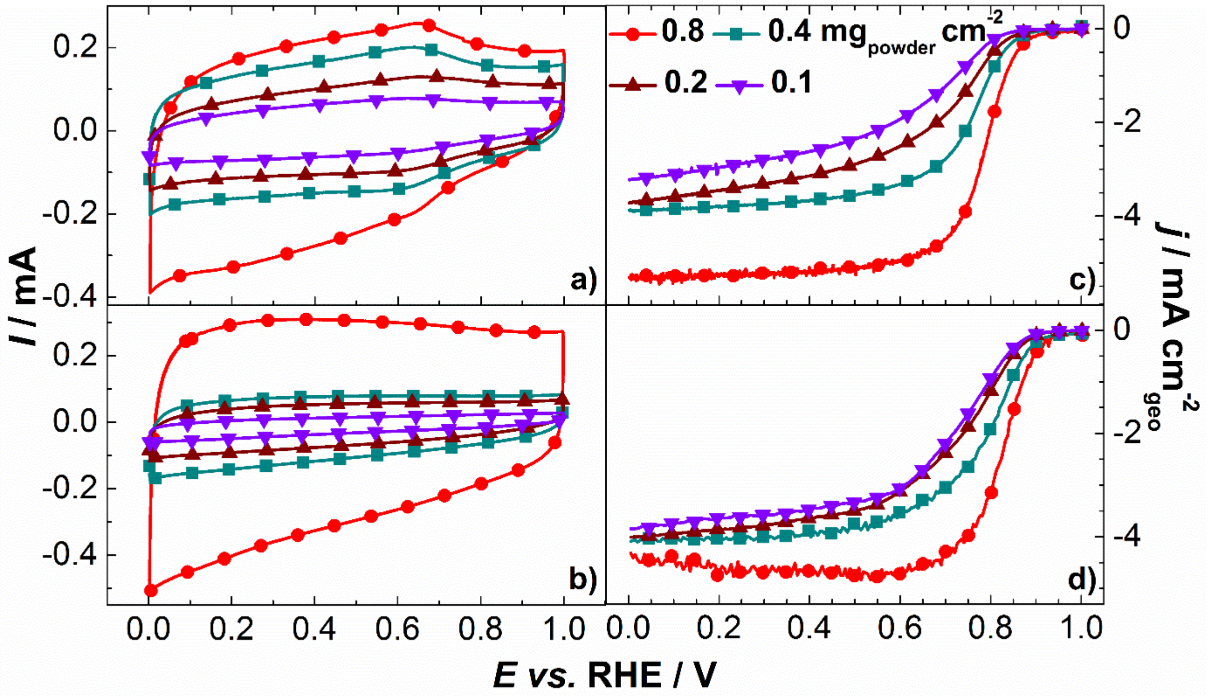

Figure 1.3 Electrochemical properties of different $Fe_{0.5}$ catalyst loadings. CVs in Ar-saturated electrolyte 0.1 mol L^{-1} **(a)** H_2SO_4 and **(b)** NaOH at 10 mV s^{-1}; ORR polarization curves in O_2-saturated electrolyte 0.1 mol L^{-1} **(c)** H_2SO_4 and **(d)** NaOH at 5 mV s^{-1} and 1600 rpm. All measurements were performed at 25 °C. Measurements were repeated at least three times leading to the same results (all results and errors are tabulated in the Appendix 1 – Table A1.3 and A1.4).

The oxygen diffusion–limited currents for the M-N-C catalysts are all smaller than those observed for Pt/C (Figure 1.2 (c–d)), that is known to lead to a predominant 4-electron ORR mechanism (O_2 is mostly reduced to H_2O in acid or OH^- in alkaline electrolytes). To discuss these issues, the percentages of H_2O_2/HO_2^- formation and the number of electrons involved in the ORR were obtained from rotating ring-disk measurements and these results are shown in Figure 1.4. Generally speaking, the n_{e-} values for the M-N-C catalysts, and more specifically Fe-N-C, are not so different from those of Pt/C, either in acid or alkaline media, but this is more evident in the alkaline medium (see Tables A1.1 and A1.2 of Appendix 1). Results related to the H_2O_2/HO_2^- formation are consistent with the above observations related to the number of transferred electrons in the ORR, as would be expected because the same data and principles are used in the calculations of n_{e-} and $\%H_2O_2/HO_2^-$. These aspects regarding the number of electrons/percentages of H_2O_2/HO_2^- formation confirm that in the alkaline medium Fe-N_xC_y and Fe@N-C sites perform the reaction involving similar pathways and provide additional evidence that the Fe@N-C sites stabilize the HO_2^- intermediate as efficiently as Fe-N_xC_y. Therefore, synergistic effects in the Fe@N-C catalyst can provide an adequate energy binding between HO_2^- and the nitrogen-carbon shell, even without the direct contact between the Fe metallic center and the reactants or intermediates. In the cases of the Co-N-C materials, inferior ne- values regularly ranging from 3 to 2 are observed in Figure 1.4 and Tables A1.1 and A1.2 (Appendix 1). Adequate adsorption energies of oxygenated intermediates species have been pointed to be essential for achieving high n_{e-} values in the ORR, and in this sense the anionic HO_2^- species formed along the ORR in alkaline conditions seems to be more strongly bound to the catalyst compared with the H_2O_2 species in acidic media, ensuring larger occurrence of the complete ORR electrocatalysis to OH^-. However, the higher amounts of H_2O_2/HO_2^- detected by the ring for the Co-catalysts, compared with the Fe-catalysts, may mean that the binding energies of H_2O_2/HO_2^- on Co-N_xC_y sites are small [21, 24, 52], as it would be also expected for the Co@N-C sites. In fact, trends observed here regarding the onset potentials, oxygen diffusion–limited currents, and number of electrons transferred in the ORR were similar to those observed in other studies of the ORR electrocatalysis in other Fe-N-C and Co-N-C catalysts [24, 53–55].

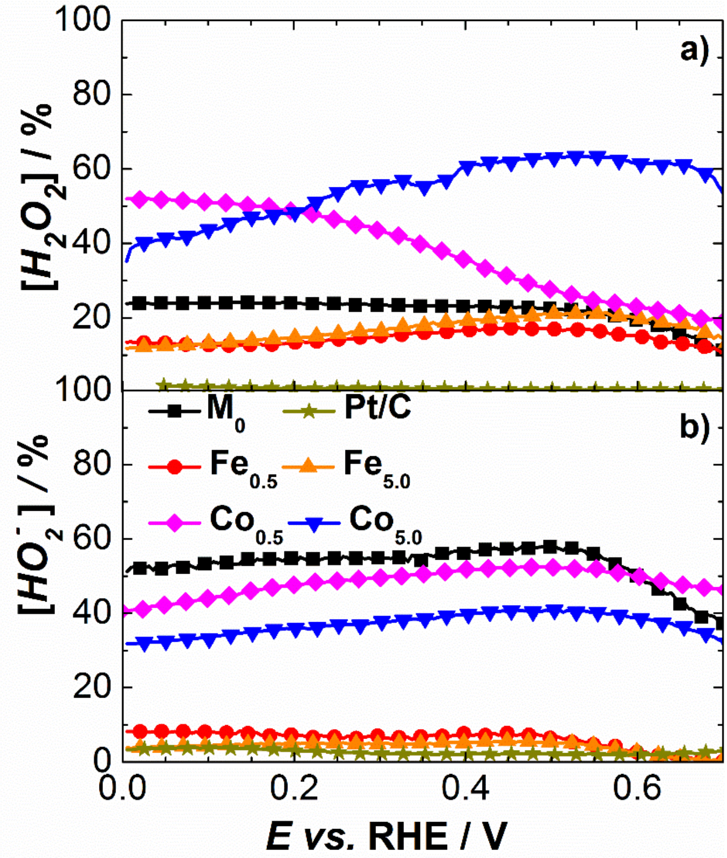

Figure 1.4 RRDE measurements of Fe-N-C and Co-N-C catalysts. Peroxide percentage produced from ORR electrocatalysis in O_2-saturated electrolyte 0.1 mol L^{-1} **(a)** H_2SO_4 and **(b)** NaOH at 5 mV s^{-1} and 1600 rpm. For all measurements: 0.1 mg_{powder} cm^{-2} and 25 °C. For comparison, Pt/C (10 $\mu g_{Pt/C}$ cm^{-2}) and M_0 (without Fe or Co) catalysts were utilized (all results are tabulated in the Appendix 1 – Table A1.1 and A1.2)

Further information about the reaction mechanism was obtained from Tafel plots constructed in the high-potential region of the ORR polarization curves and expressed in terms of the mass activity of the catalysts (i_{MA}), calculated as described in the “Experimental section.” Results are shown in Figure 1.5. The slopes of the resulting lines (Tafel slopes) were calculated, and the values are summarized in Tables A1.1-A1.4 of Appendix 1. First, it is noted that $Fe_{0.5}$ and $Fe_{5.0}$ exhibit higher Tafel slopes as compared with $Co_{0.5}$ and $Co_{5.0}$ in both media (Figure 1.5 (a–b)), and this is consistent with the occurrence of distinct ORR mechanisms and/or rate-determining steps in the two classes of investigated materials. This observation is similar to those reported in published works when comparing Fe- *vs.* Co-based catalysts [22, 24, 53, 56].

The Tafel slopes for $Fe_{0.5}$ and $Fe_{5.0}$ catalysts are essentially the same in acid or alkaline media, demonstrating that the rate determining step of the ORR mechanism may be the same in both cases, although involving different active sites and for $Fe_{0.5}$ in acid medium corresponding to a direct redox mediated process. This implies that the different ORR activities seen for $Fe_{0.5}$ and $Fe_{5.0}$ in acid media (as evidenced for the different reaction overpotentials at a given mass activity) may be related to the different catalyst-specific active areas and/or different synergistic phenomena related to the different natures of the active centers. In alkaline media, since no redox features are detected but the activities are also close, one may conclude that the rate-determining step, the ORR mechanism, and eventually the specific active area are very similar for both catalysts. Finally, the results evidence the absence of mass transport and conductivity problems related to the thickness/structure of catalytic layers, so that the magnitude of Tafel slopes is only related to the ORR mechanism [57].

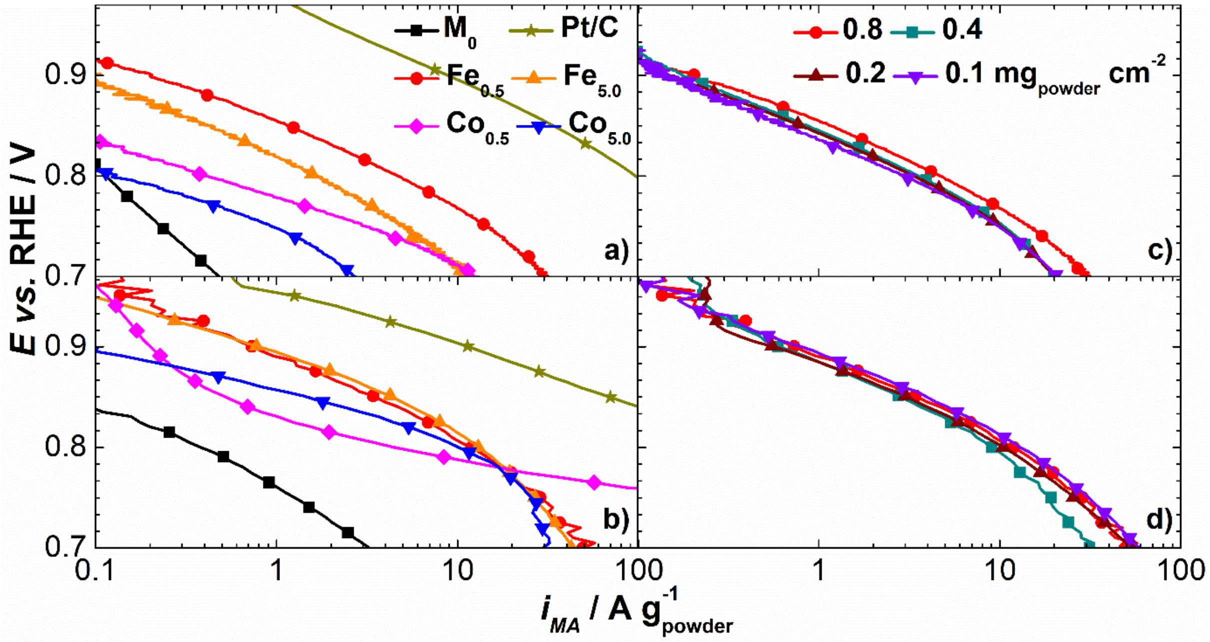

Figure 1.5 Mass-transport-corrected Tafel plots of Fe-N-C and Co-N-C catalysts at fixed loading, and for $Fe_{0.5}$ on different catalyst loadings. Performed in O_2-saturated electrolyte 0.1 mol L^{-1} **(a, c)** H_2SO_4 and **(b, d)** NaOH at 5 mV s^{-1}, 1600 rpm, and 25 °C. For **(a, b)** measurements: 0.8 mg_{powder} cm^{-2}; Pt/C (10 $\mu g_{Pt/C}$ cm^{-2}) and M_0 (without Fe or Co) catalysts were utilized. Measurements were repeated at least three times leading to the same results (all results and errors are tabulated in the Appendix 1 – Table A1.1 - A1.4). In **(c, d)** panels, different $Fe_{0.5}$ loadings were used.

For easier comparisons of the mass activity towards the ORR of materials, the previously calculated values at 0.85 V were plotted for each set of catalyst in both electrolytes (Figure 1.6 (a-b)). Analyzing the results in acidic conditions (Figure 1.6 (a)), it is concluded that among all M-N-C catalysts, $Fe_{0.5}$ presents the highest mass activity for the ORR, followed by $Fe_{5.0}$, $Co_{0.5}$ and $Co_{5.0}$, as shown in Figures 1.5 (a) and 1.6 (a). This superior activity of $Fe_{0.5}$ compared with that of $Fe_{5.0}$ indicates a superior activity of Fe-N_xC_y sites compared with Fe@N-C; this trend is maintained for $Co_{0.5}$ with respect to $Co_{5.0}$. Therefore, we conclude that M-N_xC_y sites provide higher mass activity than M@N-C in acid conditions.

In alkaline solution, results show that $Fe_{5.0}$ presents the highest mass activity for the ORR, followed by $Fe_{0.5}$, $Co_{5.0}$, and $Co_{0.5}$ (Figure 1.6 (b)). Therefore, generally speaking, it is seen that a high number of M@N-C sites (present in the catalysts with high metal content) can provide higher mass activity in alkaline medium as compared with a low number of M-N_xC_y sites, that is, predominant in catalysts with low metal content. These results show that, in alkaline media, the presence of atomically dispersed M-N_xC_y sites is not mandatory for the promotion of the ORR electrocatalysis with good efficiency. However, this mass activity distinction for materials containing M@N-C and M-N_xC_y sites seems to be evident only for Ar-pyrolyzed catalysts (or another inert gas). Indeed, recently, Santori *et al.* [58] have shown that other factors can lead to increased mass activity when switching from Ar- to NH_3-treated catalysts containing atomically dispersed Fe-N_xC_y sites. Further, another important aspect is that the catalyst without a metallic center (M_0) resulted in the poorest mass activity towards the ORR, stressing the crucial importance of having the metallic M@N-C or M-N_xC_y active sites for catalyzing the ORR, particularly in the case of iron. This is in agreement with the observation above reported, confirming that synergistic effects between the M^{2+} active metallic center and nitrogen-carbon shell (M@N-C) enhance the ORR mass activity, more than M-N_xC_y sites in high OH^- concentrations. Previous experimental studies provide support for the high activities found for Fe@N-C sites in alkaline media [10, 28, 44, 46, 59–61].

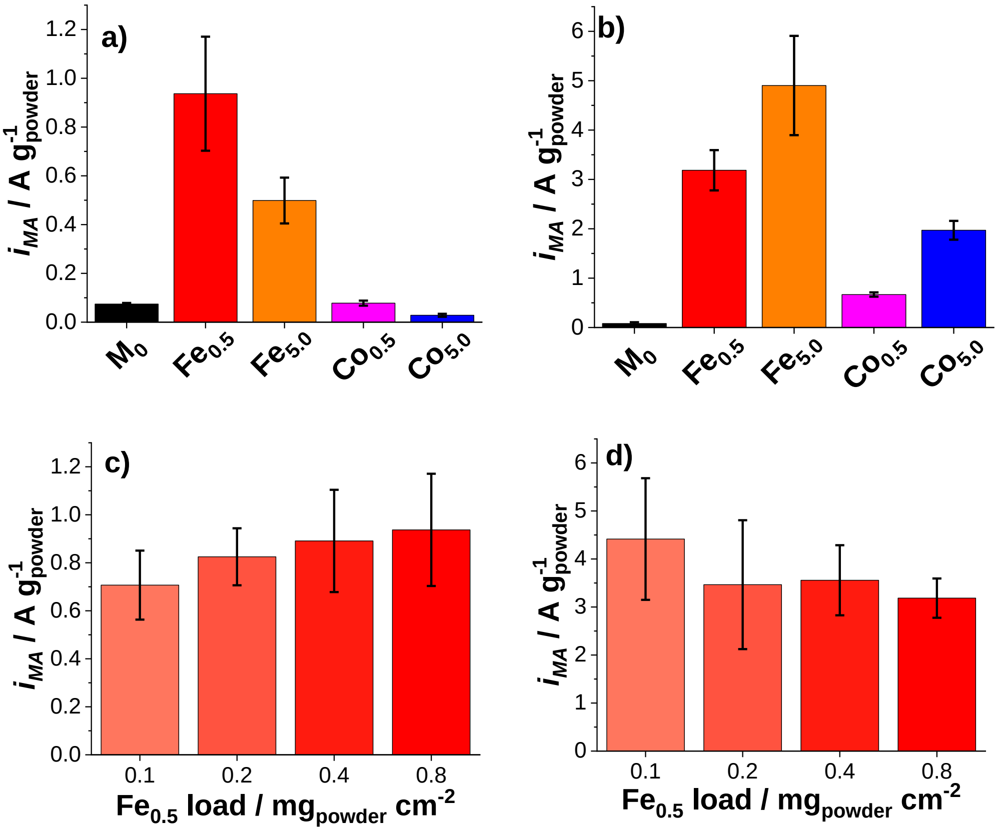

Figure 1.6 Mass activity towards the ORR (i_{MA}) measured at 0.85 V for **(a-b)** all catalysts investigated in this study and **(c-d)** different $Fe_{0.5}$ catalyst loadings. All ORR experiments conducted at 1600 rpm, 5 mV s^{-1}, and 25 °C in O_2-saturated 0.1 mol L^{-1} **(a,c)** H_2SO_4 or **(b,d)** NaOH electrolytes. Catalyst loadings of 0.8 mg_{powder} cm^{-2} were employed in **(a-b)**. Measurements were repeated at least three times leading to the same results (all results and errors are tabulated in Appendix 1 – Table A1.1 – A1.4).

Figure 1.5 (c-d) and Figure 1.6 (c-d) allows discussing the mass activity as a function of the $Fe_{0.5}$ catalyst loading for the two pH conditions. It is first noted that the mass activities are higher in alkaline than those in acid media, following the same trends found in Figure 1.6 (a-b). Also, it is noted that there is an increase of the ORR mass activity with increased catalyst loading in acidic conditions, while the opposite occurs in alkaline media. These results confirm the need of longer residence time of reactants and/or intermediates inside the catalyst layer, as well as of the amount of $Fe-N_xC_y$ sites in acid medium, while this is not the case in alkaline medium. These results have strong implications for the design of PGM-free catalysts layers in the cathodes of PEMFC and AEMFC.

1.4 Conclusions

In conclusion, we investigated the pH effect towards ORR electrocatalytic activities using a library of M-N-C catalysts featuring either $M-N_xC_y$ or M@N-C active sites. The change in the pH of the electrolyte resulted in a switch of the ability of the active sites to reduce O_2; however, the higher performance for Fe-N-C compared with Co-N-C catalysts was maintained. Therefore, we reported there are two factors that alter the ORR activity: (i) the nature of the metallic center and (ii) the nature of the active sites. It is found that $M-N_xC_y$ sites are more active when the ORR is performed in acidic conditions. For the most active center ($Fe-N_xC_y$), this property was assigned to the formation of Fe^{2+} from Fe^{3+}/Fe^{2+} redox couple in direct contact with the electrolyte, reactants, OH_{ads}, and intermediates due to their adequate energy binding with the surface. Conversely, M@N-C presents better performance for ORR electrocatalysis in the alkaline conditions when normalized by powder mass. Fe@N-C led to the highest activity for Ar-pyrolyzed catalysts, displaying an effective synergistic effect between the iron as a metallic core with the nitrogen-carbon shells. It is emphasized that the indirect contact of the metallic center with surface hydroxyl and other intermediates drives the ORR electrocatalysis more effectively. Finally, Fe@N-C stabilizes HO_2^- intermediates adequately resulting in predominance of 4-electron transfer per oxygen molecule.

1.5 References

1 Shao, M.; Chang, Q.; Dodelet, J.-P.; Chenitz, R. Recent Advances in Electrocatalysts for Oxygen Reduction Reaction. **Chemical Reviews**, v. 116, n. 6, p. 3594–3657, 2016.

2 Lopes, T.; Kucernak, A.; Malko, D.; Ticianelli, E.A. Mechanistic Insights into the Oxygen Reduction Reaction on Metal–N–C Electrocatalysts under Fuel Cell Conditions. **ChemElectroChem**, v. 3, n. 10, p. 1580–1590, 2016.

3 Gasteiger, H.A.; Kocha, S.S.; Sompalli, B.; Wagner, F.T. Activity benchmarks and requirements for Pt, Pt-alloy, and non-Pt oxygen reduction catalysts for PEMFCs. **Applied Catalysis B: Environmental**, v. 56, n. 1- 2 SPEC. ISS., p. 9–35, 2005.

4 Serov, A.; Zenyuk, I. V.; Arges, C.G.; Chatenet, M. Hot topics in alkaline exchange membrane fuel cells. **Journal of Power Sources**, v. 375, p. 149–157, 2018.

5 Li, J.; Alsudairi, A.; Ma, Z.F.; Mukerjee, S.; Jia, Q. Asymmetric volcano trend in oxygen reduction activity of Pt and non-Pt catalysts: In situ identification of the site-blocking effect. **Journal of the American Chemical Society**, v. 139, n. 4, p. 1384–1387, 2017.

6 James, B.D.; Spisak, A.B. Mass Production Cost Estimation of Direct H_2 PEM Fuel Cell Systems for Transportation Applications: 2012 Update Prepared By : **Strategic Analysis Inc.**, p. 1–62, 2012.

7 Li, J.; Ghoshal, S.; Liang, W.; Sougrati, M.T.; Jaouen, F.; Halevi, B.; McKinney, S.; McCool, G.; Ma, C.; Yuan, X.; Ma, Z.F.; Mukerjee, S.; Jia, Q. Structural and mechanistic basis for the high activity of Fe-N-C catalysts toward oxygen reduction. **Energy and Environmental Science**, v. 9, n. 7, p. 2418–2432, 2016.

8 Rêgo, U.A. do; Lopes, T.; Bott-Neto, J.L.; Gómez-Marin, A.M.; Tanaka, A.A.; Ticianelli, E.A. Non-Noble Fe-N x /C Electrocatalysts on Tungsten Carbides/N-Doped Carbons for the Oxygen Reduction Reaction. **Electrocatalysis**, v. 10, n. 2, p. 134–148, 2019.

9 Rêgo, U.A. do; Lopes, T.; Bott-Neto, J.L.; Tanaka, A.A.; Ticianelli, E.A. Oxygen reduction electrocatalysis on transition metal-nitrogen modified tungsten carbide nanomaterials. **Journal of Electroanalytical Chemistry**, v. 810, n. 2017, p. 222–231, 2018.

10 Zhong, G.; Wang, H.; Yu, H.; Peng, F. Nitrogen-doped carbon nanotubes with encapsulated ferric carbide as excellent electrocatalyst for oxygen reduction reaction in acid and alkaline media. **Journal of Power Sources**, v. 286, p. 495–503, 2015.

11 Brocato, S.; Serov, A.; Atanassov, P. PH dependence of catalytic activity for ORR of the non-PGM catalyst derived from heat-treated Fe-phenanthroline. **Electrochimica Acta**, v. 87, p. 361–365, 2013.

12 Meng, H.; Jaouen, F.; Proietti, E.; Lefèvre, M.; Dodelet, J.P. pH-effect on oxygen reduction activity of Fe-based electro-catalysts. **Electrochemistry Communications**, v. 11, n. 10, p. 1986–1989, 2009.

13 Elumeeva, K.; Ren, J.; Antonietti, M.; Fellinger, T.P. High Surface Iron/Cobalt-Containing Nitrogen-Doped Carbon Aerogels as Non-Precious Advanced Electrocatalysts for Oxygen Reduction. **ChemElectroChem**, v. 2, n. 4, p. 584–591, 2015.

14 Rojas-Carbonell, S.; Artyushkova, K.; Serov, A.; Santoro, C.; Matanovic, I.; Atanassov, P. Effect of pH on the Activity of Platinum Group Metal-Free Catalysts in Oxygen Reduction Reaction. **ACS Catalysis**, v. 8, n. 4, p. 3041–3053, 2018.

15 Ge, X.; Sumboja, A.; Wuu, D.; An, T.; Li, B.; Goh, F.W.T.; Hor, T.S.A.; Zong, Y.; Liu, Z. Oxygen Reduction in Alkaline Media: From Mechanisms to Recent Advances of Catalysts. **ACS Catalysis**, v. 5, n. 8, p. 4643–4667, 2015.

16 Ramaswamy, N.; Mukerjee, S. Influence of inner- and outer-sphere electron transfer mechanisms during electrocatalysis of oxygen reduction in alkaline media. **Journal of Physical Chemistry C**, v. 115, n. 36, p. 18015–18026, 2011.

17 Ramaswamy, N.; Tylus, U.; Jia, Q.; Mukerjee, S. Activity descriptor identification for oxygen reduction on nonprecious electrocatalysts: Linking surface science to coordination chemistry. **Journal of the American Chemical Society**, v. 135, n. 41, p. 15443–15449, 2013.

18 Jia, Q.; Ramaswamy, N.; Hafiz, H.; Tylus, U.; Strickland, K.; Wu, G.; Barbiellini, B.; Bansil, A.; Holby, E.F.; Zelenay, P.; Mukerjee, S. Experimental Observation of Redox-Induced Fe-N Switching Behavior as a Determinant Role for Oxygen Reduction Activity. **ACS Nano**, v. 9, n. 12, p. 12496–12505, 2015.

19 Zhong, L.; Frandsen, C.; Mørup, S.; Hu, Y.; Pan, C.; Cleemann, L.N.; Jensen, J.O.; Li, Q. ^{57}Fe-MÖssbauer spectroscopy and electrochemical activities of graphitic layer encapsulated iron electrocatalysts for the oxygen reduction reaction. **Applied Catalysis B: Environmental**, v. 221, n. June 2017, p. 406–412, 2018.

20 Singh, S.K.; Takeyasu, K.; Nakamura, J. Active Sites and Mechanism of Oxygen Reduction Reaction Electrocatalysis on Nitrogen-Doped Carbon Materials. **Advanced Materials**, v. 1804297, p. 1–17, 2018.

21 Zagal, J.H.; Koper, M.T.M. Reactivity Descriptors for the Activity of Molecular MN_4 Catalysts for the Oxygen Reduction Reaction. **Angewandte Chemie - International Edition**, v. 55, n. 47, p. 14510–14521, 2016.

22 Wu, G.; More, K.L.; Johnston, C.M.; Zelenay, P. High-performance electrocatalysts for oxygen reduction derived from polyaniline, iron, and cobalt. **Science**, v. 332, n. 6028, p. 443–447, 2011.

23 Chen, Z.; Dodelet, J. P.; Zhang, J. **Non-Noble Metal Fuel Cell Catalysts**. Wiley-VCH Verlag GmbH & Co. KGaA, 2014.

24 Ranjbar-Sahraie, N.; Zitolo, A.; Fonda, E.; Mineva, T.; Mukerjee, S.; Stamatin, S.; Lyth, S.M.; Li, J.; Jaouen, F.; Krtil, P.; Jia, Q.; Harrington, G.F. Identification of catalytic sites in cobalt-nitrogen-carbon materials for the oxygen reduction reaction. **Nature Communications**, v. 8, n. 1, p. 1–10, 2017.

25 Subramanian, P.; Mohan, R.; Schechter, A. Unraveling the Oxygen-Reduction Sites in Graphitic-Carbon Co–N–C-Type Electrocatalysts Prepared by Single-Precursor Pyrolysis. **ChemCatChem**, v. 9, n. 11, p. 1969–1978, 2017.

26 Perkas, N.; Schechter, A.; Gedanken, A.; Maiyalagan, T.; Sivakumar, P.; Subramanian, P. Electrochemical Oxygen Reduction Activity of Metal Embedded Nitrogen Doped Carbon Nanostructures Derived from Pyrolysis of Nitrogen-Rich Guanidinium Salt. **Journal of The**

Electrochemical Society, v. 164, n. 7, p. F781–F789, 2017.

27 Dodelet, J.P.; Chenitz, R.; Yang, L.; Lefèvre, M. A new catalytic site for the electroreduction of oxygen? **ChemCatChem**, v. 6, n. 7, p. 1866–1867, 2014.

28 Strickland, K.; Miner, E.; Jia, Q.; Tylus, U.; Ramaswamy, N.; Liang, W.; Sougrati, M.T.; Jaouen, F.; Mukerjee, S. Highly active oxygen reduction non-platinum group metal electrocatalyst without direct metal-nitrogen coordination. **Nature Communications**, v. 6, p. 1–8, 2015.

29 Varnell, J.A.; Tse, E.C.M.; Schulz, C.E.; Fister, T.T.; Haasch, R.T.; Timoshenko, J.; Frenkel, A.I.; Gewirth, A.A. Identification of carbon-encapsulated iron nanoparticles as active species in non-precious metal oxygen reduction catalysts. **Nature Communications**, v. 7, p. 1–9, 2016.

30 Kumar, K.; Gairola, P.; Ranjbar-Sahraie, N.; Maillard, F.; Dubau, L.; Mermoux, M.; Zitolo, A.; Lions, M.; Jaouen, F. Physical and Chemical Considerations for Improving Catalytic Activity and Stability of Non-Precious-Metal Oxygen Reduction Reaction Catalysts. **ACS Catalysis**, v. 8, n. 12, p. 11264–11276, 2018.

31 Paulus, U.A.; Schmidt, T.J.; Gasteiger, H.A.; Behm, R.J. Oxygen reduction on a high-surface area Pt/Vulcan carbon catalyst: A thin-film rotating ring-disk electrode study. **Journal of Electroanalytical Chemistry**, v. 495, n. 2, p. 134–145, 2001.

32 Ravel, B.; Newville, M. ATHENA, ARTEMIS, HEPHAESTUS: Data analysis for X-ray absorption spectroscopy using IFEFFIT. **Journal of Synchrotron Radiation**, v. 12, n. 4, p. 537–541, 2005.

33 Zitolo, A.; Goellner, V.; Armel, V.; Sougrati, M.T.; Mineva, T.; Stievano, L.; Fonda, E.; Jaouen, F. Identification of catalytic sites for oxygen reduction in iron- and nitrogen-doped graphene materials. **Nature Materials**, v. 14, n. 9, p. 937–942, 2015.

34 Yuan, K.; Sfaelou, S.; Qiu, M.; Lützenkirchen-Hecht, D.; Zhuang, X.; Chen, Y.; Yuan, C.; Feng, X.; Scherf, U. Synergetic Contribution of Boron and Fe-N_x Species in Porous Carbons toward Efficient Electrocatalysts for Oxygen Reduction Reaction. **ACS Energy Letters**, v. 3, n. 1, p. 252–260, 2018.

35 Raymundo-Piñero, E.; Kierzek, K.; Machnikowski, J.; Béguin, F. Relationship between the nanoporous texture of activated carbons and their capacitance properties in different electrolytes. **Carbon**, v. 44, n. 12, p. 2498–2507, 2006.

36 Zúñiga, C.; Candia-Onfray, C.; Venegas, R.; Muñoz, K.; Urra, J.; Sánchez-Arenillas, M.; Marco, J.F.; Zagal, J.H.; Recio, F.J. Elucidating the mechanism of the oxygen reduction reaction for pyrolyzed Fe-N-C catalysts in basic media. **Electrochemistry Communications**, 2019.

37 Bard, A.J.; Faulkner, L.R. **Electrochemical methods: fundamentals and applications**. 2001.

38 Ramaswamy, N.; Mukerjee, S. Fundamental Mechanistic Understanding of Electrocatalysis of Oxygen Reduction on Pt and Non-Pt Surfaces: Acid versus Alkaline Media. **Advances in Physical Chemistry**, v. 2012, p. 1–17, 2012.

39 Tylus, U.; Jia, Q.; Strickland, K.; Ramaswamy, N.; Serov, A.; Atanassov, P.; Mukerjee, S. Elucidating oxygen reduction active sites in pyrolyzed metal-nitrogen coordinated non-precious-metal electrocatalyst systems. **Journal of Physical Chemistry C**, v. 118, n. 17, p. 8999–9008, 2014.

40 Pérez-Rodríguez, S.; Torres, D.; Lázaro, M.J. Effect of oxygen and structural properties on the electrical conductivity of powders of nanostructured carbon materials. **Powder Technology**, v. 340, p. 380–388, 2018.

41 Deng, D.; Yu, L.; Chen, X.; Wang, G.; Jin, L.; Pan, X.; Deng, J.; Sun, G.; Bao, X. Iron Encapsulated within Pod-like Carbon Nanotubes for Oxygen Reduction Reaction. **Angewandte Chemie - International Edition**, v. 52, n. 1, p. 371–375, 2013.

42 Zhu, J.; Xiao, M.; Liu, C.; Ge, J.; St-Pierre, J.; Xing, W. Growth mechanism and active site probing of Fe_3C@N-doped carbon nanotubes/C catalysts: guidance for building highly efficient oxygen reduction electrocatalysts. **Journal of Materials Chemistry A**, v. 3, n. 43, p. 21451–21459, 2015.

43 Watanabe, M. Design of Alloy Electrocatalysts for CO_2 Reduction. **Journal of The Electrochemical Society**, v. 138, n. 11, p. 3382, 1991.

44 Hu, Y.; Jensen, J.O.; Zhang, W.; Cleemann, L.N.; Xing, W.; Bjerrum, N.J.; Li, Q. Hollow spheres of iron carbide nanoparticles encased in graphitic layers as oxygen reduction catalysts. **Angewandte Chemie - International Edition**, v. 53, n. 14, p. 3675–3679, 2014.

45 Anderson, A.B.; Sidik, R.A. Oxygen Electroreduction on Fe^{II} and Fe^{III} Coordinated to N_4 Chelates. Reversible Potentials for the Intermediate Steps from Quantum Theory. **The Journal of Physical Chemistry B**, v. 108, n. 16, p. 5031–5035, 2004.

46 Yi, Y.; Weinberg, G.; Prenzel, M.; Greiner, M.; Heumann, S.; Becker, S.; Schlögl, R. Electrochemical corrosion of a glassy carbon electrode. **Catalysis Today**, v. 295, n. July, p. 32–40, 2017.

47 Freitas, K.S.; Concha, B.M.; Ticianelli, E.A.; Chatenet, M. Mass transport effects in the borohydride oxidation reaction - Influence of the residence time on the reaction onset and faradaic efficiency. **Catalysis Today**, v. 170, n. 1, p. 110–119, 2011.

48 A. Schneider, L. Colmenares, Y. E. Seidel, Z. Jusys, B. Wickman, B.K. and R.J.B. Transport effects in the oxygen reduction reaction on nanostructured, planar glassy carbon supported Pt/GC model electrodes. **Physical Chemistry Chemical Physics**, v. 10, p. 1931–1943, 2008.

49 Serov, A.; Artyushkova, K.; Andersen, N.I.; Stariha, S.; Atanassov, P. Original Mechanochemical Synthesis of Non-Platinum Group Metals Oxygen Reduction Reaction Catalysts Assisted by Sacrificial Support Method. **Electrochimica Acta**, v. 179, p. 154–160, 2015.

50 Goellner, V.; Armel, V.; Zitolo, A.; Fonda, E.; Jaouen, F. Degradation by Hydrogen Peroxide of Metal-Nitrogen-Carbon Catalysts for Oxygen Reduction. **Journal of The Electrochemical Society**, v. 162, n. 6, p. H403–H414, 2015.

51 Osmieri, L.; Monteverde Videla, A.H.A.; Armandi, M.; Specchia, S. Influence of different transition metals on the properties of Me–N–C (Me = Fe, Co, Cu, Zn) catalysts synthesized

using SBA-15 as tubular nano-silica reactor for oxygen reduction reaction. **International Journal of Hydrogen Energy**, v. 41, n. 47, p. 22570–22588, 2016.

52 Osmieri, L.; Monteverde Videla, A.H.A.; Ocón, P.; Specchia, S. Kinetics of Oxygen Electroreduction on Me-N-C (Me = Fe, Co, Cu) Catalysts in Acidic Medium: Insights on the Effect of the Transition Metal. **Journal of Physical Chemistry C**, v. 121, n. 33, p. 17796–17817, 2017.

53 Chen, R.; Li, H.; Chu, D.; Wang, G. Unraveling Oxygen Reduction Reaction Mechanisms on Carbon-Supported Fe-Phthalocyanine and Co-Phthalocyanine Catalysts in Alkaline Solutions. **J. Phys. Chem. C**, v. 113, n. 2, p. 20689–20697, 2009.

54 Goenaga, G.A.; Roy, A.L.; Cantillo, N.M.; Foister, S.; Zawodzinski, T.A. A family of platinum group metal-free catalysts for oxygen reduction in alkaline media. **Journal of Power Sources**, v. 395, n. February, p. 148–157, 2018.

55 Chlistunoff, J. RRDE and voltammetric study of ORR on pyrolyzed Fe/polyaniline catalyst. On the origins of variable Tafel slopes. **Journal of Physical Chemistry C**, v. 115, n. 14, p. 6496–6507, 2011.

56 Santori, P.G.; Speck, F.D.; Li, J.; Zitolo, A.; Jia, Q.; Mukerjee, S.; Cherevko, S.; Jaouen, F. Effect of Pyrolysis Atmosphere and Electrolyte pH on the Oxygen Reduction Activity, Stability and Spectroscopic Signature of FeN_x Moieties in Fe-N-C Catalysts . **Journal of The Electrochemical Society**, v. 166, n. 7, p. F3311–F3320, 2019.

57 Lee, J.S.; Park, G.S.; Kim, S.T.; Liu, M.; Cho, J. A highly efficient electrocatalyst for the oxygen reduction reaction: N-doped ketjenblack incorporated into Fe/Fe_3C-functionalized melamine foam. **Angewandte Chemie - International Edition**, v. 52, n. 3, p. 1026–1030, 2013.

58 Kim, J.H.; Sa, Y.J.; Jeong, H.Y.; Joo, S.H. Roles of Fe−N_x and Fe−Fe_3C@C Species in Fe−N/C Electrocatalysts for Oxygen Reduction Reaction. **ACS Applied Materials and Interfaces**, v. 9, n. 11, p. 9567–9575, 2017.

59 Gokhale, R.; Chen, Y.; Serov, A.; Artyushkova, K.; Atanassov, P. Direct synthesis of platinum group metal-free Fe-N-C catalyst for oxygen reduction reaction in alkaline media. **Electrochemistry Communications**, v. 72, p. 140–143, 2016.

Chapter 2

Electrocatalytic Features of Fe-N-C and Co-N-C Catalysts under Alkaline Degradant Conditions towards Oxygen Reduction Reaction

2.1 Introduction

Electrochemical energy conversion devices have been pointed as available technologies for the world transition from fossil to renewable energies. Among these, fuel cells act efficiently and cleanly in the conversion of the stocked chemical energy of hydrogen (or another fuel) into electricity. In this respect, acidic-operation devices (*i. e.* PEMFC; proton-exchange membrane fuel cell) lie in a more advanced stage regarding the activity and durability of the catalysts for HOR (hydrogen oxidation reaction) and ORR (oxygen reduction reaction).[1] On the ORR side, a new class of PGM (platinum-group-metals)-free materials formed by metal and nitrogen-doped carbons (Metal-N-C) arises as promising catalysts. Briefly, the degradation of Metal-N-C (where Metal is Fe or Co) catalysts take place mainly by four pathways in acidic conditions: (i) mild oxidation of carbon matrix,[2] (ii) anion adsorption on protonated highly basic nitrogen groups,[3] (iii) demetallation of the center metallic[4] and (iv) carbon corrosion followed by metal loss from center metallic.[4,5]

Meanwhile, in alkaline media, many metals are thermodynamically more stable due to the passivation of them.[6] Similarly, the carbon matrix can be passivated by solid carbonates, in opposition to the release of the stable CO_2 at low pH.[7,8] On the kinetics parameters there is a facility for ORR due to the inner and outer-sphere electron transfer mechanism caused by a slight change in double-layer structure at high pH.[9] Thus, significant researches about Metal-N-C catalyst in alkaline-operation devices (*i. e.* AEMFC; anion-exchange membrane fuel cell) has grown in last years, due to these advantages over acidic conditions, besides the fuel versatility.[10–13] Further, Metal-N-C material has high activity for ORR electrocatalysis at least similar (or even higher) of the onset and half-wave potential of the benchmark carbon-supported platinum nanoparticles (Pt/C) in most cases.[14–17] Its high activity is mainly attributed to the active site of metal nanoparticles surrounded by nitrogen-doped carbon shell (M@N-C) than the counterpart atomically dispersed metal (M-N_xC_y);[18] with the iron as the most active center metallic.[18,19] M-N-C catalysts have shown tolerance to the possible occurrence of the *crossover* effect caused by fuel migration, as alcohols and borohydride, from anode to cathode compartment.[12,16,20]

Since electrocatalyst durability is a key issue for its application, the Fuel Cell Commercialization Conference of Japan (FCCJ)[21] have proposed protocol guidelines for durability tests in acidic conditions, usually labeled as accelerated stress tests (ASTs). Hence, some studies have been adapted to these guidelines protocol to be applied under alkaline conditions (*e.g.*, 0.1 mol L^{-1} KOH or NaOH). As an initial comparison, it has been remarked that the benchmark carbon-supported platinum nanoparticles catalyst undergoes strongly depletion over time, even in short-term durability tests [22,23] mainly attributed to a large decrease of ECSA (electrochemical surface area), caused by metal agglomeration and detachment.[24,25] On the other hand, Metal-N-C catalysts exhibit a decrease of the half-wave potential by few tens millivolts after short-term degradation tests. The number of investigations of the durability of this class of catalysts in short-term conditions has increased in the last years, mainly for the most active materials: Fe-N-C and Co-N-C,[26,27] which has allowed quite good initial understanding of their degradation mechanism in alkaline media.

The superior durability of metal or metal-carbide particles encapsulated by a protective multilayered graphitized nitrogen-carbon shell is commonly related to the raise of the carbon crystallinity that protects the metallic-based centers during degradation tests.[23,27–30] A mixed catalyst containing Fe_3C nanoparticles and Fe-N_xC_y moieties achieved well-defined stability, as demonstrated by their retaining of the morphological and crystalline structures [31] that maintain the O_2-reduction proceeding by the 4-electrons mechanism.[32] Using square-wave potential-cycling's (a higher degradant test), Fe_3C undergoes a decrease of electrochemical activity after 10,000 cycles, while it remains constant for Fe-N_xC_y even after 60,000 cycles under Ar-saturated alkaline electrolytes at 25 °C.[33] This indicates higher long-term stability of Fe-N_xC_y moieties compared to the Fe_3C nanoparticles, this latter seeming to degrade slowly but continuously under this condition.

Comparing the effect of the pyrolysis conditions used for preparation of Fe-N-C catalysts (Ar *vs*. NH_3 atmosphere), on the stability of Fe-N_xC_y moieties it is seen that the metal leaching is slightly less intense in the latter catalyst due to the higher surface area of nitrogen-doped carbon.[34] Carbon property is another important parameter that controls the durability of the catalysts, particularly when the porosity and wettability are considered. The ORR mass activity of catalysts based on graphene presents a less intense decrease compared to nanotubes and active carbon, with the graphene support evidencing production of CO_2 coming from carbon oxidation starting at higher anodic potentials.[35] Further, catalysts with carbons containing mixed porosity, such as macro and mesopores[36] and micro and mesopores[37], preserved intact their porosity and electrocatalytic parameters, and, thus the electrolyte transport and accessibility to FeN_xC_y active sites. Thereby, the causes of degradation and/or long-term durability of the Metal-N-C catalysts still lie in the first steps under alkaline conditions regarding the ORR electrocatalysis.

Herein, the degradation mechanism of Metal-N-C catalysts has been investigated in alkaline conditions, where M-N-C comprised Fe-catalysts ($Fe_{0.5}$ and $Fe_{5.0}$) and Co-catalysts ($Co_{0.5}$ and $Co_{5.0}$), in the form of atomic dispersion ($M_{0.5}$) and metal-based nanoparticles ($M_{5.0}$). The main results showed that atomically dispersed iron forms Fe-based nanoparticles after degradation under the O_2-atmosphere at 60 °C and 25 °C, and the temperature change the size of them. In addition, the degradation mechanism of the atomic dispersion takes place mainly by metal leaching from catalyst to electrolyte, while, for metal nanoparticles, the metal leaching act together nitrogen and carbon partial oxidation on the surface. To get these results the catalysts were submitted to accelerated stress tests under Ar- and O_2-saturated 0.1 mol L^{-1} NaOH electrolytes at 60 and 25 °C. Cyclic voltammetry (CV) and ORR polarization curves measurements have been carried out before and after 10,000 loading cycles between 0.6 to 1.0 V *vs.* RHE. Physicochemical characterization of catalysts has been conducted, for fresh and aged Metal-N-C catalysts, by x-ray photoelectron (XPS) and Raman spectroscopies, x-ray diffraction (XRD), transmission electron microscopy (TEM), energy-dispersive x-ray spectroscopy (X-EDS) and inductively coupled plasma-mass-spectrometry (ICP-MS).

2.2 Experimental Section

2.2.1 Electrocatalysts and Catalytic Layers

Four different M-N-C electrocatalysts were synthesized using zinc(II) zeolitic imidazolate framework ZIF-8 (purchased from BASF, Basolite Z1200), metal(II) acetate (Fe or Co) and 1,10-phenanthroline mixed via dry planetary ball milling in the optimized ratio, followed by pyrolysis step at 1050 °C, as detailed described in [38]. The catalysts are labeled as M_x in this study, where M is the nature of the metal (Co or Fe) and x is the concentration of the metal employed in the synthesis before pyrolysis (0.5 or 5.0 wt.%).

To evaluate the electrochemical properties and durability of the materials, the catalytic layers were made from inks based on ultrasonically homogenized dispersion of the catalytic powders (10 mg) in a mixture of 5 wt.% Nafion® solution (50 µL, Sigma-Aldrich), isopropanol (854 µL, Carl Roth) and ultrapure water (372 µL, Millipore, 18.2 MΩ cm, 1−3 ppm TOC).[4] To form the catalytic layers, aliquots of 20 µL were dropped onto the glassy carbon disc substrate of rotating disk electrode (RDE; 0.196 cm^2), following by drying using a heat gun, under controlled rotation speed to obtain a catalyst loading of 0.8 mg_{powder} cm^{-2}.

2.2.2 Electrochemical measurements

To avoid contaminations, all glassware, electrodes, volumetric flasks and polytetrafluoroethylene(PTFE)-based materials were cleaned in 50 % v/v solution of H_2SO_4 (Merck, Suprapur 96 wt.%) / H_2O_2 (Carl Roth, 30% w/w) followed by washing in fresh and hot ultrapure water (Millipore, 18.2 MΩ cm, 1−3 ppm TOC). The glassy carbon materials were polished with diamond polishing paste (3 and 1 microns, Presi). The alkaline electrolyte was prepared from NaOH (Alfa Aesar, 50% w/w aq. soln.) to a final concentration of 0.1 mol L^{-1}.

Electrochemical measurements were performed using an Autolab potentiostat (PGSTAT302N) connected to the three-electrode electrochemical cells. In this study, two different PTFE cells were used, one exclusively for the CVs and ORR polarization curves at 25 °C and the other for the accelerated stress tests (ASTs) at 60 °C and 25 °C. Both PTFE cells contained a Luggin capillary for connecting a commercial reversible hydrogen reference electrode (RHE, Hydroflex, Gaskatel GmbH) and carbon sheet counter electrodes. A Pt-wire immersed in the electrolyte was used to filter the high-frequency electrical noise. For supporting the working electrode, a homemade glassy carbon cylinder (Sigradur® from Hochtemperatur-Werkstoffe GmbH) embedded in a PTFE cylinder coupled to a rotation rate control system was used.

Electrochemical measurements on the thin films, stated by conducting 50 consecutive cyclic voltammograms (CVs) in the range of 0.0 and 1.0 V *vs.* RHE at 100 mV s^{-1} in Ar-purged 0.1 mol L^{-1} NaOH; this was followed by recording CVs at 10 and 5 mV s^{-1} scan rates. Then, ORR polarization curves corrected from Ohmic drop were obtained at 5 mV s^{-1} and 1600 rpm in the O_2-saturated electrolyte. This procedure was repeated before and after 500, 1,000 and 10,000 potential cycles, this comprising the accelerated stress test (AST) protocol. These tests were conducted using 0.6 and 1.0 V *vs.* RHE square-wave steps, holding the potential during 3 s.[21] The 0.1 mol L^{-1} NaOH electrolytes were purged with Ar or O_2 gas and kept in the controlled temperature of 60 °C; for comparison, measurements were also performed at 25 °C.

The degradation of the catalysts was tracked by the values of kinetic current densities for ORR (i_k) obtained at 1600 rpm, calculated according to the Koutecky Levich equation (Equation 1):

$$i_k = -\frac{(i_L . i)}{(i_L - i)} \qquad (1)$$

where i_L = oxygen-diffusion limited current density at 0.2 V and i = Faradaic current obtained with capacitive current subtractions at different electrode potentials (with Ohmic drop correction). The i_k values were then normalized by the mass (m) of the catalyst layer on the glassy carbon electrode, and these were taken as the catalyst mass activity, i_{MA}.

2.2.3 X-ray Photoelectron Spectroscopy (XPS)

XPS data were obtained on a Thermo Scientific K_α spectrometer with a monochromated Al x-ray source (hν = 1486.6 eV and spot size 400 μm) measured directly onto the glassy carbon disc substrate with the catalytic layer. Binding energies were corrected to the reference of the C-C component of C 1s peak at 284.3 eV. The XPS spectra of O 1s, N 1s and C 1s were deconvoluted using CasaXPS software to obtain the surface composition of the catalysts.

2.2.4 Raman Spectroscopy

The Raman spectra were recorded on a Renishaw inVia Raman system using an argon Laser (514 nm) operated near to 5 mW. A Peltier-cooled charge-coupled device camera (CCD) was the detector with a spectral resolution of approximately 1 cm^{-1}. The measurements were performed with an objective model X50 ULWD in a backscattering configuration. All Raman spectra were normalized by the intensity of the G band (*ca*. 1580 cm^{-1}).

2.2.5 Transmission Electron Microscopy (TEM) and Energy-Dispersive X-ray Spectroscopy (X-EDS)

The electrocatalytic materials were investigated with a JEOL 2010 TEM instrument operated at 200 kV with a point-to-point resolution of 0.19 nm. X-EDS spectra were obtained in at least 6 different regions of the TEM grid. The quantification analysis was performed on the Fe K and Co K lines, using K-factors determined by the JEOL software.

2.2.6 X-ray Diffraction (XRD)

XRD patterns were obtained using a D8 Advance X-ray diffractometer (Bruker) operated at 40 mA and 40 kV, using Ni-filtered Cu Kα X-ray radiation (λ= 1.5406 Å). The 2θ angle ranged from 10 to 100 ° stepped by 0.02 ° with step-time of 0.5 s. The crystallite size of the metallic structures was determined using Scherrer's equation.

2.2.7 Inductively Coupled Plasma-Mass-Spectrometry (ICP-MS)

The amount of Fe and Zn dissolved in the electrolyte was determined using a PerkinElmer NexION 2000 inductively coupled plasma mass spectrometer (ICP-MS). The Fe and Zn calibration curves were obtained from metal standard solutions (ICP Multi-Element Standard Solution, 28 elements, 1 mg L^{-1}, Carl Roth GmbH & Co. KG), previously diluted with 50:50 v/v solution of NaOH 0.1 mol L^{-1} and 2 % nitric acid (Merck, Suprapur® HNO_3, 65 %) to obtain analytical concentrations of 5, 10, 20 and 50 µg L^{-1} for each metal. The collected electrolyte was diluted with a 2% HNO_3 solution to decrease the aliquot's pH and bring the analyte concentrations into the specified calibration ranges. Sample and calibration solutions were spiked with a 25 µg L^{-1} of ^{45}Sc internal standard solution (PerkinElmer, N9303832) for the detection of ^{57}Fe and ^{64}Zn. To attenuate polyatomic interferences (*e.g.* ^{40}Ar and ^{16}O), the detection of ^{57}Fe and ^{64}Zn was performed in Helium collision mode with kinetic energy discrimination (KED).

2.3 Results and Discussion

2.3.1 Structural, Surface and Chemical Properties of Metal-N-C Electrocatalysts

The physicochemical characteristics of the catalysts assessed by using the X-ray absorption (XAS), Raman, ^{57}Fe Mössbauer spectroscopy, TEM, X-EDS, XRD and BET techniques have been detailed in previously published works.[2,4,38,40,41] Therefore, here we only present a brief overview of the chemical and structural properties for the $M_{0.5}$ and $M_{5.0}$ catalysts. $M_{0.5}$ materials contain only atomically dispersed metal dispersed on a nitrogen-doped carbon matrix, designated as $M\text{-}N_xC_y$. These catalysts present a metal content of *ca.* 1.5 wt.%

after the pyrolysis step, and high values of BET specific surface areas due to the large presence of mesopores and micropores structures. Whereas $M_{5.0}$ electrocatalysts contain metallic nanoparticles (Co or Fe_3C) embedded in a nitrogen-doped carbon shell, designated as M@N-C and their metal content is 15 wt.% after pyrolysis. Their carbon structures exhibit more graphitic organizations than $M_{0.5}$ catalysts and present low BET specific surface areas. The previous finding demonstrates that in alkaline conditions: (i) $M_{5.0}$ catalysts have higher ORR mass activity compared to the $M_{0.5}$ materials; (ii) Fe-based catalysts (Fe@N-C and Fe-N_xC_y) show greater activity towards ORR electrocatalysis compared to the corresponding Co-based materials; (iii) Fe-based catalysts are the most effective for O_2-reduction to OH^- ion, thus involving 4-electrons per oxygen molecule.[18]

Transmission electron microscopy (TEM) measurements have been used to characterize possible changes in the nanoparticles of the metallic center before and after the ASTs load cycling in Ar- and O_2-purged electrolytes, as shown Figure 2.1. In agreement with previous work,[4,18] images for both raw $M_{0.5}$ catalysts indicate the absence of particles distributed over the materials, while for $M_{5.0}$ the presence of nanoparticles is clearly noted. Also, images in Figure 2.1a-d *vs*. 2.1e-h show that no significant differences in aspects are seen between fresh and aged catalysts in all cases when the ASTs comprised 10,000 cycles at 60 °C in Ar-purged electrolytes. In the case of Co-catalysts, these similarities are extended to the cases of O_2-purged electrolytes (Figures 2.1k,l). However, under this last cycling condition, in the case of $Fe_{5.0}$, a growth of the nanoparticles is evidenced when it is cycled at 60 °C under O_2 (Figure 2.1j), and in the case of $Fe_{0.5}$ formation of nanoparticles is seen when it is cycled at 60 °C (Figure 1i) and 25 °C (Figure 2.1m). These results could indicate the occurrence of iron dissolution from Fe-N_xC_y moieties ($Fe_{0.5}$) or from the original nanoparticles in $Fe_{5.0}$ and their redeposition, forming or growing iron-based nanoparticles. Indeed, the occurrence of dissolution/growth processes has been also found when the AST is conducted under Ar-purged electrolyte at 25 °C, but only after 60,000 cycles, as reported previously for atomically dispersed iron.[33]

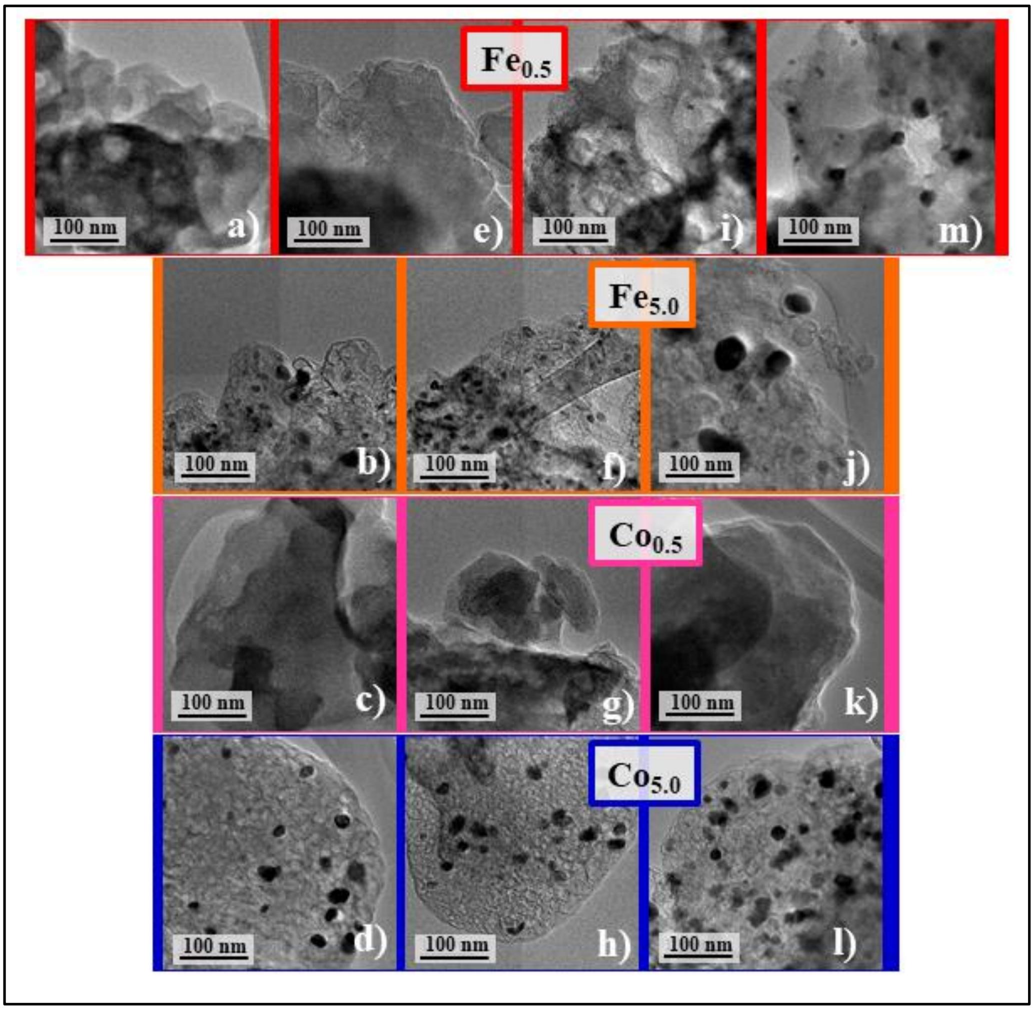

Figure 2.1. Representative transmission electron microscopy images of the $Fe_{0.5}$ (red), $Fe_{5.0}$ (orange), $Co_{0.5}$ (magenta) and $Co_{5.0}$ (blue) catalysts. For **(a-d)** fresh catalysts and aged catalysts after 10,000 cycles under **(e-h)** Ar at 60 °C, **(i-l)** O_2 at 60 °C and **(m)** O_2 at 25 °C.

Particle size histograms obtained from TEM images (Figure A2.1) denote that, particularly in the case of the $Fe_{0.5}$ electrocatalyst, the increase of electrolyte temperature during the AST leads to a decrease of the size of redeposited nanoparticles (from *ca*. 20.7 nm and 8.24 nm for 25 °C and 60 °C, respectively). For $Fe_{5.0}$, histograms show that the particle sizes remain the same before (*ca*. 17.2 nm) and after AST under Ar (*ca*. 15.5 nm), but it is increased to *ca*. 35.8 nm after AST in the O_2-saturated electrolyte. Possibly, the increase of particle size mentioned above for $Fe_{0.5}$ and $Fe_{5.0}$ is a consequence of iron oxidation, followed by the growth of an iron oxide phase during AST under O_2. Also, iron carbide agglomeration should be considered in the $Fe_{5.0}$ catalyst. For the $Co_{5.0}$ catalyst, the nanoparticles remain almost unaltered presenting an average size of *ca*. 23.9 nm before the ASTs and *ca*. 21.5 nm and *ca*. 26.9 nm after-AST under Ar and O_2, respectively.

Measurements by energy-dispersive x-ray spectroscopy (X-EDS) of all catalysts were carried out to characterize the metal content in the samples before and after the ASTs. These data were used to obtain the normalized values ($[\text{metal}]_{\text{final}}/[\text{metal}]_{\text{initial}}$) of atomic percentages (respect to the uncycled sample) of metals remaining after 10,000 cycles of ASTs in the different conditions, and these results are shown in Figure 2.2a. The concentrations of released metal ($[\text{metal}]_{\text{final}} – [\text{metal}]_{\text{initial}}$) in parts per billion (ppb) along the AST have obtained from inductively coupled plasma mass spectrometry (ICP-MS) analyses of the electrolytes used in the AST for the iron-based catalysts, as shown Figures 2.2b and 2.2c. X-EDS results (Figure 2.2a) for ASTs at 60 °C under either Ar and O_2 conditions, the materials present two distinguished trends in the catalytic layer: (i) the $M_{0.5}$ ($Fe_{0.5}$ and $Co_{0.5}$) catalysts remain with the metal content between 60 % to 40 % of initial atomic percentage; (ii) $M_{5.0}$ ($Fe_{5.0}$ and $Co_{5.0}$) catalysts have between 90 % to 80 % of start metallic concentrations. These results reveal that the metallic center embedded in a nitrogen-carbon shell has more resistance to corrosion caused by a more stabilized chemical ambient of nanoparticles and/or less extended contact between metal and the alkaline electrolyte. Further, the AST conditions concerning the Ar or O_2-purged electrolytes at 60 °C do not show a clear correlation with the remaining metallic center.

In contrast, it is very interesting to observe that, when the AST is conducted at 25 ^{o}C there is absolutely no demetallation for $Fe_{0.5}$ catalyst, as indicated by the X-EDS and by ICP-MS results. In these conditions, iron species eventually leached from the Fe-N_xC_y moieties seem to be completely redeposited as nanoparticles resulting in a constant value of iron in the catalyst, as measured by X-EDS. Further, the trace iron-containing in the pure electrolyte seems to be partially deposited on the catalysts, as shown by the lower values ($[\text{metal}]_{\text{final}} – [\text{metal}]_{\text{initial}} < 0$ ppb) of the iron content in the electrolyte after the AST potential cycles, as obtained by ICP-MS. These observations are completely consistent with the TEM results in Figure 2.1 for the $Fe_{0.5}$ catalyst, for which the presence of iron-based nanoparticles is noted after the AST conducted at 25 ^{o}C under O_2.

Zn(II) zeolitic Metal-Organic Framework (MOF, ZIF-8) has been used as templates for preparing the M-N-C catalysts to generate micropores structures resulting from MOF residues releasing during the pyrolysis step.[20,42] Here, results in Figure 2.2c that at moderate pH conditions zinc species are as $Zn(OH)_2$ that dissolves as $HZnOO^-$ and $ZnOO^{2-}$ at higher pH (Equations 2-3),[43] as, particularly for the $Fe_{0.5}$ catalysts when it is cycled under O_2 atmosphere.

$Zn(OH)_2 + OH^- \rightarrow HZnOO^- + H_2O$ (2)

$Zn(OH)_2 + 2\ OH^- \rightarrow ZnO_2^{2-} + 2\ H_2O$ (3)

X-ray diffraction (XRD) measurements have been used to characterize changes in the crystalline structures of the metallic center before and after the AST load cycles in O_2-purged electrolytes, as shown Figure 2.2c and 2.2d. From XRD results, the following points are evident: i) for the $M_{0.5}$ materials the patterns are very similar to those of carbon, with the features at *ca*. 25 ° and 45 °, corresponding to diffraction of the (002) and (100) planes of graphitic zones respectively. Signals related to the nanoparticles detected by TEM after some ASTs are not at all evidenced, but this may be because these particles correspond to amorphous iron-based species, which would be seen as a large low intense peak coinciding with the 25 ° and 45 ° peaks of carbon; ii) considering the $M_{5.0}$ catalysts, in the case of iron the intense diffraction peaks at *ca*. 42.9 °, 43.8 °, 44.6 °, 45.0 °, 45.9 °, 48.6 ° and 49.1 ° evidence the presence of crystalline Fe_3C, before and after AST with crystallite sizes of *ca*. 33.3 nm and 32.3 nm, respectively.

The formation *in situ* of nanoparticles detected for $Fe_{0.5}$ can be a consequence of iron oxidation, followed by the growth of an amorphous iron-based phase during AST under O_2. Thus, we proposed a mechanism that starts from the oxidation of Fe^{2+} from $Fe\text{-}N_xC_y$ moieties to Fe^{3+} (Equation 4) since the redox potential of Fe^{3+}/Fe^{2+} ($E° = 0.77$ V [44]) is into the potential range of ASTs (0.6 to 1.0 V *vs*. RHE). Then, Fe^{3+} species are converted to amorphous Fe-based species. In the case of $Fe_{5.0}$ catalyst, a similar oxidation process has been observed for Fe_3C in the presence of Mo_2C structures in neutral and alkaline media, [45] however, iron carbide agglomeration also should be considered as a likely process along the ASTs under O_2.

For $Co_{0.5}$, the formation *in situ* of Co-based nanoparticles is hindered due to the highest values of $Co^{3+/}Co^{2+}$ redox potential ($E° = 1.92$ V [44]) above the potential window applied along ASTs. For $Co_{5.0}$, XRD peaks evidence the presence of a major phase of metallic Co, but also some Co_3O_4 and CoOOH. In the case of metallic Co, the crystallite sizes remain essentially constant even after 10,000 loading cycles after both AST conditions. Since it is known that Co nanoparticles passivate after forming a thin layer of $Co(OH)_2$ from a solid-state oxidation process at less than 1.0 mol L^{-1} OH^- concentrations,[46] and this oxidizes to Co_3O_4 at $E^o = 0.73$ V (reversible process at $E > 1.0$ V *vs*. RHE) and CoOOH at $E^o = 0.87$ V (irreversible process), as shown by Equations 4-5 respectively.[47,48]

$$3\ Co(OH)_2 + 2\ OH^- \rightarrow Co_3O_4 + 4\ H_2O + 2\ e^- \quad (4)$$

$$Co(OH)_2 + OH^- \rightarrow CoOOH + H_2O + e^- \quad (5)$$

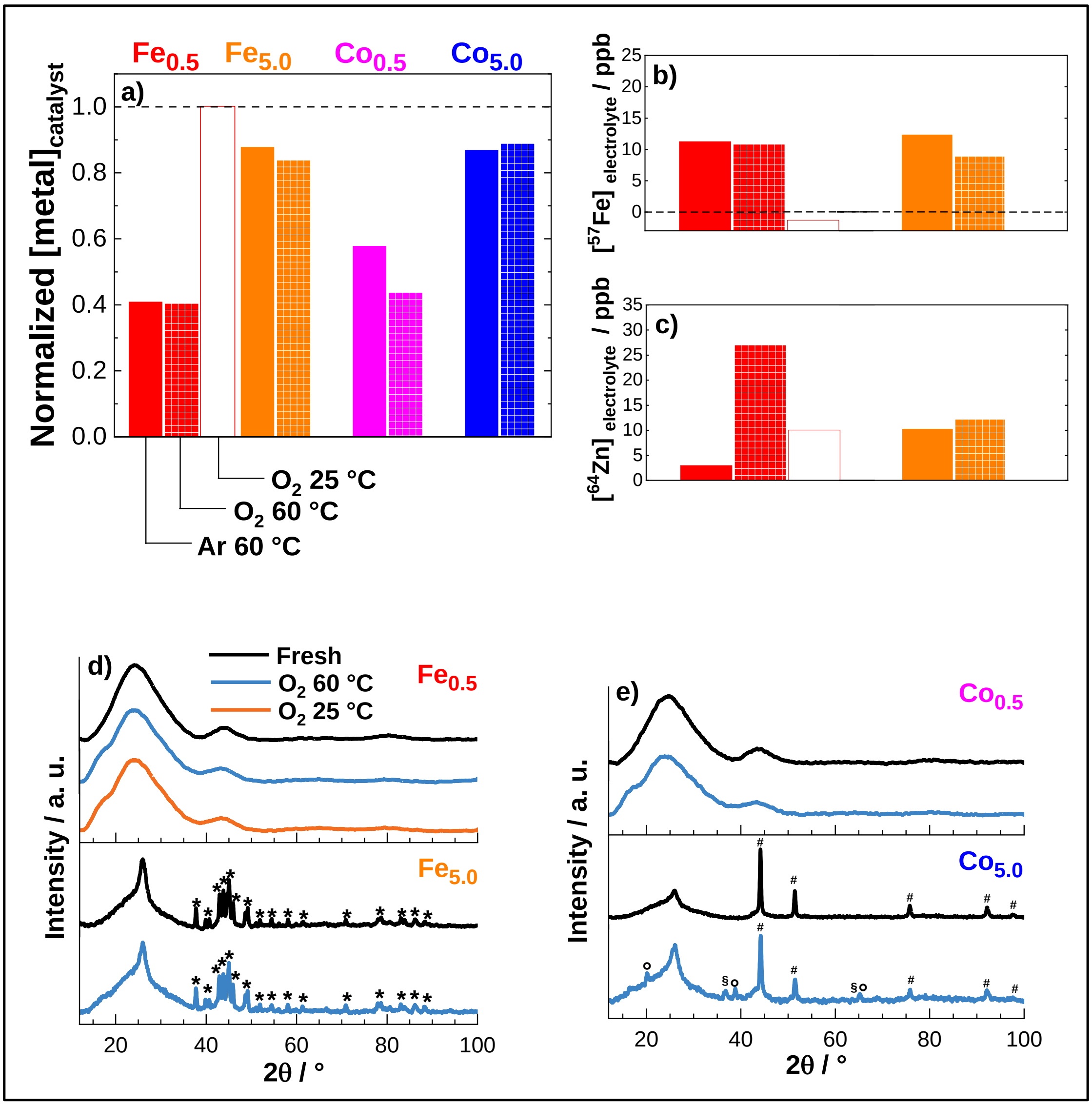

Figure 2.2. **(a)** Normalized metal content ($[metal]_{final}/[metal]_{initial}$) in the Co and Fe-catalysts measured by X-EDS and **(b)** metal leached ($[metal]_{final} – [metal]_{initial}$) from the Fe-catalysts either after 10,000 AST loading cycles in Ar and O_2-saturated 0.1 mol L^{-1} NaOH at 60 °C (also at 25 °C and O_2 for $Fe_{0.5}$). **(c)** x-ray diffraction patterns of the catalysts before and after 10,000 load cycling under O_2-purged electrolytes at 60 °C and 25 °C. The main crystalline structures indexed: (*) Fe_3C (PDF 85-1317), (#) Co (PDF 15-0806), (§) Co_3O_4 (65-3103) and (°) CoOOH (72-2280).

Possible chemical and structural changes of the nitrogen-doped carbon matrix on the M-N-C catalysts caused by the ASTs were evaluated by x-ray photoelectron spectroscopy (XPS) and Raman spectroscopy. Figure 2.3a, 2.3b and 2.3c show the deconvoluted O 1s, N 1s and C1s

XPS signals for the Fe-based catalysts, before and after the 10,000 AST loading cycles under Ar-purged electrolyte.

Fittings of the O 1s XPS signal (Figure 2.3a) were more consistent when considering four types of possible bonds with carbon, reported in the literature, [49–51] and corresponding to C=O/O=C-OH (O doubly-bonded with C, 531.2 - 531.4 eV), C-O-H/C-O-C (532.1 eV), O=C-OH/O=C-OR (O singly-bonded with C, 533.0 – 533.3 eV) and peroxyacid/peroxyester (535.1 - 535.3 eV). Indeed, these results show that the oxygen atoms in the Fe-based catalysts are participating in C-O-H/C-O-C bonds, corresponding to 39.0 and 55.8 at.% for $Fe_{0.5}$ and $Fe_{5.0}$, respectively, as detailed in Table A2.1 (see Appendix 2). Results in Figure 2.3a also evidence that degradation of these oxygen functional groups is higher in $Fe_{5.0}$ than in $Fe_{0.5}$, which is mainly related to the conversion of C-O-H into C=O/O=C-OH functional groups (+ 15.2 %). This behavior is explained by an oxidative process that takes place following the sequence of two electrons transfer on the catalytic surface at high potentials in alkaline media.[52,53] Since the complete oxidation of carbon structures releasing CO_3^{2-} to electrolyte starts from more anodic potentials (*E* > 1.1 V *vs.* RHE),[17,35] the oxidative process that occurs here should be considered a partial oxidation process to C=O and/or O=C-OH. During AST loading-cycles for $Fe_{5.0}$, a portion of C-O-H functional groups are oxidized involving two-electrons transfer to C=O, then it is oxidized to O=C-OH functional groups involving more two-electrons with a local releasing of H^+ species, as proposed by Equations 6-7 and confirmed by XPS measurements.

$$\text{R-[C-O-H]} \rightarrow \text{R-[C=O]} + 2\ \text{H}^+ + 2\ \text{e}^- \qquad (6)$$

$$\text{R-[H-C=O]} + \text{H}_2\text{O} \rightarrow \text{R-[O=C-OH]} + 2\ \text{H}^+ + 2\ \text{e}^- \qquad (7)$$

The N 1s spectra (Figure 2.3b) of the iron-based catalysts obtained before and after the AST were consistently deconvoluted into four N-bondings: pyridinic (C=N-C), pyrrolic (C-(NH)-C), graphitic (C-(NC)-C) and oxidized (O=N-C), corresponding to 398.0 – 398.4 eV, 399.8 – 400.2 eV, 401.4 eV and 403.4 eV binding energies, respectively.[54–57] Among these species, the more abundant form is the pyrrolic-N, which is at proportions of 69.3 at.% for $Fe_{0.5}$ and 78.6 at.% for $Fe_{5.0}$ (see details in Table S1). Results for the samples before and after AST, evidence similar changes of N 1s spectra, like those found for O 1s, that is, the more graphitized catalyst ($Fe_{5.0}$) undergoes more degradation than the atomic dispersed material ($Fe_{0.5}$). Despite the high stability of aromatic pyrrolic nitrogen, in the $Fe_{5.0}$ catalyst this functional group is converted and/or rearranged to pyridinic (+ 4.7 at.%), graphitic (+ 6.0 at.%) and oxidized (+ 6.0 at.%) nitrogen species. Findings are in agreement with the literature for nitrogen-doped carbon materials.[58] The conversion of pyrrolic to oxidized nitrogen functional groups can be explained by the oxidative process, as proposed above. The electrosynthesis of some oxidized-pyrrole species has been described to occurs on maximum yield at E > 1.3 V *vs.* RHE in non-aqueous electrolytes;[59,60] substituted and unsubstituted pyrrole species are also electrooxidized in aqueous electrolytes.[61–63] In the case of pyrrolic to pyridinic/graphitic functional group conversion, the formation may be attributed to the multistep rearrangement between surface species from the oxidative process and/or initial functional groups. The higher stability of the nitrogen-bonds observed by XPS for the $Fe_{0.5}$ catalyst (Figure 2.3b) evidence that the oxidation not appreciable occurs on the surface/near-surface of the atomically dispersed iron coordinated nitrogen structures.

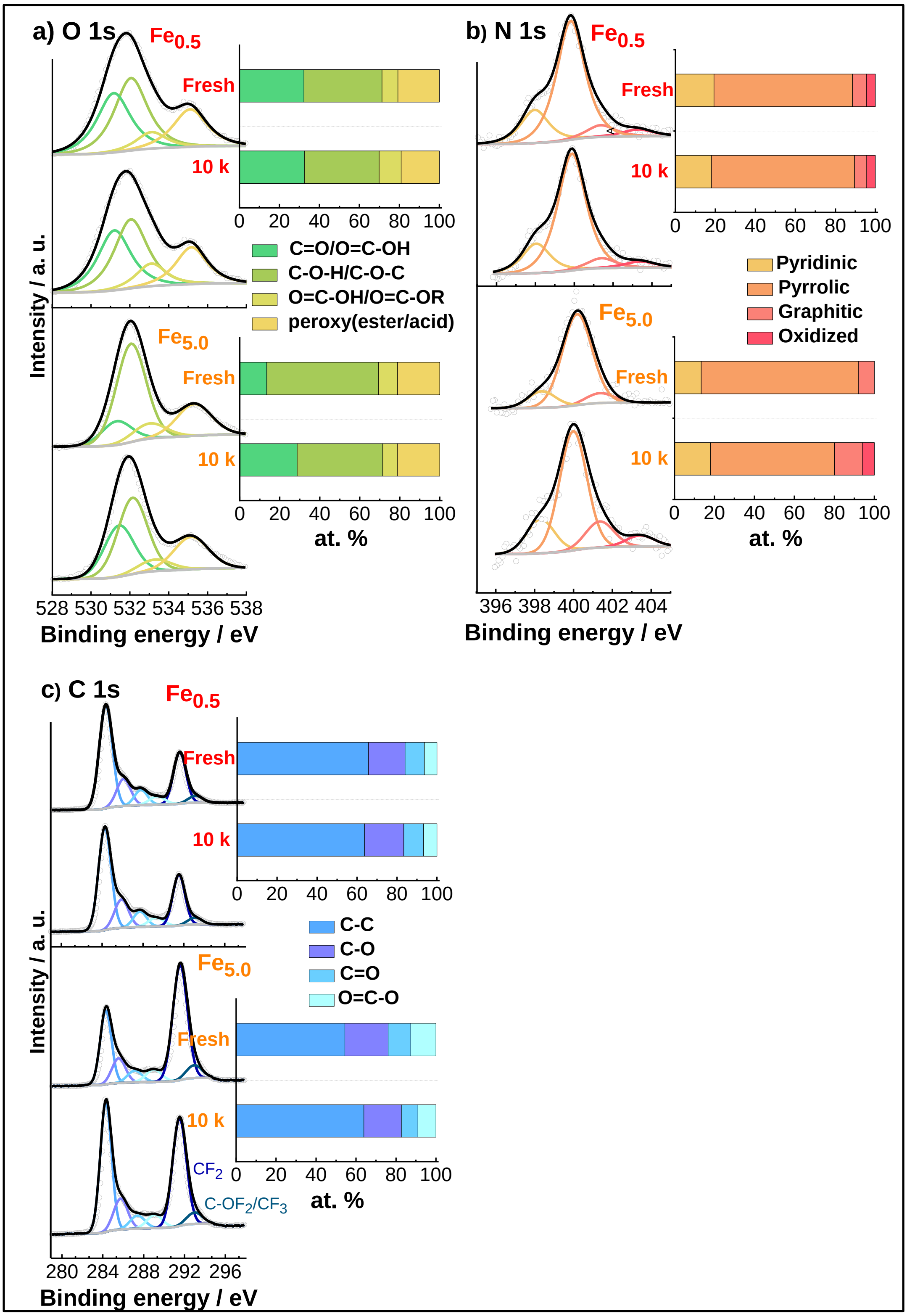

Figure 2.3. X-ray photoelectron spectroscopy deconvolution patterns of the **(a)** O 1s, **(b)** N 1s, **(c)** C 1s binding energy regions of the $Fe_{0.5}$ and $Fe_{5.0}$ catalysts before and after 10,000 AST cycles under Ar-purged 0.1 mol L^{-1} NaOH electrolyte at 60 °C.

The fittings of C 1s spectra (Figure 2.3c) were obtained considering six main deconvoluted peaks assigned to C-C (284.3 eV), C-O (285.6-286.0 eV), C=O (287.1-287.7 eV), O=C-O (289.0-289.3 eV) functional groups, besides Nafion related functional groups, as CF_2 (291.3 eV) and CF_3/C-OF_2 (293.0-293.1 eV), in agreement with the literature.[7,51] As evidenced by the bar chart, the C-C functional group is the most abundant for either Fe-catalysts before and even after 10,000 loading cycles. Further, the atomic percentage of C-C functional groups remains constant for $Fe_{0.5}$ (from 65.7 at.% to 63.8 at.%) and increase for $Fe_{5.0}$ (from 54.5 at.% to 63.9 at.%) after ASTs.

Raman spectra of the catalysts before and after 10,000 AST cycles are shown in Figure 2.4. These results can be compared in terms of the most intense spectral features related to the order/disorder of the sp^2 carbon bond, which is the D band at *ca.* 1350 cm^{-1} and the G band at *ca.* 1580 cm^{-1}. D band is associated with the presence of structural disorder of graphite lattice (A_{1g}-symmetry) and G band to the ideal graphitic lattice (E_{2g}-symmetry).[64] As shown in Figure 2.4, the Raman spectra of the catalysts are all almost identical before and after the 10,000 AST potential-cycles in either Ar or O_2-saturated electrolytes, which is in agreement with previous results for the oxidation of the carbon component at high pH solutions.[65] The 2D band (also labeled G', *ca.* 2650 cm^{-1}) in the inset of Figure 2.4 is linked to the two-phonon double resonance scattering that increases with the number of graphene layers.[66] In summary, comparisons of Raman results show that no obvious order/disorder differences are present in the catalysts, before and after the ASTs confirming the XPS spectra results.

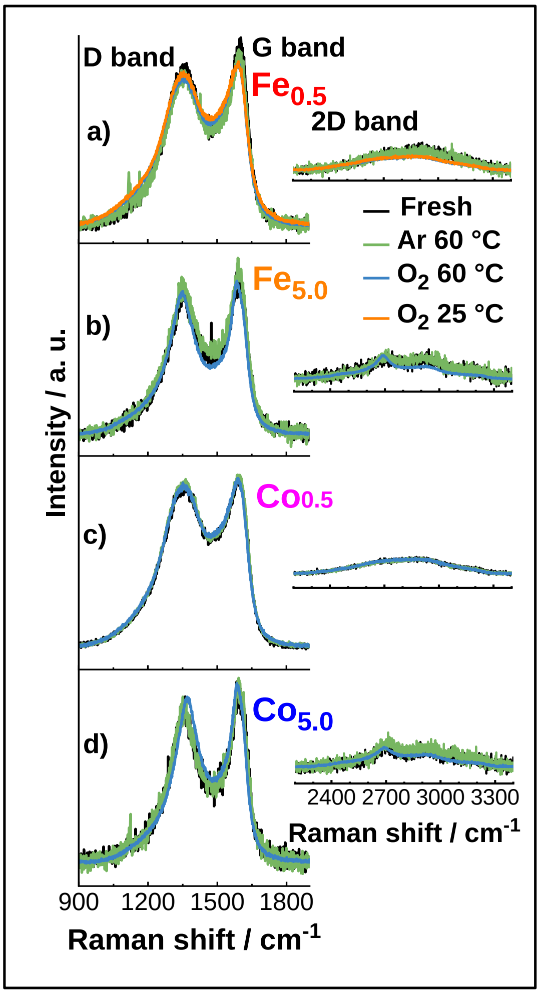

Figure 2.4. Raman spectra of the **(a)** $Fe_{0.5}$, **(b)** $Fe_{5.0}$, **(c)** $Co_{0.5}$ and **(d)** $Co_{5.0}$ catalysts before (black) and after 10,000 load-cycle under Ar-(green) and O_2-(blue) purged 0.1 mol L^{-1} NaOH at 60 °C (also at 25 °C and O_2 for $Fe_{0.5}$; orange). The spectra were normalized to the intensity of the G band (*ca*. 1580 cm^{-1}).

3.2 Electrocatalytic properties of Metal-N-C electrocatalysts

Figure 2.5 shows Ohmic-drop corrected cyclic voltammograms of the catalysts, obtained before and after 10,000 ASTs loading cycles conducted at 60 °C in Ar- and O_2-saturated alkaline electrolytes. CV results for all materials evidence appearance of capacitive features, which are linked to charge accumulation in the double layer of the catalyst electrodes. In particular, for the atomically metal dispersed catalysts ($Fe_{0.5}$ and $Co_{0.5}$), more pronounced capacitive currents are seen even after ASTs, with no further decrease seen even after 10,000 loading cycles. On the other hand, CV results for the metal-based nanoparticles ($M_{5.0}$) catalysts evidence smaller capacitive currents and also negligible effect of electrode cycling's, as expected due to the smaller specific surface area of the more graphitized carbon structures.[4,18] A small feature is observed for the $Co_{5.0}$ catalyst at potentials near the CV upper limit, where a drop of the anodic current is seen after load cycling. This anodic current is related with some oxidation and surface passivation of the Co nanoparticles, involving the initial formation of a $Co(OH)_2$ layer followed by the formation of Co_3O_4 and CoOOH,[46–48] as described above. Then, the partial conversion of Co nanoparticles to oxides species and the metal loss along with the ASTs lead to the depletion of the anodic current between fresh and aged Co5.0 catalyst. Finally, cyclic voltammograms obtained before and after AST in oxygen-saturated electrolytes at 60 °C and 25 °C evidence very similar features to those displayed in the argon-saturated electrolyte. It confirms that the nitrogen-doped carbon matrix does not suffer severe degradation, but mainly chemical changes over its catalytic surface up to 1.0 V *vs*. RHE, as confirmed above by XPS and Raman spectra.

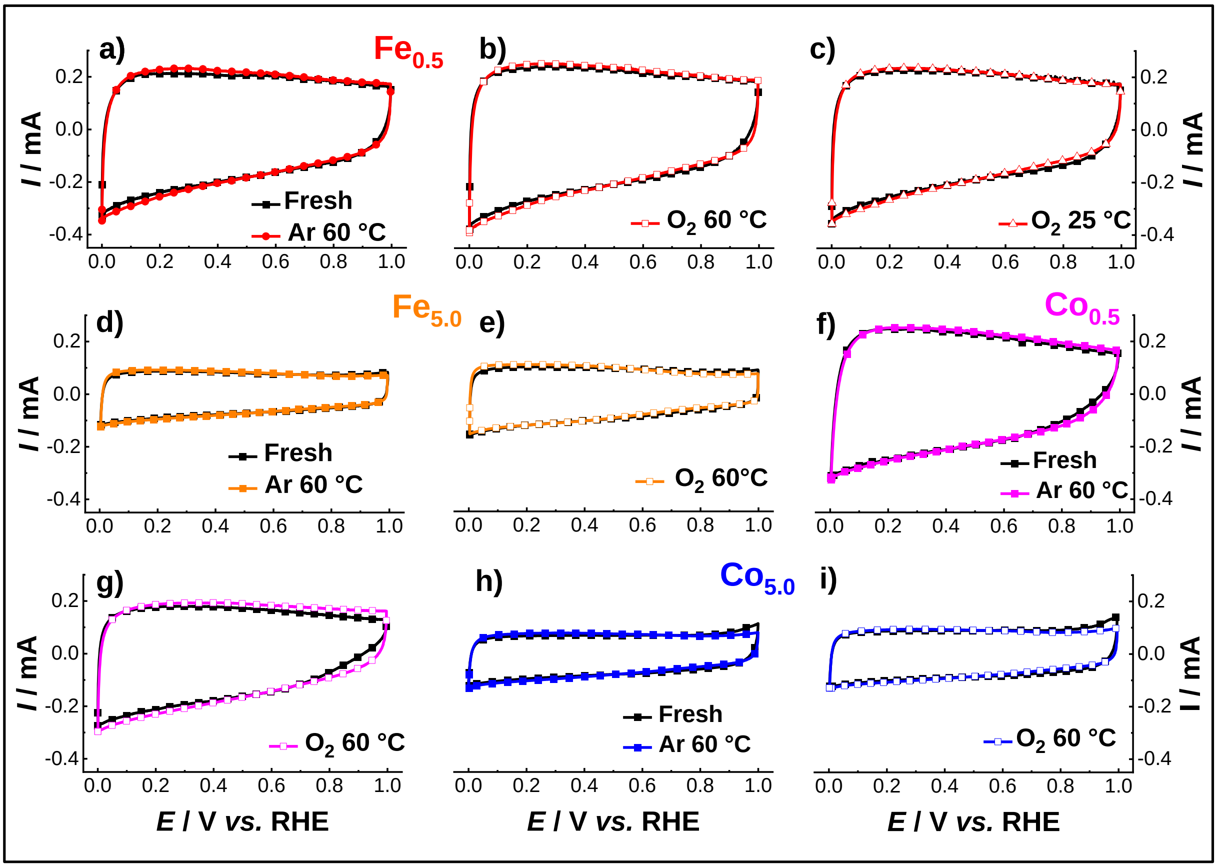

Figure 2.5. Cyclic voltammograms of $Fe_{0.5}$ (red), $Fe_{5.0}$ (orange), $Co_{0.5}$ (magenta) and $Co_{5.0}$ (blue) electrocatalysts before and after 10,000 AST loading cycles under **(a, d, f, h)** Ar-and O_2- **(b, e, g, i)** saturated 0.1 mol L^{-1} NaOH electrolyte at 60 °C (also **(c)** at O_2 and 25 °C for $Fe_{0.5}$). Representative CVs were performed in Ar-purged electrolytes, 10 mV s^{-1}, 0.8 mg_{powder} cm^{-2} and 25 °C.

ORR polarization curves for the fresh and aged catalysts obtained in O_2-saturated electrocatalysts are shown in Figure A2.2. These results show that the ORR onset potentials change depending on the nature of the catalysts,[18] but it remains constant for the fresh and aged electrodes, either in Ar and O_2 atmosphere and even after 10,000 cycles. ORR half-wave potential ($E_{half\text{-}wave}$) follow similar trends for the catalysts and the initial values are 0.82, 0.85, 0.80 and 0.84 V *vs.* RHE for $Fe_{0.5}$, $Fe_{5.0}$, $Co_{0.5}$ and $Co_{5.0}$, respectively, indicating higher activity for the materials with higher metal contents for each metallic center and it remains unaltered even after 10,000 cycles for most catalysts, as shown by Figure 2.6a (Table A2.2 for details). This behavior is in agreement with the literature for aged M-N-C catalysts in alkaline media regardless of the degradation conditions and/or electrochemical procedures.[14,16,31,67] Since the content and nature of functional groups change along with the AST cycles for most catalysts, these results would indicate that the real active centers are not exclusively related to the carbon functionalities, but also related to another component not affected by the electrode cycling. In contrast, the $E_{half\text{-}wave}$ slightly shift for $Co_{5.0}$ catalysts after AST under O_2 (0.81 V); the causes of this change might be related to changes in the reaction mechanism and/or rate-determining steps.

For analyzing this point, mass-corrected Tafel lines and their Tafel slopes (Figure A2.3 and Table A2.2) were obtained from the polarization results before and after AST in Ar and O_2 atmosphere. The Tafel slopes of fresh catalysts are in agreement with our previous work:[18] 79, 78, 58 and 51 mV dec^{-1} for $Fe_{0.5}$, $Fe_{5.0}$, $Co_{0.5}$ and $Co_{5.0}$, respectively. Results for the $Fe_{0.5}$ catalysts lead to Tafel lines with slopes of 93 and 107 mV dec^{-1}, along the cyclings at 60 °C under Ar and O_2, respectively, and 88 mV dec^{-1} when cyclings are made under O_2 at 25 °C. In the case of $Fe_{5.0}$, values of Tafel slopes are essentially the same as for $Fe_{0.5}$ (82 and 81 mV dec^{-1} under Ar and O_2 respectively), but here values resulted approximately constant along the AST cyclings, in contrast to $Fe_{0.5}$. For Co-catalysts, Tafel slope values were 66 and 73 mV dec^{-1} ($Co_{0.5}$) and 55 and mV dec^{-1} ($Co_{5.0}$), when cycled under argon and oxygen at 60 °C, respectively. Tafel slopes of the order of 80 mV dec^{-1} are expected for catalysts with moderate coverages of adsorbed intermediates (as for $Fe_{0.5}$ and $Fe_{5.0}$), while values near 60 mV dec^{-1} are often observed for catalysts with high degrees of oxygen-intermediates coverages (as seen here for $Co_{0.5}$ and $Co_{5.0}$).[68,69] In particular, for $M_{0.5}$ catalysts, there are clear tendencies of increase of Tafel slope and deviation of linearity of the lines after 10,000 loading cycles at 60 °C, and this may be assigned to changes in the number of electrons involved in the ORR and/or degree of coverages of adsorbed oxygen-based intermediates of ORR in the active sites, as discussed below. On the other hand, large separations of the Tafel lines are most probably resulting from a significant reduction in the number of active sites for the ORR occurring along the ASTs, and this maintains a reasonable correlation with the changes in the metal contents measured by X-EDS (Figure 2.2) and the particles sizes as measured by TEM (Figure 2.1 and A2.1).

In Figure A2.2, it is seen that most catalysts undergo slight degradation of the O_2 diffusion-limited current density (0.0 V < E < 0.6 V *vs*. RHE), along either Ar- or O_2-AST load cycling at 60 ºC. For $Fe_{0.5}$, the effect is less significant when the AST cycling is conducted at 25 °C in O_2-saturated electrolyte, indicating higher stability of the iron atomically dispersed catalyst at lower temperatures. This may be also related to the ability of iron to be re-deposited on the catalytic layer, which may be more efficient at 25 °C than 60 °C, evidencing that metal-losses slightly harm the complete reduction of O_2 to OH^-. Similar behavior for AST at 60 °C can be extended to $Co_{0.5}$, while these effects are negligible for the $Fe_{5.0}$ catalyst after AST 10,000 loading cycles in at 60 °C demonstrating great stability to the main reduction of O_2 to OH^-. It indicating that the residence time of reactants and/or intermediates in the thick layers act as an important factor to the complete reduction for aged catalysts, in agreement with results for fresh materials.[18,70] In contrast, the negative changes in the synergistic effect between cobalt and carbon nitrogen-doped shells should be considered in the HO_2^- stabilization for $Co_{5.0}$ catalyst, since the partial conversion of Co to oxides species evidencing the structural and/or chemical changes. Thus, the $Co_{5.0}$ indicates some deterioration of the catalyst's ability to retain ORR intermediate species, mainly HO_2^-, that leaves the catalyst thin-film without further reaction.

For a more detailed comparison of catalysts performance, ORR mass activities (i_{MA}) were obtained at 0.85 V *vs*. RHE for fresh and after ASTs under Ar- and O_2-purged electrolytes, which were then normalized by the values corresponding to fresh electrodes, and the results are shown in Figure 2.6b (see Table A2.2 for details). In general, these plots show that catalysts containing atomically dispersed metals ($M_{0.5}$) undergo less severe depletion of the mass activity along both ASTs conditions. For $Fe_{0.5}$, the initial mass activity shift from 2.576 A g_{powder}^{-1} to 2.200, 2.128 and 2.323 A g_{powder}^{-1} after ASTs under Ar and O_2 at 60 °C and 25 °C, respectively. The result is similar[35] or superior[15] to previous atomically dispersed iron catalyst after ASTs at 25 °C. For $Co_{0.5,}$ it starts from 0.686 A g_{powder}^{-1} to 0.472 (Ar) and 0.647 A g_{powder}^{-1} (O_2) after ASTs at 60 °C. Interestingly, despite proportionally more metal leaching for $M_{0.5}$ than their counterpart catalysts ($M_{5.0}$), as detected by X-EDS and ICP-MS, the mass activity depletion is less likely due to the almost intact chemical composition of its surface and/or near-surface, as shown by XPS. Thus, it may be attributed that their activity depletion is essentially related to the metal loss from the M-N_xC_y moieties, and this can be seen when comparing the metallic content after ASTs at 60 ° C and 25 ° C. It is possible for $Fe_{0.5}$ catalyst, iron leached from the Fe-N_xC_y moieties is completely re-deposited as Fe-based nanoparticles, which remains the catalyst with the same activity for the ORR of the initial atomically dispersed Fe-N_xC_y.

For $M_{5.0}$ catalysts, the surface changes related to nitrogen and carbon conversion and/or partial oxidation, as suggested by XPS, may explain these results together with metal loss, particularly for $Fe_{5.0}$ catalyst. For $Fe_{5.0}$, i_{MA} starts from 5.049 A g_{powder}^{-1} to 3.067 and 3.548 A g_{powder}^{-1} after ASTs under Ar and O_2 at 60 °C respectively; also from 2.580 A g_{powder}^{-1} to 1.194 (Ar at 60 °C) and 0.889 A g_{powder}^{-1}(O_2 at 60 °C) for $Co_{5.0}$. Regarding that different nitrogen functional groups have different activities towards ORR electrocatalysis, in which pyridinic and pyrrolic nitrogen have been attributed the most active while the graphitic and oxidized are fewer actives.[71,72] The interconversion of main pyrrolic sites to graphitic and oxidized nitrogen functional groups causes a drop in the ORR mass activities. Despite the metal loss from M@N-C active sites take place in less extension than M-N_xC_y counterparts, when coupled with chemical changes on the surface and/or near-surface can generate a largely negative influence in the synergistic effect between the nitrogen-doped carbon shell and the metallic center.

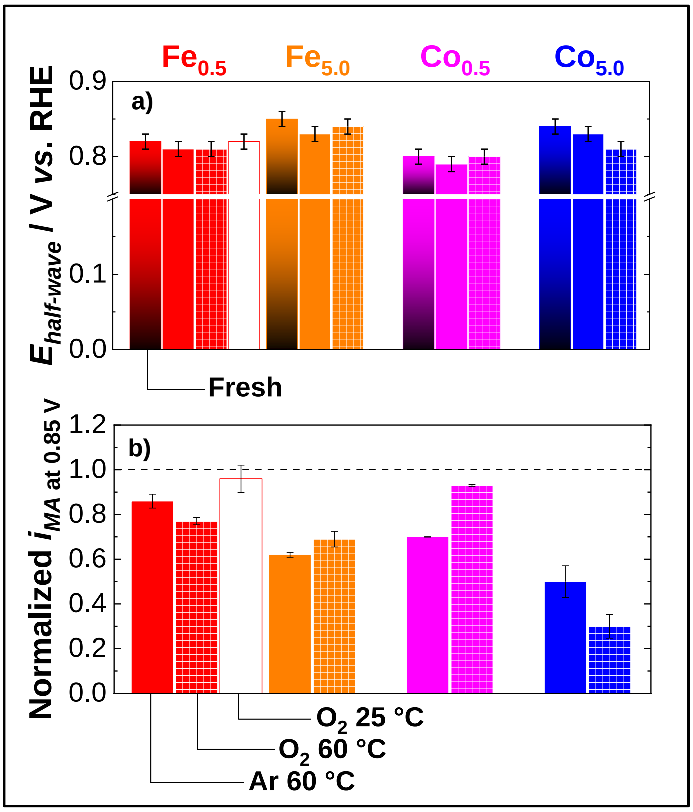

Figure 2.6. ORR kinetic parameter for Metal-N-C catalysts: **(a)** ORR half-wave potential and **(b)** normalized mass activity towards ORR (i_{MA}) measured at 0.85 V *vs.* RHE after 10,000 AST potential-cycles under Ar- and O_2-saturated 0.1 mol L^{-1} NaOH electrolyte at 60 °C (also at 25 °C and O_2 for $Fe_{0.5}$). For all measurements: 5 mV s^{-1}, 0.8 mg_{powder} cm^{-2}, 1600 rpm and 25 °C. The error bars represent the standard value deviation of at least three independent measurements.

2.4 Conclusions

In this work, we investigated the chemical changes of Fe-N-C and Co-N-C electrocatalysts during accelerated stress tests from 0.6 to 1.0 V *vs.* RHE under Ar- and O_2-saturated alkaline electrolytes at 60 °C and 25 °C. Interestingly, *in situ* Fe-based nanoparticles were grown with the temperature along AST under O_2 atmosphere at 60 °C and 25 °C, reaching the highest size at the lowest temperature, as detected by TEM and XRD. Further, the combined physicochemical and electrochemical findings indicate that the interconversion and/or partial oxidation of nitrogen- and oxygenated-surface-groups undergo more intensely for nanoparticles Fe-catalyst ($Fe_{5.0}$) than their counterpart atomically dispersed ($Fe_{0.5}$) on the surface and/or near-surface, as detected by XPS and confirmed by Raman spectroscopy and Cyclic Voltammetry. This effect combined with the demetallation of M@N-C moieties after AST loading cycles affects negatively the synergistic effect between the center metallic and the nitrogen-doped carbon shell. For atomically dispersed metal (M-N_xC_y), the depletion of ORR mass activity is governed by the metal loss to the electrolyte, as evidenced by X-EDS and ICP-MS measurements. Fe-N-C electrocatalysts are more stable than Co-based catalysts, indicating theirs as an excellent candidate for investigation on the anion-exchange membrane fuel cell and metal-air batteries.

2.5 References

1 X. Peng, V. Kashyap, B. Ng, S. Kurungot, L. Wang, J.R. Varcoe, W.E. Mustain, High-performing PGM-Free AEMFC cathodes from carbon-supported cobalt ferrite nanoparticles, **Catalysts**. 9 (2019) 1–12.

2 C.H. Choi, H.K. Lim, M.W. Chung, G. Chon, N. Ranjbar Sahraie, A. Altin, M.T. Sougrati, L. Stievano, H.S. Oh, E.S. Park, F. Luo, P. Strasser, G. Dražić, K.J.J. Mayrhofer, H. Kim, F. Jaouen, The Achilles' heel of iron-based catalysts during oxygen reduction in an acidic medium, **Energy Environ. Sci.** 11 (2018) 3176–3182.

3 J. Herranz, F. Jaouen, M. Lefèvre, U.I. Kramm, E. Proietti, J.P. Dodelet, P. Bogdanoff, S. Fiechter, I. Abs-Wurmbach, P. Bertrand, T.M. Arruda, S. Mukerjee, Unveiling N-protonation and anion-binding effects on Fe/N/C catalysts for O_2 reduction in proton-exchange-membrane fuel cells, **J. Phys. Chem. C.** 115 (2011) 16087–16097.

4 K. Kumar, P. Gairola, M. Lions, N. Ranjbar-Sahraie, M. Mermoux, L. Dubau, A. Zitolo, F. Jaouen, F. Maillard, Physical and Chemical Considerations for Improving Catalytic Activity and Stability of Non-Precious-Metal Oxygen Reduction Reaction Catalysts, **ACS Catal.** 8 (2018) 11264–11276.

5 K. Kumar, L. Dubau, M. Mermoux, J. Li, A. Zitolo, J. Nelayah, F. Jaouen, F. Maillard, On the Influence of Oxygen on the Degradation of Fe-N-C Catalysts, **Angew. Chemie** - Int. Ed. 59 (2020) 3235–3243.

6 A. Serov, I. V. Zenyuk, C.G. Arges, M. Chatenet, Hot topics in alkaline exchange membrane fuel cells, **J. Power Sources.** 375 (2018) 149–157.

7 L. Castanheira, L. Dubau, M. Mermoux, G. Berthomé, N. Caqué, E. Rossinot, M. Chatenet, F. Maillard, Carbon corrosion in proton-exchange membrane fuel cells: From model experiments to real-life operation in membrane electrode assemblies, **ACS Catal.** 4 (2014) 2258–2267.

8 L. Castanheira, W.O. Silva, F.H.B. Lima, A. Crisci, L. Dubau, F. Maillard, Carbon corrosion in proton-exchange membrane fuel cells: Effect of the carbon structure, the degradation protocol, and the gas atmosphere, **ACS Catal.** 5 (2015) 2184–2194.

9 N. Ramaswamy, S. Mukerjee, Fundamental Mechanistic Understanding of Electrocatalysis of Oxygen Reduction on Pt and Non-Pt Surfaces: Acid versus Alkaline Media, **Adv. Phys. Chem.** 2012 (2012).

10 B.P. Setzler, Z. Zhuang, J.A. Wittkopf, Y. Yan, Activity targets for nanostructured platinum-group-metal-free catalysts in hydroxide exchange membrane fuel cells, **Nat. Nanotechnol.** 11 (2016) 1020–1025.

11 J.R. Varcoe, P. Atanassov, D.R. Dekel, A.M. Herring, M.A. Hickner, P.A. Kohl, A.R. Kucernak, W.E. Mustain, K. Nijmeijer, K. Scott, T. Xu, L. Zhuang, Anion-exchange membranes in electrochemical energy systems, **Energy Environ. Sci.** 7 (2014) 3135–3191.

12 R. Sgarbi, E.A. Ticianelli, F. Maillard, F. Jaouen, M. Chatenet, Oxygen Reduction Reaction on Metal and Nitrogen – Doped Carbon Electrocatalysts in the Presence of

Sodium Borohydride, **Electrocatalysis**. 11 (2020) 365–373.

13 D.R. Dekel, Review of cell performance in anion exchange membrane fuel cells, **J. Power Sources.** 375 (2018) 158–169.

14 D. Chen, J. Ji, Z. Jiang, M. Ling, Z. Jiang, X. Peng, Molecular-confinement synthesis of sub-nano Fe/N/C catalysts with high oxygen reduction reaction activity and excellent durability for rechargeable Zn-Air batteries, **J. Power Sources.** 450 (2020) 227660.

15 Y. Gao, Z. Cai, X. Wu, Z. Lv, P. Wu, C. Cai, Graphdiyne-Supported Single-Atom-Sized Fe Catalysts for the Oxygen Reduction Reaction: DFT Predictions and Experimental Validations, **ACS Catal.** 8 (2018) 10364–10374.

16 Y. Chen, Z. Li, Y. Zhu, D. Sun, X. Liu, L. Xu, Y. Tang, Atomic Fe Dispersed on N-Doped Carbon Hollow Nanospheres for High-Efficiency Electrocatalytic Oxygen Reduction, **Adv. Mater.** 31 (2019) 1806312.

17 X. Zhang, Y. Bahari, D. Lyu, L. Liang, F. Yu, M. Qing, Molecular-level design of Fe-N-C catalysts derived from Fe-dual pyridine coordination complexes for highly efficient oxygen reduction, **J. Catal.** 372 (2019) 245–257.

18 R. Sgarbi, K. Kumar, F. Jaouen, A. Zitolo, E.A. Ticianelli, F. Maillard, Oxygen reduction reaction mechanism and kinetics on M-N_xC_y and M@N-C active sites present in model M-N-C catalysts under alkaline and acidic conditions, **J. Solid State Electrochem**. (2019). DOI: 10.1007/s10008-019-04436-w.

19 L. Osmieri, A.H.A. Monteverde Videla, P. Ocón, S. Specchia, Kinetics of Oxygen Electroreduction on Me-N-C (Me = Fe, Co, Cu) Catalysts in Acidic Medium: Insights on the Effect of the Transition Metal, **J. Phys. Chem. C**. 121 (2017) 17796–17817.

20 G. Chen, P. Liu, Z. Liao, F. Sun, Y. He, H. Zhong, T. Zhang, E. Zschech, M. Chen, G. Wu, J. Zhang, X. Feng, Zinc-Mediated Template Synthesis of Fe-N-C Electrocatalysts with Densely Accessible Fe-N_x Active Sites for Efficient Oxygen Reduction, **Adv. Mater.** 32 (2020) 1907399.

21 A. Ohma, K. Shinohara, A. Iiyama, T. Yoshida, A. Daimaru, Membrane and Catalyst Performance Targets for Automotive Fuel Cells by FCCJ Membrane, Catalyst, MEA WG, **ECS Trans.** 41 (2011) 775–784.

22 J. Liu, B. V. Cunning, T. Daio, A. Mufundirwa, K. Sasaki, S.M. Lyth, Nitrogen-Doped Carbon Foam as a Highly Durable Metal-Free Electrocatalyst for the Oxygen Reduction Reaction in Alkaline Solution, **Electrochim. Acta.** 220 (2016) 554–561.

23 J. Sanetuntikul, S. Shanmugam, High pressure pyrolyzed non-precious metal oxygen reduction catalysts for alkaline polymer electrolyte membrane fuel cells, **Nanoscale.** 7 (2015) 7644–7650.

24 C. Lafforgue, M. Chatenet, L. Dubau, D.R. Dekel, Accelerated Stress Test of Pt/C Nanoparticles in an Interface with an Anion-Exchange Membrane - An Identical-Location Transmission Electron Microscopy Study, **ACS Catal.** 8 (2018) 1278–1286.

25 A. Zadick, L. Dubau, N. Sergent, G. Berthomé, M. Chatenet, Huge Instability of Pt/C Catalysts in Alkaline Medium, **ACS Catal.** 5 (2015) 4819–4824.

26 G.A. Ferrero, K. Preuss, A. Marinovic, A.B. Jorge, N. Mansor, D.J.L. Brett, A.B. Fuertes, M. Sevilla, M.M. Titirici, Fe-N-Doped Carbon Capsules with Outstanding Electrochemical Performance and Stability for the Oxygen Reduction Reaction in Both Acid and Alkaline Conditions, **ACS Nano.** 10 (2016) 5922–5932.

27 S.G. Peera, J. Balamurugan, N.H. Kim, J.H. Lee, Sustainable Synthesis of Co@NC Core Shell Nanostructures from Metal Organic Frameworks via Mechanochemical Coordination Self-Assembly: An Efficient Electrocatalyst for Oxygen Reduction Reaction, **Small.** 14 (2018) 1800441.

28 H. Tan, Y. Li, J. Kim, T. Takei, Z. Wang, X. Xu, J. Wang, Y. Bando, Y.M. Kang, J. Tang, Y. Yamauchi, Sub-50 nm Iron–Nitrogen-Doped Hollow Carbon Sphere-Encapsulated Iron Carbide Nanoparticles as Efficient Oxygen Reduction Catalysts, Adv. Sci. 5 (2018). https://doi.org/10.1002/advs.201800120.

29 M. Thomas, R. Illathvalappil, S. Kurungot, B.N. Nair, A.P. Mohamed, G.M. Anilkumar, T. Yamaguchi, U.S. Hareesh, Morphological Ensembles of N-Doped Porous Carbon Derived from ZIF-8/Fe-Graphene Nanocomposites: Processing and Electrocatalytic Studies, **ChemistrySelect.** 3 (2018) 8688–8697.

30 Z. Yan, C. Dai, M. Zhang, X. Lv, X. Zhao, J. Xie, Nitrogen doped porous carbon with iron promotion for oxygen reduction reaction in alkaline and acidic media, **Int. J. Hydrogen Energy**. 44 (2019) 4090–4101.

31 J.W. Huang, Y. Bin Chen, X.L. Chen, X. Liu, L.S. Ma, W.Y. Su, Y. Zhao, H. Bin Zhu, H. Yang, Exploring Efficient Fe/N/C Electrocatalysts for Oxygen Reduction from Nonporous Interpenetrated Metal-Organic Framework Involving in Situ Formation of ZnO Templates, **ACS Sustain. Chem. Eng**. 8 (2020) 3208–3217.

32 J. Zhu, M. Xiao, C. Liu, J. Ge, J. St-Pierre, W. Xing, Growth mechanism and active site probing of Fe_3C@N-doped carbon nanotubes/C catalysts: guidance for building highly efficient oxygen reduction electrocatalysts, **J. Mater. Chem. A**. 3 (2015) 21451–21459.

33 A. Mufundirwa, G.F. Harrington, B. Smid, B. V. Cunning, K. Sasaki, S.M. Lyth, Durability of template-free Fe-N-C foams for electrochemical oxygen reduction in alkaline solution, **J. Power Sources**. 375 (2018) 244–254.

34 P.G. Santori, F.D. Speck, J. Li, A. Zitolo, Q. Jia, S. Mukerjee, S. Cherevko, F. Jaouen, Effect of Pyrolysis Atmosphere and Electrolyte pH on the Oxygen Reduction Activity, Stability and Spectroscopic Signature of FeN_x Moieties in Fe-N-C Catalysts, **J. Electrochem. Soc.** 166 (2019) F3311–F3320.

35 C. Domínguez, F.J. Pérez-Alonso, M.A. Salam, S.A. Al-Thabaiti, M.A. Peña, F.J. García-García, L. Barrio, S. Rojas, Repercussion of the carbon matrix for the activity and stability of Fe/N/C electrocatalysts for the oxygen reduction reaction, **Appl. Catal. B Environ.** 183 (2016) 185–196.

36 S.H. Lee, J. Kim, D.Y. Chung, J.M. Yoo, H.S. Lee, M.J. Kim, B.S. Mun, S.G. Kwon, Y.E. Sung, T. Hyeon, Design Principle of Fe-N-C Electrocatalysts: How to Optimize Multimodal Porous Structures?, **J. Am. Chem. Soc.** 141 (2019) 2035–2045.

37 R. Gokhale, Y. Chen, A. Serov, K. Artyushkova, P. Atanassov, Novel dual templating approach for preparation of highly active Fe-N-C electrocatalyst for oxygen reduction,

Electrochim. Acta. 224 (2017) 49–55.

38 A. Zitolo, N. Ranjbar-Sahraie, T. Mineva, J. Li, Q. Jia, S. Stamatin, G.F. Harrington, S.M. Lyth, P. Krtil, S. Mukerjee, E. Fonda, F. Jaouen, Identification of catalytic sites in cobalt-nitrogen-carbon materials for the oxygen reduction reaction, **Nat. Commun.** 8, 957 (2017).

39 C.D. Wagner, W.M. Riggs, L.E. Davis, J.F. Moulder, G.E. Muilenberg, **Handbook of X-ray electron spectroscopy**, Minnesota, 1979.

40 A. Zitolo, V. Goellner, V. Armel, M.T. Sougrati, T. Mineva, L. Stievano, E. Fonda, F. Jaouen, Identification of catalytic sites for oxygen reduction in iron- and nitrogen-doped graphene materials, **Nat. Mater.** 14 (2015) 937–942.

41 V. Armel, J. Hannauer, F. Jaouen, Effect of ZIF-8 crystal size on the O_2 electro-reduction performance of pyrolyzed Fe–N–C catalysts, **Catalysts**. 5 (2015) 1333–1351.

42 Y. Pan, S. Liu, K. Sun, X. Chen, B. Wang, K. Wu, X. Cao, W.C. Cheong, R. Shen, A. Han, Z. Chen, L. Zheng, J. Luo, Y. Lin, Y. Liu, D. Wang, Q. Peng, Q. Zhang, C. Chen, Y. Li, A Bimetallic Zn/Fe Polyphthalocyanine-Derived Single-Atom Fe-N_4 Catalytic Site:A Superior Trifunctional Catalyst for Overall Water Splitting and Zn–Air Batteries, **Angew. Chemie - Int. Ed**. 57 (2018) 8614–8618.

43 M. Pourbaix, **Atlas of Electrochemical Equilibria in Aqueous Solutions**, National Association of Corrosion Engineers, Houston, 1974.

44 W.M. Haynes, D.R. Lide, T.J. Bruno, eds., **Handbook of Chemistry and Physics: A Ready-Reference Book of Chemical and Physical Data**, 97th ed., CRC Press, Boca Raton, 2017.

45 A.A. Koverga, A.M. Gómez-Marin, L. Dorkis, E. Flórez, E.A. Ticianelli, Role of Transition Metals on TM/Mo_2C Composites : Hydrogen Evolution Activity in Mildly Acidic and Alkaline Media, **ACS Appl. Mater. Interfaces.** 12 (2020) 27150-27165.

46 M.E.G. Lyons, M.P. Brandon, The oxygen evolution reaction on passive oxide covered transition metal electrodes in alkaline solution - Part II - cobalt, **Int. J. Electrochem. Sci.** 3 (2008) 1425–1462.

47 R.D. Cowling, A.C. Riddiford, The anodic behaviour of cobalt in alkaline solutions, **Electrochim. Acta.** 14 (1969) 981–989.

48 M. Favaro, J. Yang, S. Nappini, E. Magnano, F.M. Toma, E.J. Crumlin, J. Yano, I.D. Sharp, Understanding the Oxygen Evolution Reaction Mechanism on CoO_x using Operando Ambient-Pressure X-ray Photoelectron Spectroscopy, **J. Am. Chem. Soc.** 139 (2017) 8960–8970.

49 R. Rozada, J.I. Paredes, S. Villar-Rodil, A. Martínez-Alonso, J.M.D. Tascón, Towards full repair of defects in reduced graphene oxide films by two-step graphitization, **Nano Res.** 6 (2013) 216–233.

50 D. Rosenthal, M. Ruta, R. Schlögl, L. Kiwi-Minsker, Combined XPS and TPD study of oxygen-functionalized carbon nanofibers grown on sintered metal fibers, **Carbon N. Y**. 48 (2010) 1835–1843.

51 M. Smith, L. Scudiero, J. Espinal, J.S. McEwen, M. Garcia-Perez, Improving the deconvolution and interpretation of XPS spectra from chars by ab initio calculations, **Carbon N. Y.** 110 (2016) 155–171.

52 J.F. Gomes, A.C. Garcia, L.H.S. Gasparotto, N.E. De Souza, E.B. Ferreira, C. Pires, G. Tremiliosi-Filho, Influence of silver on the glycerol electro-oxidation over AuAg/C catalysts in alkaline medium: A cyclic voltammetry and in situ FTIR spectroscopy study, **Electrochim. Acta.** 144 (2014) 361–368.

53 R.M.L.M. Sandrini, J.R. Sempionatto, E. Herrero, J.M. Feliu, J. Souza-Garcia, C.A. Angelucci, Mechanistic aspects of glycerol electrooxidation on Pt(111) electrode in alkaline media, **Electrochem. Commun.** 86 (2018) 149–152.

54 K. Stańczyk, R. Dziembaj, Z. Piwowarska, S. Witkowski, Transformation of nitrogen structures in carbonization of model compounds determined by XPS, **Carbon N. Y**. 33 (1995) 1383–1392.

55 C. Zhang, S. Yang, J. Wu, M. Liu, S. Yazdi, M. Ren, J. Sha, J. Zhong, K. Nie, A.S. Jalilov, Z. Li, H. Li, B.I. Yakobson, Q. Wu, E. Ringe, H. Xu, P.M. Ajayan, J.M. Tour, Electrochemical CO_2 Reduction with Atomic Iron-Dispersed on Nitrogen-Doped Graphene, **Adv. Energy Mater.** 8 (2018).

56 V. Goellner, V. Armel, A. Zitolo, E. Fonda, F. Jaouen, Degradation by Hydrogen Peroxide of Metal-Nitrogen-Carbon Catalysts for Oxygen Reduction, **J. Electrochem. Soc.** 162 (2015) H403–H414.

57 Z.-Y. Zhou, C. Chen, S.-G. Sun, W.-H. Yang, M.-Q. Wang, H.-H. Wang, Pyrolyzed Fe–N–C Composite as an Efficient Non-precious Metal Catalyst for Oxygen Reduction Reaction in Acidic Medium, **ACS Catal.** 4 (2014) 3928–3936.

58 V. Perazzolo, E. Grądzka, C. Durante, R. Pilot, N. Vicentini, G.A. Rizzi, G. Granozzi, A. Gennaro, Chemical and Electrochemical Stability of Nitrogen and Sulphur Doped Mesoporous Carbons, **Electrochim. Acta.** 197 (2016) 251–262.

59 A.F. Diaz, A. Martinez, K.K. Kanazawa, M. Salmón, Electrochemistry of some substituted pyrroles, **J. Electroanal. Chem.** 130 (1981) 181–187.

60 H.D. Tabba, K.M. Smith, Anodic Oxidation Potentials of Substituted Pyrroles: Derivation and Analysis of Substituent Partial Potentials, **J. Org. Chem.** 49 (1984) 1870–1875.

61 J.K. Howard, K.J. Rihak, A.C. Bissember, J.A. Smith, The Oxidation of Pyrrole, **Chem. - An Asian J.** 11 (2016) 155–167.

62 N.L. Weinberg, E.A. Brown, The Anodic Oxidation of Organic Compounds. I. The Electrochemical Methoxylation of 2,6-Dimethoxypyridine and N-Methylpyrrole, **J. Org. Chem.** 31 (1966) 4054–4058.

63 X. Zhou, S. Liu, H. Yu, A. Xu, J. Li, X. Sun, J. Shen, W. Han, L. Wang, Electrochemical oxidation of pyrrole, pyrazole and tetrazole using a TiO_2 nanotubes based SnO_2-Sb/3D highly ordered macro-porous PbO_2 electrode, **J. Electroanal. Chem.** 826 (2018) 181–190.

64 A. Sadezky, H. Muckenhuber, H. Grothe, R. Niessner, U. Pöschl, Raman microspectroscopy of soot and related carbonaceous materials: Spectral analysis and structural information, **Carbon** N. Y. 43 (2005) 1731–1742.

65 Y. Yi, G. Weinberg, M. Prenzel, M. Greiner, S. Heumann, S. Becker, R. Schlögl, Electrochemical corrosion of a glassy carbon electrode**, Catal. Today**. 295 (2017) 32–40.

66 J.S. Park, A. Reina, R. Saito, J. Kong, G. Dresselhaus, M.S. Dresselhaus, G′ band Raman spectra of single, double and triple layer graphene, Carbon N. Y. 47 (2009) 1303–1310. https://doi.org/10.1016/j.carbon.2009.01.009.

67 X. Chen, S. Wang, Y. Wang, Z. Yang, S. Liu, J. Gao, Z. Su, P. Zhu, X. Zhao, G. Wang, Nitrogen-Doped Mesoporous Carbon Layer with Embedded Co/CoO$_x$ Nanoparticles Coated on CNTs for Oxygen Reduction Reaction in Zn–Air Battery, **Electrocatalysis**. 10 (2019) 277–286.

68 J. Perez, E.R. Gonzalez, E.A. Ticianelli, Oxygen electrocatalysis on thin porous coating rotating platinum electrodes, **Electrochim. Acta**. 44 (1998) 1329–1339.

69 M. V. Castegnaro, W.J. Paschoalino, M.R. Fernandes, B. Balke, M.C. M Alves, E.A. Ticianelli, J. Morais, Pd-M/C (M = Pd, Cu, Pt) Electrocatalysts for Oxygen Reduction Reaction in Alkaline Medium: Correlating the Electronic Structure with Activity, **Langmuir**. 33 (2017) 2734–2743.

70 K.S. Freitas, B.M. Concha, E.A. Ticianelli, M. Chatenet, Mass transport effects in the borohydride oxidation reaction - Influence of the residence time on the reaction onset and faradaic efficiency, **Catal. Today**. 170 (2011) 110–119.

71 J. Liu, P. Song, M. Ruan, W. Xu, Catalytic properties of graphitic and pyridinic nitrogen doped on carbon black for oxygen reduction reaction, **Chinese J. Catal**. 37 (2016) 1119–1126.

72 J. Liu, P. Song, W. Xu, Structure-activity relationship of doped-nitrogen (N)-based metal-free active sites on carbon for oxygen reduction reaction, **Carbon** N. Y. 115 (2017) 763–772.

Chapter 3

Oxygen Reduction Reaction on Metal and Nitrogen-Doped Carbon Electrocatalysts in the Presence of Sodium Borohydride

This chapter has been adapted with permission from Springer Nature (Electrocatalysis, 2020, DOI: 10.1007/s12678-020-00602-1)

3.1 Introduction

Small mobile electric devices (*e.g.*, either portable electronics or drones) require power systems of high energy density. They are usually powered by batteries, but these “closed systems” are inherently limited by their insufficient specific energy (*e.g.*, < 250 Wh kg^{-1} for the most energetic Li-ion systems [1]). Fuel cells, being open systems, are intrinsically denser in energy and could therefore advantageously be used in such devices. The present standard is the proton exchange membrane fuel cell (PEMFC), which is, in its state-of-the-art, fed by pure hydrogen [2]. While transporting, compressing, and storing gaseous hydrogen may prove relevant for large quantities of energy stored, this solution is not always efficient, safe, economically viable, and therefore relevant in applications where smaller amount of energy is stored, *i.e.*, the particular case for small mobile electric devices. In that situation, the direct oxidation of a liquid fuel may be more desirable, and direct methanol fuel cells (DMFC) have historically been studied as the pioneer direct liquid fuel cell (DLFC) [3]. However, electrooxidizing methanol is a complex and slow process (not speaking from the toxicity of the fuel), which requires extensive amounts of platinum-group metals (PGM) electrocatalyst, and this is a clear hindrance to the development of DMFCs, should they be acidic or alkaline [2, 4]. While other hydrocarbon fuels have been tried as well, none proved capable to provide both sufficient energy and power density (even in alkaline environments, known to facilitate the reactions and hence to render them faster [5]), a clear drawback for the powering of small electronic devices. This triggered intense research to find more suitable liquid fuels for portable/small mobility application; from these works, sodium borohydride soon appeared as a promising candidate, owing to the properties of its fuel [6, 7] and of its relevance for portable fuel cell system design [8–11].

Of course, the direct oxidation of the borohydride anion (BH_4^-) in a direct borohydride fuel cell (DBFC) is not an easy process, and many works addressed the issue, so as to isolate the reaction mechanisms [12–18]; the proper electrocatalysts for the anode [19]; and the ideal fuel composition, electrode structure, operating parameters of the anode, etc. [20–23]. While one shall not neglect research actions to improve our understanding of the borohydride oxidation reaction (BOR) and hence to find better materials to achieve it efficiently, one must also not neglect the membrane/separator that should separate the anode and cathode compartments. To date, cation-exchange membranes are more mature than their anion-exchange counterparts, and bipolar membranes are at an early stage of development. All types of ion-exchange membranes can be used in a DBFC (see for example [24, 25]), and, whatever the nature of the membrane/separator, there are drawbacks to their utilization. For a cation-exchange membrane, during DBFC operation, the Na^+ cation shall migrate to the cathode, where it will combine with the OH^- species formed in the alkaline oxygen reduction reaction (ORR), thereby displacing the NaOH from the anolyte to the cathode side. This naturally has a clear detrimental effect on the operation of the cathode, as recently put forth by Ould-Amara *et al*. [26], owing to deleterious crystallization of NaOH in the cathode pores, leading to unavoidable mass-transport hindrances. Should an anion-exchange membrane be used (this is probably the desired situation, as the anolyte of a DBFC is necessarily alkaline [27, 28]), there will be non-negligible crossover of borohydride anions from the fuel anolyte to the cathode compartment. In that latter case, of course, the cathode catalyst must be tolerant to BH_4^-, otherwise its apparent ORR activity will be significantly affected, because either the net current will be the sum of the cathodic (desired) ORR and anodic (undesired) BOR contributions, or because borohydride species will adversely adsorb or react with the catalyst material and deactivate or chemically modify it. This shows that the cathode of a DBFC should also be tightly optimized, and in particular that BH_4^--tolerant ORR catalysts must be selected for the application [10].

The literature regarding fuel-tolerant electrocatalysts for alkaline fuel cells is abundant, but mainly deals with tolerance to hydrocarbon molecules (methanol, ethanol, etc.) [29–33]. The case of borohydride, a very strong reducer, has been less under focus, even if some (rare) studies have explored the issue. Metal-oxides (*e.g.*, perovskites, $LaNi_{0.8}Co_{0.2}O_3$ [34] and carbon-supported nanometric manganese oxides, MnO_x/ C) [35, 36] have demonstrated some interesting properties for potential use in DBFC cathodes, but one could question the durability of such inherently oxidized materials in strongly reducing environments; as a matter of fact, long-term stability data was never reported in such studies, except for MnO_x/C (but not in the presence of BH_4^- species) [37]. Cheng and Scott [38] explored PGM-free electrocatalysts (iron tetramethoxyphenyl porphyrin (FeTMPP), silver, and nickel), regarding their ORR performances in direct borohydride fuel cell cathodes. FeTMPP cathodes outperformed silver and nickel ones, which led the authors to the conclusion that FeTMPP was somewhat $BH4^-$-tolerant, unlike Ag and Ni (the latter is no surprise, as both Ag [39, 40] and especially Ni [41–43] are active catalysts for the BOR). More recently Fe-aminoantipyrine (Fe-AAPyr) was successfully developed as a BH_4^--tolerant ORR catalyst for a mixed-reactant DBFC[44]. These last two materials fall into the category of metal–nitrogen–carbon (M–N–C) catalysts, which are now under tremendous focus to replace Pt-based ones for PEMFC applications (see, *e.g.*, [45–47]). Because these classes of material are commonly admitted to be tolerant to fuel species, and some of them have indeed shown tolerance to borohydride [38, 44], the present contribution explores two families of M–N–C compounds, based on cobalt (Co) and iron (Fe) metal centers. It notably aims to unveil whether any such catalysts are tolerant to BH_4^-, or if they must have particular features to be tolerant, herein are compared the nature of the metal (Fe and Co), the structure of the resulting electrocatalyst (atomically dispersed *vs*. nanoparticles), and its mode of synthesis (flash *vs*. ramp pyrolysis in argon atmosphere).

3.2 Materials and Methods

3.2.1 Catalyst Syntheses

The electrocatalysts used in this study were synthesized using the method described by Ranjbar-Sahraie *et al*. [48]. In brief, a zinc (II) zeolitic imidazolate framework (ZIF-8, purchased from BASF, Basolite Z1200), Fe or Co acetate precursor, and 1,10-phenanthroline were mixed via dry planetary ball milling. The masses of the precursors were 200 mg phenanthroline, 800 mg ZIF-8, and either 0.5 wt% or 5.0 wt% of metal (Fe or Co) compared with the overall mass of the three precursors. The dry mixed metal, carbon, and nitrogen precursors were then pyrolyzed either in flash (*i.e*., the powder was introduced at 1050 °C in the oven) or ramp (the powder was heated from room temperature to 1050 °C at 5°C min^{-1}) mode, and a temperature of 1050 °C was maintained for 1 h. Then, the quartz tube and boat were opened and quenched to room temperature while still flowing Ar. As Ar was used, the weight loss during the pyrolysis was *ca*. 65 – 75 wt.% and it was independent on the pyrolysis mode.

3.2.2 Physicochemical Characterizations

All physicochemical characterizations have been previously published; then, here only a brief overview is presented (for detailed experimental specifications, the readers could refer to References [48–52]). TEM measurements were performed on a JEM-2100HCKM (JEOL) microscope operating at 120 keV for the atomically dispersed metal atom electrocatalysts [48, 50] and a JEOL 2010 TEM microscope operating at 200 kV for the metal nanoparticulated electrocatalysts [51]. To obtain ^{57}Fe Mössbauer spectra and confirm the absence of zerovalent iron crystalline phases in atomically-dispersed metal atom electrocatalysts, Fe-containing samples were measured with ^{57}Co–Rh source and analyzed for doublet and sextet spectral components ([51]for $Fe_{5.0}$0RP and $Fe_{0.5}$RP; [52]for $Fe_{0.5}$FP). The carbon nanocrystallites were characterized by Raman Spectroscopy using an argon LASER (514 nm) and X-ray diffraction by an X'Pert PRO MPD PANalytical diffractometer operated at 45 kV [51]. Surface area and pore volume were estimated by the Brunauer–Emmett–Teller (BET) method using a Micromeritics ASAP 2020 equipment with N_2 sorption at liquid nitrogen temperature (77 K) [49].

3.2.3 Electrochemical Characterizations

Before the electrochemical measurements, the glassware, polytetrafluoroethylene (PTFE)-based materials, volumetric flasks, tips, and electrodes were cleaned in 50% v/v solution of H_2SO_4 (Merck, Suprapur 96 wt.%)/H_2O_2 (Carl Roth, 30% v/v) and rinsed in ultrapure water (MQ grade, 18.2 MΩ cm, 1– 3 ppb TOC) and hot ultrapure water. The glassy carbon tips (working electrode substrates) were polished on diamond polishing paste (Presi®, 3 and 1 μm). All fresh Ar- and O_2-saturated electrolytes were prepared from NaOH (Alfa Aesar, 50% w/w aqueous solution) and ultrapure water to obtain a concentration of 0.1 M; similarly, $NaBH_4$ fresh "mother solution" was prepared from previous 0.1 M NaOH solution and $NaBH_4$ powder (Merck, ≥ 98.0%) to obtain a concentration total of 0.5 M.

All electrochemical measurements were performed using a three-electrode PTFE-electrochemical cell with temperature control at 25 °C. The reference electrode was a commercial reversible hydrogen electrode (RHE, Gaskatel GmbH) connected to the cell by a Luggin capillary and the counter electrode was a carbon sheet. The working electrode, a homemade glassy carbon cylinder (glassy carbon Sigradur® from Hochtemperatur-Werkstoffe GmbH) inserted in a PTFE cylinder, was connected to a commercial rotator (Origalys®). To investigate the electrocatalyst materials, a catalytic layer was made onto the glassy carbon disc substrate (0.196 cm^2) by dropping 20 μL of each prepared ink to obtain a total catalyst loading of 0.8 mg_{powder} cm^{-2}. The catalyst inks were prepared by dispersing 10 mg of catalytic powder, 50 μL of 5 wt.% Nafion solution (Sigma-Aldrich), 854 μL of isopropanol (Carl Roth), and 372 μL of ultrapure water, followed by ultrasonic homogenization [51]. Then, the electrochemical cell was coupled to an Autolab PGSTAT12 potentiostat to perform RDE (rotating disk electrode) measurements.

An initial reproducible surface state was obtained by applying 50 cyclic voltammograms (CVs) between 0.0 and 1.0 V *vs*. RHE at 100 mV s^{-1} in Ar-purged 0.1 M NaOH. Next, the CVs of the catalytic layers were recorded in the same conditions at 10 and 5 mV s^{-1}, followed by polarization curves at 5 mV s^{-1} in Ar- and O_2-saturated 0.1 M NaOH electrolyte at 400 rpm. Capacitive currents obtained (CVs at 5 mV s^{-1}) in Ar-purged electrolytes were subtracted from all polarization curves. This same procedure was repeated after each $NaBH_4$ addition into the electrolyte ($NaBH_4$ concentration of 0, 10, 20, 40, and 60 mM). All measurements were corrected from Ohmic drop. Mass activity ($i_{MA} = \frac{i_k}{m}$ at 0.85 V *vs*. RHE, where m is the catalyst mass onto the glassy carbon electrode) was calculated from the kinetic current density for ORR (i_k) obtained by using the Koutecky Levich equation:

$$i_k = -\frac{(i_L.i)}{(i_L - i)} \qquad (3.3)$$

where i_L is the O_2 diffusion-limited current density at 0.2 V *vs*. RHE and i is the Faradaic current corrected as described above.

3.3 Results and Discussion

3.3.1 Physicochemical Properties

Detailed physicochemical characterizations of the catalysts have been previously published by Zitolo *et al*. [48, 53], Choi *et al*. [50], and Kumar *et a*l. [51]. High-resolution transmission electron microscopy and ^{57}Fe Mössbauer spectroscopy showed that the catalysts with 0.5 wt.% metal content before pyrolysis (*ca*. 1.5 wt.% metal content after pyrolysis, due to the mass loss of *ca*. 66% experienced by the sacrificial metal-organic framework ZIF-8 during pyrolysis) feature only atomically-dispersed metal atoms coordinated by nitrogen atoms and embedded into a carbon matrix (FeN_x sites). In contrast, the catalysts prepared with 5.0 wt.% metal content before pyrolysis (*ca*. 15 wt.% metal after pyrolysis) resulted in either metallic (Co) or metal carbide (Fe_3C) nanoparticles surrounded by carbon-nitrogen shell. No atomically-dispersed metal atoms coordinated by nitrogen atoms were detected from the spectroscopic characterization of these samples. The Mössbauer or EXAFS spectroscopic detection limit for FeN_x sites is *ca*. 5% relative to the total amount of Fe; so the absence of detection of FeN_x sites monitored by these techniques for the 5.0 wt.%-loaded Fe–N–C sample (*ca*. 15 wt.% Fe total content after pyrolysis) means that, at maximum, 0.75 wt.% Fe might be present as FeN_x sites in this catalyst. In comparison, the 0.5 wt.%-loaded Fe–N–C sample (1.5 wt.% Fe bulk content after pyrolysis) only contains FeN_x sites, and this implies that the absolute number of FeN_x sites in the latter is at least double than that in the 5.0 wt.%-loaded Fe– N–C sample. Raman spectroscopy and X-ray diffraction provided evidences that the content of carbon nanocrystallites (*i.e*., more graphitic carbon phase, with lower amount of surface defects and oxygen functional groups) increases with the increase of metal content. Because ramp pyrolysis results in slow but continuous escape of the volatile products from ZIF-8 and phenanthroline decomposition, *ca*. twice higher Brunauer–Emmett–Teller (BET) surface area was observed for the ramp-pyrolyzed Fe catalyst with 0.5 wt.% Fe content compared with the flash pyrolyzed one [49]. However, this change mostly results in higher microporous surface area but little affects the meso- and macroporous surface areas [49]. In what follows, we refer to the catalysts as M_x mode, where M is Fe or Co, x is the weight percent metal in the powder composed of mixed precursors before pyrolysis, either 0.5 or 5.0 and "mode" is the pyrolysis mode (either ramp or flash pyrolysis, RP and FP, respectively).

3.3.2 Electrochemical Properties

In agreement with our former findings [54], it is found that (i) all the electrocatalyst materials present very interesting ORR activity in alkaline electrolyte and (ii) Fe–N–C electrocatalysts perform better than Co–N–C ones, independently of their structure and BET surface area. To probe their tolerance to sodium borohydride, the electrocatalysts were tested subsequently in $NaBH_4$-free and $NaBH_4$-containing Ar-saturated electrolytes. Figure 3.1 shows the cyclic voltammograms obtained at 10 mV s^{-1} for all synthesized catalysts in 0.1 M NaOH electrolytes with different contents of $NaBH_4$, in the absence of O_2. These results reveal that none of the tested electrocatalysts is totally insensitive to the presence of BH_4^- anions in the electrolyte: all of them show non-negligible oxidation current in the "high-potential range," the magnitude of which increases with the $NaBH_4$ concentration, signing that they present some activity towards the electrooxidation of the BH_4^- anion. However, clear differences can be seen when results for Fe–N–C and Co–N–C electrocatalysts are compared.

Focusing firstly on the Fe-containing materials (Figure 3.1a), one notices that the 5.0 wt.%-loaded Fe–N–C sample is much more sensitive to the presence of $NaBH_4$ than its 0.5

wt.% counterparts (the oxidation current monitored is *ca*. 10 times larger in the former than in the latter cases). These results are ascribed to the presence of Fe_3C nanoparticles in the $Fe_{5.0}RP$ catalyst (which may contain no FeN_x sites at all, and in the most favorable hypothesis for minor fraction of co-existing FeN_x sites, does not contain more FeN_x sites than the $Fe_{0.5}RP$ catalyst - see "3.3.1 Physicochemical Properties"), whereas the two other samples ($Fe_{0.5}FP$ and $Fe_{0.5}RP$) exclusively contain atomically-dispersed iron coordinated by nitrogen ligands (FeN_x sites). It is believed that the lower reactivity of the $Fe_{0.5}$ catalysts is related to the absence (or limited amounts) of neighbor sites required for the BH_4^- anion adsorption and its subsequent oxidation. Comparing the Fe–N– C electrocatalysts prepared by the ramp pyrolysis (RP) or the flash pyrolysis (FP), results do not enable to differentiate the samples: $Fe_{0.5}RP$ and $Fe_{0.5}FP$ present similar reactivity in the presence of $NaBH_4$ and are leading to very moderate BOR current (both contain atomically-dispersed iron).

Co-containing samples are, at given metal fraction, far more reactive for the BOR than their Fe-containing counterparts. $Co_{0.5}RP$, although presenting atomically-dispersed Co coordinated by N-ligands, leads to significant BOR currents particularly for $NaBH_4$ concentration higher than 20 mM, and the situation is even worse for the $Co_{5.0}RP$ sample, which is constituted of Co nanoparticles (Figure 3.1b, see inserted image for better visualization). In this last case, the electrode process must involve significant H_2 release by BH_4^- hydrolysis, as evidenced by the instability of the catalyst thin-film, which prevented measurements for $NaBH_4$ concentrations above 20 mM. These results illustrate the high ability of Co–N–C electrocatalysts to promote reactions with $NaBH_4$. This property is not surprising for the $Co_{5.0}RP$ sample, owing to the already-reported activity of Co electrocatalysts for the BOR [55, 56] or for the hydrolysis of BH_4^- followed by hydrogen release and subsequent oxidation [57–59]. The present results show that atomically-dispersed Co is also a good BOR electrocatalyst (Hannauer *et al*. reported the activity of Co^{x+} (x = 2, 3) cations for BH_4^- hydrolysis [60], but not for the BOR).

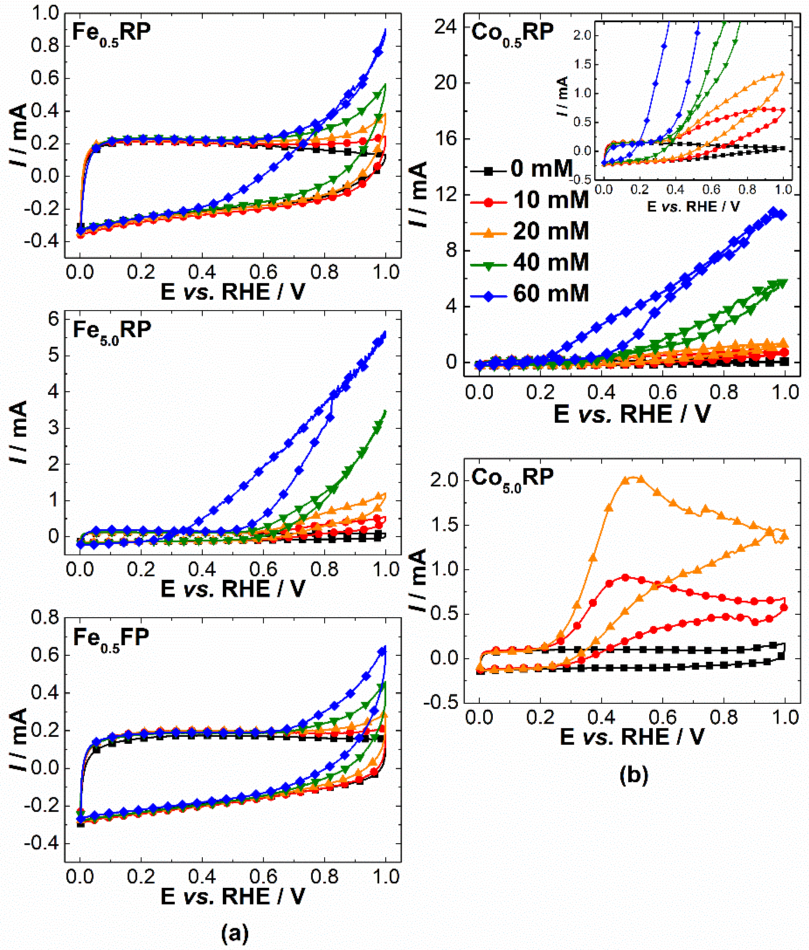

(a) (b)

Figure 3.1 Cyclic voltamperograms measured on **(a)** Fe–N–C and **(b)** Co–N–C electrocatalysts in Ar-purged 0.1 M NaOH supporting electrolyte containing increasing concentrations of $NaBH_4$: 0, 10, 20, 40, and 60 mM. All the tests were performed at 25 °C and 10 mV s^{-1}; the M–N–C electrocatalyst loading on the RDE tip was in all measurements 0.8 mg_{powder} cm^{-2}. For the $Co_{5.0}$RP sample, the active layer was destroyed for [$NaBH_4$] > 20 mM

The electrocatalysts were then tested for the ORR in the absence and presence of $NaBH_4$ at several concentrations in O_2-saturated electrolytes (Figure 3.2). In all cases, the "direct" measurement of the ORR in the presence of $NaBH_4$ (represented by the curves (3), in symbols) are compared with the "reconstructed" ones, for which the ORR currents in absence of $NaBH_4$ are added to the currents of BH_4^- oxidation in Ar-saturated supporting electrolyte (represented by the curves (4 + 2), in dotted lines). For the majority of the electrocatalysts considered, the "direct" and "reconstructed" curves of ORR in the presence of $NaBH_4$ are nearly-superposed; this means that the processes at stake on these class of materials are indeed the sum of the ORR and of the BOR (or of BH_4^- hydrolysis followed by the oxidation of the produced H_2), meaning that the processes are independent from each other.

Furthermore, one clearly sees that not all the electrocatalysts have the same reactivity for the ORR in the presence of $NaBH_4$, in agreement to the conclusions obtained from Figure

3.1. Firstly, Fe– N–C electrocatalysts presenting only atomically-dispersed iron ($Fe_{0.5}$RP and $Fe_{0.5}$FP) are somewhat tolerant to $NaBH_4$: the ORR activity in presence of 10 mM $NaBH_4$ is hardly changed compared with its value in absence of $NaBH_4$. However, increasing the $NaBH_4$ concentration progressively from 10 to 60 mM leads to an increase of BOR contribution to the total current, causing a slight negative shift of the apparent ORR onset potential (a sign of depreciated ORR kinetics and/or appearance of mixed electrode potentials, Figure 3.2a). Surprisingly, increasing $NaBH_4$ concentrations lead to practically unaffected absolute value of the ORR-limiting currents (see curves (3), symbols), which one could associate to similar number of electrons involved in ORR electrocatalysis even in the presence of strong reducer. Another interesting aspect is the smaller "direct" ORR-limiting currents compared with the sum of the ORR and the BOR (see curves (4 + 2), dotted lines); it can be related to the reduction of oxygen by BH_4^- anions on the catalysts surface, which in fact reduces the local effective concentration of O_2 in the "direct" measurements.

In contrast, when Fe_3C nanoparticles are present ($Fe_{5.0}$RP), the BH_4^- tolerance is no longer maintained: the ORR activity of $Fe_{5.0}$RP is severely affected by increasing amounts of $NaBH_4$, and even at 10 mM $NaBH_4$, the reaction onset potential is severely negatively shifted (by more than 100 mV; the negative shift being > 400 mV for 60 mM $NaBH_4$). Moreover, increasing $NaBH_4$ concentration leads to decreased absolute values of ORR-limiting currents, which indicates a lower number of electrons involved in the O_2 electrocatalysis and/or a drastic reduction of O_2 concentration in the catalyst surface (probably because of a reaction of O_2 or ORR intermediates (*i.e.*, HO_2^-) with BH_4^- or H_2 [36]). Not surprisingly, Co–N–C samples, which showed non-negligible activity towards the BOR (Figure 3.1), are not capable to maintain their good ORR activity in presence of $NaBH_4$ in the electrolyte, even at low concentration (Figure 3.2b). Of course, in the presence of Co nanoparticles ($Co_{5.0}$RP), the $NaBH_4$ tolerance is even worse as compared with that of atomically-dispersed Co ($Co_{0.5}$RP).

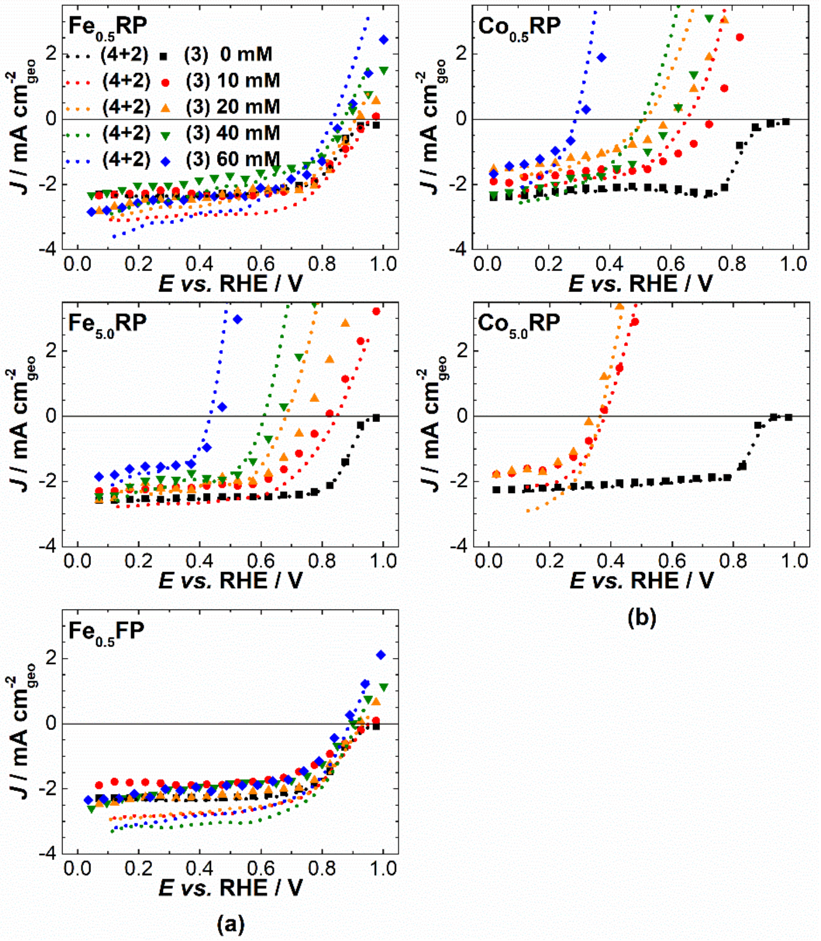

(a)

(b)

Figure 3.2 Cyclic voltamperograms of oxygen reduction reaction measured on **(a)** Fe–N–C and **(b)** Co–N–C electrocatalysts in O_2-purged 0.1 M NaOH supporting electrolyte containing increasing concentrations of $NaBH_4$: 0, 10, 20, 40 and 60 mM. All the tests were performed at 25 °C, 400 rpm, and 5 mV s^{-1}; the M–N–C electrocatalyst loading on the RDE tip was in all measurements 0.8 mg_{powder} cm^{-2}. (symbols) “direct” experimental curves of ORR in the presence of $NaBH_4$; (dotted lines) sum of current of ORR in absence of $NaBH_4$ with those for the BOR (similar as Figure 3.1)

The ORR onset potential (E_{onset}), half-wave potential ($E_{half\text{-}wave}$), and mass activity (i_{MA} at 0.85 V *vs*. RHE) of all the electrocatalysts were determined in the “direct” ORR experiments as a function of the $NaBH_4$ concentration in the electrolyte, as shown in Figure 3.3. The drastic reduction of the onset and half-wave potentials observed in Figure 3.3a, b confirms that for $Fe_{5.0}$RP or Co–N–C samples ($Co_{0.5}$RP and the $Co_{5.0}$RP), the tolerance to $NaBH_4$ is insufficient: these electrocatalysts present highly degraded ORR performances both in the kinetically-controlled and in the mixed kinetic-diffusion-controlled regions as soon as some $NaBH_4$ is present in the electrolyte.

In this way, the results evidence that only the atomically-dispersed Fe–N–C electrocatalysts present a sufficient tolerance to BH_4^- to be used as ORR electrocatalysts in a DBFC cathode, even though their ORR performances would start to non-negligible decrease if the crossover of $NaBH_4$ is significant and the BH_4^- concentration at the cathode exceeds a few 10 mM. This is further highlighted by results in Figure 3.3c, which demonstrate that the intrinsic mass activity of the $Fe_{0.5}$RP and $Fe_{0.5}$FP electrocatalysts is not drastically affected by concentrations of $NaBH_4$ in the NaOH supporting electrolyte, at least for BH_4^- concentrations of the order of 10 mM. These results also show that the electrocatalyst prepared by ramp pyrolysis ($Fe_{0.5}$RP) is a little more tolerant than the one prepared by flash pyrolysis ($Fe_{0.5}$FP). This behavior may be related to the above mentioned difference in BET surface area, which facilitates the access of oxygen molecules. Note however that this effect progressively vanishes by increasing $[BH_4^-]$ concentrations in solution to values that far exceed the O_2 solubility (1–2 mM).

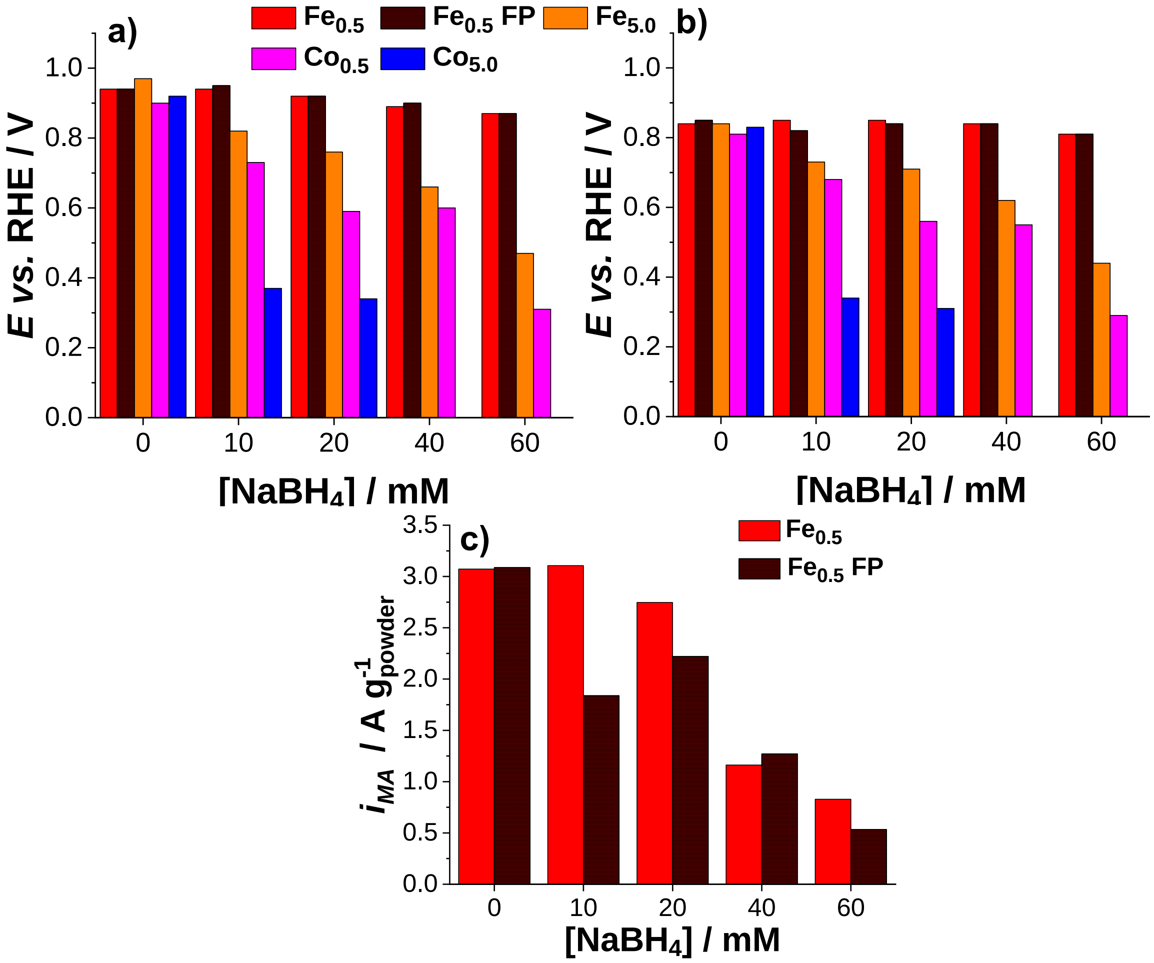

Figure 3.3 Determination of representative oxygen reduction reaction kinetic parameters for the Fe–N–C and Co–N–C electrocatalysts measured in O_2-purged 0.1 M NaOH supporting electrolyte containing increasing concentrations of $NaBH_4$: 0, 10, 20, 40, and 60 mM. All the tests were performed at 25 °C, 400 rpm, and 5 mV s^{-1}; the M–N–C electrocatalyst loading on the RDE tip was in all measurements 0.8 mg_{powder} cm^{-2}. **(a)** ORR onset potential and **(b)** ORR half-wave potential, measured for all the M–N–C electrocatalysts; **(c)** ORR mass activities measured at 0.85 V *vs.* RHE (corrected from mass-transfer limitation) for the atomically-dispersed Fe–N–C electrocatalysts (the measurement made no sense for the other electrocatalysts)

3.4 Conclusions

The present study shows that by tuning the nature of the metal center, its structure (atomic dispersion *vs.* nanoparticles) and the BET surface area of the carbonaceous structure, the tolerance of the ORR to $NaBH_4$, can be enhanced in the potential range of a direct borohydride fuel cell cathode. Evidences of a positive structural effect on the tolerance to BH_4^- competition were obtained for catalysts containing atomically-dispersed Fe and Co sites, the latter being magnified for Fe-containing electrocatalysts because of combined poor activity towards the BOR and high activity towards the ORR. A small but non-negligible effect of the microporous surface area was observed; however, it is believed that it relates to higher density of active sites in catalysts after ramp compared with flash pyrolysis. These findings thus open the door to enhanced electrocatalysts for the DBFC both at atomic and macroscopic levels.

3.5 References

1 T.B. Reddy, D. Linden, **Linden's Handbook of Batteries**, 4th edn. (McGraw-Hill Professional, New York, 2010)

2 W. Vielstich, A. Lamm, H.A. Gasteiger, **Handbook of Fuel Cells: Fundamentals, Technology and Applications** (Wiley, Chichester, 2003)

3 S. Wasmus, A. Küver, Methanol oxidation and direct methanol fuel cells: a selective review. **J. Electroanal. Chem.** 461(1-2), 14–31 (1999)

4 W. Vielstich, H.A. Gasteiger, H. Yokokawa, **Handbook of fuel fells: Fundamentals, technology and application**s (Wiley, Chichester, 2009)

5 J.S. Spendelow, A. Wieckowski, Electrocatalysis of oxygen reduction and small alcohol oxidation in alkaline media. **Phys. Chem. Chem. Phys**. 9(21), 2654–2675 (2007)

6 J.H. Wee, Which type of fuel cell is more competitive for portable application: direct methanol fuel cells or direct borohydride fuel cells? **J. Power Sources** 161(1), 1–10 (2006)

7 U.B. Demirci, Direct liquid-feed fuel cells: thermodynamic and environmental concerns. **J. Power Sources** 169(2), 239–246 (2007)

8 S.C. Amendola, P. Onnerud, M.T. Kelly, P.J. Petillo, S.L. Sharp- Goldman, M. Binder, A novel high power density borohydride-air cell. **J. Power Sources** 84(1), 130–133 (1999)

9 C. Kim, K.-J. Kim, M.Y. Ha, Investigation of the characteristics of a stacked direct borohydride fuel cell for portable applications. **J. Power Sources** 180(1), 114–121 (2008)

10 B.H. Liu, Z.P. Li, Current status and progress of direct borohydride fuel cell technology development. **J. Power Sources** 187(2), 291– 297 (2009)

11 J. Ma, N.A. Choudhury, Y. Sahai, A comprehensive review of direct borohydride fuel cells. **Renew. Sust. Energ. Rev.** 14(1), 183–199 (2010)

12 G. Rostamikia, M.J. Janik, Direct borohydride oxidation: mechanism determination and design of alloy catalysts guided by density functional theory. **Energy Environ. Sci.** 3(9), 1262–1274 (2010)

13 M. Chatenet, M.B. Molina-Concha, J.-P. Diard, First insights into the borohydride oxidation reaction mechanism on gold by electrochemical impedance spectroscopy. **Electrochim. Acta** 54(6), 1687– 1693 (2009)

14 D.A. Finkelstein, N. Da Mota, J.L. Cohen, H.D. Abruña, Rotating disk electrode (RDE) investigation of BH_4^- and BH_3OH^- electro-oxidation at Pt and Au: implications for BH_4^- fuel cells. **J. Phys.Chem. C** 113(45), 19700–19712 (2009)

15 B. M. Concha, M. Chatenet, E.A. Ticianelli, F.H.B. Lima, *In situ* infrared (FTIR) study of the mechanism of the borohydride oxidation reaction on smooth Pt electrode. **J. Phys. Chem. C** 115(25), 12439–12447 (2011)

16 P.-Y. Olu, A. Bonnefont, M. Rouhet, S. Bozdech, N. Job, M. Chatenet, E. Savinova, Insights into the potential dependence of the borohydride electrooxidation reaction mechanism

on platinum nanoparticles supported on ordered carbon nanomaterials. **Electrochim. Acta** 179,637–646 (2015)

17 M.C.S. Escaño, R.L. Arevalo, E. Gyenge, H. Kasai, Electrocatalysis of borohydride oxidation: a review of density functional theory approach combined with experimental validation. **J. Phys, Condens. Matter** 26(35), (2014)

18 P.-Y. Olu, A. Bonnefont, M. Chatenet, "Borohydride Oxidation Reaction (BOR) at Pt and Au electrodes: From experimental insights to mechanism and kinetic modeling". In **Encyclopedia Interfacial Chemistry: Surface Science and Electrochemistry**, K. Wandelt (Ed.). (Elsevier, 2018), pp. 384–392

19 P.-Y. Olu, A. Zadick, N. Job, M. Chatenet, "Anode Electrocatalysts for Direct Borohydride and Direct Ammonia Borane Fuel Cells". In **Electrocatalysts for Low Temperature Fuel Cells: Fundamentals and Recent Trends**, T. Maiyalagan, V. S. Saji (Eds.). (Wiley, 2017), pp. 317–346

20 I. Merino-Jiménez, C. Ponce De León, A.A. Shah, F.C. Walsh, Developments in direct borohydride fuel cells and remaining challenges. **J.Power Sources** 219,339–357 (2012)

21 K.S. Freitas, B.M. Concha, E.A. Ticianelli, M. Chatenet, Mass transport effects in the borohydride oxidation reaction—influence of the residence time on the reaction onset and faradaic efficiency. **Catal. Today** 170(1), 110–119 (2011)

22 S. Suda. "Aqueous borohydride solutions". In **Handbook of Fuel Cells - Fundamentals, Technology and Applications**, W. Vielstich, A. Lamm, H. A. Gasteiger (Eds.). (Wiley, Chichester, 2003), pp. 115–120

23 C. Ponce De León, F. C. Walsh, "Direct and indirect borohydride fuel cells". In **Reference Module in Chemistry: Molecular Sciences and Chemical Engineering** (Elsevier, 2015). https://doi.org/10. 1016/B978-0-12-409547-2.11190-4

24 Z. Wang, J. Parrondo, C. He, S. Sankarasubramanian, V. Ramani, Efficient pH-gradient-enabled microscale bipolar interfaces in direct borohydride fuel cells. **Nat. Energy** 4,281–289 (2019)

25 M. Chatenet, Tailoring membranes. Nat. Energy 4,261–262 (2019) 26. S. Ould-Amara, J. Dillet, S. Didierjean, M. Chatenet, G. Maranzana, Operating heterogeneities within a direct borohydride fuel cell. **J. Power Sources** 439, 227099 (2019)

27 K. N. Mochalov, V. S. Khain, G. G. Gil'manshin, A generalized scheme for the hydrolysis of the borohydride ion and diborane. **Dokl. Akad. Nauk SSSR** 162(3), 613–616 (1965)

28 M.M. Kreevoy, R.W. Jacobson, The rate of decomposition of $NaBH_4$ in basic aqueous solutions. **Vent. Alembic** 15,2–3 (1979)

29 D. Sebastián, A. Serov, I. Matanovic, K. Artyushkova, P. Atanassov, A.S. Aricò, V. Baglio, Insights on the extraordinary tolerance to alcohols of Fe-N-C cathode catalysts in highly performing direct alcohol fuel cells. **Nano Energy** 34, 195–204 (2017)

30 K.B. Ma, D.H. Kwak, S.B. Han, H.S. Park, D.H. Kim, J.E. Won, S.H. Kwon, M.C. Kim, S.H. Moon, K.W. Park, Direct ethanol fuel cells with superior ethanol-tolerant nonprecious

metal cathode catalysts for oxygen reduction reaction. **ACS Sustain. Chem. Eng**. 6(6), 7609–7618 (2018)

31 L. Osmieri, R. Escudero-Cid, A.H.A. Monteverde Videla, P. Ocón, S. Specchia, Application of a non-noble Fe-N-C catalyst for oxygen reduction reaction in an alkaline direct ethanol fuel cell. **Renew. Energy** 115,226–237 (2018)

32 A.C. Garcia, J.J. Linares, M. Chatenet, E.A. Ticianelli, $NiMnO_x/C$: a non-noble ethanol-tolerant catalyst for oxygen reduction in alkaline exchange membrane DEFC. **Electrocatalysis** 5,41–49 (2014)

33 E. A. Ticianelli, F. H. B. Lima, "Nanostructured Electrocatalysts for Methanol and Ethanol-Tolerant Cathodes". In **Direct Alcohol Fuel Cells: Materials, Performance, Durability and Applications**, H. R. Corti, E. R. Gonzalez (Eds.). (Springer, 2014), pp. 99–119

34 X. Yang, S. Li, Y. Liu, X.Wei, Y. Liu, $LaNi_{0.8}Co_{0.2}O_3$ as a cathode catalyst for a direct borohydride fuel cell. **J. Power Sources** 196(11), 4992–4995 (2011)

35 M. Chatenet, F. Micoud, I. Roche, E. Chainet, J. Vondrák, Kinetics of sodium borohydride direct oxidation and oxygen reduction in sodium hydroxide electrolyte: Part II. O_2 reduction. **Electrochim. Acta** 51(25), 5452–5458 (2006)

36 A.C. Garcia, F.H.B. Lima, E.A. Ticianelli, M. Chatenet, Carbon-supported nickel-doped manganese oxides as electrocatalysts for the oxygen reduction reaction in the presence of sodium borohydride. **J. Power Sources** 222,305–312 (2013)

37 I. Roche, E. Chaînet, M. Chatenet, J. Vondrák, Durability of carbon-supported manganese oxide nanoparticles for the oxygen reduction reaction (ORR) in alkaline medium. **J. Appl. Electrochem.** 38,1195–1201 (2008)

38 H. Cheng, K. Scott, Investigation of non-platinum cathode catalysts for direct borohydride fuel cells. **J. Electroanal. Chem.** 596(2), 117– 123 (2006)

39 M. Chatenet, F. Micoud, I. Roche, E. Chainet, Kinetics of sodium borohydride direct oxidation and oxygen reduction in sodium hydroxide electrolyte: Part I. BH_4^- electro-oxidation on Au and Ag catalysts. **Electrochim. Acta** 51(25), 5459–5467 (2006)

40 M.H. Atwan, D.O. Northwood, E.L. Gyenge, Evaluation of colloidal Ag and Ag-alloys as anode electrocatalysts for direct borohydride fuel cells. **Int. J. Hydrog. Energy** 32(15), 3116–3125 (2007)

41 A.V. N. Kumar, S. Harish, J. Joseph, New route for synthesis of electrocatalytic Ni(OH)2 modified electrodes—electrooxidation of borohydride as probe reaction. **Bull. Mater. Sci**. 37, 635–641 (2014)

42 D.M.F. Santos, B. Šljukić, L. Amaral, D. Macciò, A. Saccone, C.A.C. Sequeira, Nickel and nickel-cerium alloy anodes for direct borohydride fuel cells. **J. Electrochem. Soc.** 161(5), F594-F599 (2014)

43 A.G. Oshchepkov, G. Braesch, S. Ould-Amara, G. Rostamikia, G. Maranzana, A. Bonnefont, V. Papaefthimiou, M.J. Janik, M. Chatenet, E.R. Savinova, Nickel metal nanoparticles as anode electrocatalysts for highly efficient direct borohydride fuel cells. **ACS Catal**. 9(9), 8520–8528 (2019)

44 A. Serov, A. Aziznia, P.H. Benhangi, K. Artyushkova, P. Atanassov, E. Gyenge, Borohydride-tolerant oxygen electroreduction catalyst for mixed-reactant Swiss-roll direct borohydride fuel cells. **J. Mater. Chem. A** 1(45), 14384–14391 (2013)

45 M. Lefèvre, E. Proietti, F. Jaouen, and J.-P. Dodelet, Iron-based catalysts with improved oxygen reduction activity in polymer electrolyte fuel cells. **Science** 324 (5923), 71–74 (2009)

46 A. Serov, K. Artyushkova, E. Niangar, C. Wang, N. Dale, F. Jaouen, M.T. Sougrati, Q. Jia, S. Mukerjee, P. Atanassov, Nanostructured non-platinum catalysts for automotive fuel cell application. **Nano Energy** 16,293–300 (2015)

47 F. Luo, C.H. Choi, M.J.M. Primbs, W. Ju, S. Li, N.D. Leonard, A. Thomas, F. Jaouen, P. Strasser, Accurate evaluation of active-site density (SD) and turnover frequency (TOF) of PGM-free metal–nitrogen-doped carbon (MNC) electrocatalysts using CO cryo adsorption. **ACS Catal**. 9(6), 4841–4852 (2019)

48 A. Zitolo, N. Ranjbar-Sahraie, T. Mineva, J. Li, Q. Jia, S. Stamatin, G. F. Harrington, S. M. Lyth, P. Krtil, S. Mukerjee, E. Fonda, F. Jaouen, Identification of catalytic sites in cobalt-nitrogen-carbon materials for the oxygen reduction reaction. **Nat. Comm**. 8,957 (2017)

49 V. Armel, J. Hannauer, F. Jaouen, Effect of ZIF-8 crystal size on the O_2 electro-reduction performance of pyrolyzed Fe–N–C catalysts. **Catalysts** 5(3), 1333–1351 (2015)

50 C.H. Choi, H.K. Lim, M.W. Chung, G. Chon, N. Ranjbar Sahraie, A. Altin, M.T. Sougrati, L. Stievano, H.S. Oh, E.S. Park, F. Luo, P. Strasser, G. Dražić, K.J.J. Mayrhofer, H. Kim, F. Jaouen, The Achilles' heel of iron-based catalysts during oxygen reduction in an acidic medium. **Energy Environ. Sci.** 11,3176–3182 (2018)

51 K. Kumar, P. Gairola, M. Lions, N. Ranjbar-Sahraie, M. Mermoux, L. Dubau, A. Zitolo, F. Jaouen, F. Maillard, Physical and chemical considerations for improving catalytic activity and stability of non-precious-metal oxygen reduction reaction catalysts. **ACS Catal**. 8(12), 11264–11276 (2018)

52 V. Goellner, V. Armel, A. Zitolo, E. Fonda, F. Jaouen, Degradation by hydrogen peroxide of metal-nitrogen-carbon catalysts for oxygen reduction. **J. Electrochem. Soc**. 162(6), H403–H414 (2015)

53 A. Zitolo, V. Goellner, V. Armel, M.T. Sougrati, T. Mineva, L. Stievano, E. Fonda, F. Jaouen, Identification of catalytic sites for oxygen reduction in iron- and nitrogen-doped graphene materials. **Nat. Mater**. 14(9), 937–942 (2015)

54 R. Sgarbi, K. Kumar, F. Jaouen, A. Zitolo, E. A. Ticianelli, and F. Maillard, Oxygen reduction reaction mechanism and kinetics on M- N_xC_y and M@N-C active sites present in model M-N-C catalysts under alkaline and acidic conditions. **J. Solid State Electrochem**. (2019). https://doi.org/10.1007/s10008-019-04436-w

55 J. Ma, X. Gao, D. Wang, T. Xue, S. Yang, Effect of cobalt precursors on Co_3O_4 anodic catalyst for a membrane-free direct borohydride fuel cell. **J. Alloys Compd.** 724,474–480 (2017)

56 A. Tiwari, V. Singh, T.C. Nagaiah, Non-noble cobalt tungstate catalyst for effective electrocatalytic oxidation of borohydride. **ACS Appl. Mater. Interfaces** 11(24), 21465–21472 (2019)

57 A. Garron, D. Świerczyński, S. Bennici, A. Auroux, New insights into the mechanism of H_2 generation through $NaBH_4$ hydrolysis on Co-based nanocatalysts studied by differential reaction calorimetry. **Int. J. Hydrog. Energy** 34(3), 1185–1199 (2009)

58 J. Choi, J. Chung, Preparation and Characteristics of Novel Cobalt Oxide Catalysts for Hydrogen Generation from Metal Borohydride Solution. **J. Energy Eng**. 142(3), (2016)

59 R. Edla, S. Gupta, N. Patel, N. Bazzanella, R. Fernandes, D.C. Kothari, A. Miotello, Enhanced H_2 production from hydrolysis of sodium borohydride using Co_3O_4 nanoparticles assembled coatings prepared by pulsed laser deposition. **Appl. Catal. A Gen**. 515,1–9 (2016)

60 J. Hannauer, U.B. Demirci, C. Geantet, J.M. Herrmann, P. Miele, Enhanced hydrogen release by catalyzed hydrolysis of sodium borohydride-ammonia borane mixtures: a solution-state ^{11}B NMR study. **Phys. Chem. Chem. Phys**. 13(9), 3809–3818 (2011)

Conclusions and Perspectives

This thesis contains studies of Fe-N-C and Co-N-C electrocatalysts towards the oxygen reduction reaction. The final goal of these investigations is to understand the electrocatalytic features of M-N-C catalysts under different conditions. These electrocatalysts are formed by two main structures, one of then being formed by single metallic atoms coordinated with nitrogen/carbon moieties ($M-N_xC_y$) and the other by metallic nanoparticles embedded on a nitrogen-doped carbonaceous matrix (M@N-C). Their electrocatalytic features have been correlated to the physicochemical properties, such as the nature of metallic center, active sites, specific surface area and/or micropore surface area, size of nanoparticles and amount of metals in the catalyst. To allow these correlations the electrochemical (cyclic voltammetry and rotating (ring)disk electrode), spectroscopic (Raman, Mössbauer, XAS, XPS and X-EDS) microscopic (TEM), physisorption (BET method), spectrometric (ICP-MS) and diffractometric (XRD) techniques have been employed.

Chapter 1 discusses the pH effect on the ORR electrocatalytic activity for synthesized catalysts featuring $M-N_xC_y$ or M@N-C active sites. Two factors that alter the ORR activity are identified: (i) the nature of the metallic center (Fe > Co) and (ii) the nature of the active sites. It is found that $M-N_xC_y$ and M@N-C active sites are more active when the ORR is performed in acidic and alkaline conditions, respectively. For the most active center ($Fe-N_xC_y$) in acidic conditions, this property was assigned to the formation of Fe^{2+} from Fe^{3+}/Fe^{2+} redox couple in direct contact with the electrolyte, the reactant, OH_{ads} moieties, and reaction intermediates, all with adequate energy binding with the surface. Fe@N-C led to the highest activity for Ar-pyrolyzed catalysts, displaying an effective synergistic effect between the iron in a metallic core surrounded by the nitrogen-carbon shells. It is emphasized that the indirect contact of the metallic center with surface-hydroxyl and other intermediates drives the ORR electrocatalysis more effectively. Further, Fe@N-C stabilizes HO_2^- intermediates adequately, resulting in the predominance of 4-electron transfer per oxygen molecule.

Interestingly, *in situ* Fe-based nanoparticles were grown with the temperature along AST under O_2 atmosphere at 60 °C and 25 °C, reaching the highest size at the lowest temperature, as detected by TEM and XRD. Further, the combined physicochemical and electrochemical findings indicate that the interconversion and/or partial oxidation of nitrogen- and oxygenated-surface-groups undergo more intensely for nanoparticles Fe-catalyst ($Fe_{5.0}$) than their counterpart atomically dispersed ($Fe_{0.5}$) on the surface and/or near-surface, as detected by XPS and confirmed by Raman spectroscopy and Cyclic Voltammetry. This effect combined with the demetallation of M@N-C moieties after AST loading cycles affects negatively the synergistic effect between the center metallic and the nitrogen-doped carbon shell. For atomically dispersed metal (M-N_xC_y), the depletion of ORR mass activity is governed by the metal loss to the electrolyte, as evidenced by X-EDS and ICP-MS measurements. Fe-N-C electrocatalysts are more stable than Co-based catalysts, indicating theirs as an excellent candidate for investigation on the anion-exchange membrane fuel cell and metal-air batteries.

Chapter 2 investigates the electrocatalysts corrosion resistance under alkaline conditions simulating load cycles on AEMFC cathodes. Two main processes that change the ORR electrocatalytic activity are reported: (i) nitrogen and oxygen functional groups interconversion and/or oxidation and (ii) demetallation of active sites. The first effect undergoes more intensely for nanoparticles Fe-catalyst ($Fe_{5.0}$) than their counterpart atomically dispersed ($Fe_{0.5}$) on the surface and/or near-surface. Further, the effect is combined with the demetallation of M@N-C moieties after AST loading cycles and it affects negatively the synergistic effect between the center metallic and the nitrogen-doped carbon shell. While, for atomically dispersed metal (M-N_xC_y), the depletion of ORR mass activity is governed by the metal loss to the electrolyte. Interestingly, *in situ* Fe-based nanoparticles were grown with the temperature along AST under O_2 atmosphere at 60 °C and 25 °C, reaching the highest size at the lowest temperature. These findings drive to future investigations of Fe-N-C catalysts mainly atomically-dispersed Fe electrocatalysts in AEMFC cathodes, including using long-term stress conditions.

Chapter 3 displays the tolerance of the ORR to $NaBH_4$, which was related to the nature of the metal center in the M-N-C catalyst, its structure (atomic dispersion *vs*. nanoparticles) and the micropore surface area of the carbonaceous clusters. In the potential range of interest for a direct borohydride fuel cell cathode (DBFC), evidence of a positive structural effect on the tolerance to BH_4^- was obtained for catalysts containing atomically-dispersed Fe and Co sites. This is magnified for Fe-containing electrocatalysts because they combine poor activity towards the BOR and high activity towards the ORR. Further, in this chapter, a fifth electrocatalyst containing atomically dispersed Fe with a lower BET surface area of carbon (and less microporous structures) than the former has been included. This allowed to identify the small effect of the microporous surface area, which in fact is related to the slight advantage for ORR mass activity in the presence of BH_4^- anions attributed to the higher active sites density in the micropore structures. These findings open the door to developing electrocatalysts for the DBFC both at atomic and macroscopic levels.

Overall results of these investigations confirm that the Fe-catalysts are ready for the next step of studies related to application tests as the cathode material for alkaline fuel cells, such as in anion-exchange membrane and direct borohydride fuel cells. This is reinforced by the fact that the atomically dispersed iron catalyst has shown a better balance between activity and durability towards ORR, as well as the best BH_4^- tolerance. Other interesting points that deserve future investigation are related to (i) establishment of a correlation of iron-based nanoparticles re-deposition and their sizes at intermediate temperatures of cycling between 25 °C and 100 °C under O_2-saturated electrolytes, (ii) characterize this effect for the atomically dispersed iron using lower specific surface area carbon catalysts and (iii) characterize the behavior of the catalysts when submitted to the start/stop cycles between 1.0 and 1.5 V *vs.* RHE, for simulating the shut-down period of a fuel cell.

Appendix 1

Table A1.1 RDE/RRDE results in alkaline electrolyte. Summary of results and errors in O_2-saturated 0.1 mol L^{-1} NaOH for onset and half-wave potential, Mass Activity (i_{MA}) at 0.85 V, Tafel slope (*a*: 0.9 to 0.8 V), number of electrons transferred during the ORR (n_{e-}) and percentage of HO_2^-. All measurements were performed at 5 mV s^{-1}, 1600 rpm and 25 °C. Catalyst loading for i) RDE: 0.8 mg_{powder} cm^{-2}; and ii) RRDE: 0.1 mg_{powder} cm^{-2} for M_0, $Fe_{0.5}$, $Fe_{5.0}$, $Co_{0.5}$ and $Co_{5.0}$; i) RDE: 20 μg_{Pt} cm^{-2}; and ii) RRDE: 10 μg_{Pt} cm^{-2} for Pt/C. (*b*: 0.87 to 0.80 V)

0.1 mol L^{-1} NaOH										
Catalyst	**E_{onset} / V**	**$E_{half-wave}$ / V**	**i_{MA} at 0.85 V / A g_{powder}^{-1}**	**Tafel Slope / mV dec^{-1}**	**n_{e-} / electrons**			**%[HO_2^-]**		
					0.2 V	**0.4 V**	**0.6 V**	**0.2 V**	**0.4 V**	**0.6 V**
M_0	0.87 ± 0.01	0.70 ± 0.01	0.081 ± 0.0264	60 ± 2.1^b	2.60	2.55	2.67	53.8	57.0	49.7
$Fe_{0.5}$	0.95 ± 0.01	0.82 ± 0.01	3.185 ± 0.4084	81 ± 1.5^a	3.73	3.72	3.91	7.14	7.57	2.44
$Fe_{5.0}$	0.97 ± 0.01	0.84 ± 0.01	4.903 ± 1.0056	82 ± 2.0^a	3.80	3.80	3.91	5.20	5.40	2.42
$Co_{0.5}$	0.90 ± 0.01	0.80 ± 0.01	0.668 ± 0.0426	54 ± 2.7^a	2.71	2.64	2.67	47.5	51.5	50.1
$Co_{5.0}$	0.93 ± 0.01	0.83 ± 0.01	1.970 ± 0.1903	46 ± 1.1^a	2.94	2.86	2.89	35.9	39.8	38.6
Pt/C	0.97 ± 0.01	0.84 ± 0.01	83.16 ± 0.0007	62 ± 0.4^a	3.88	3.92	3.92	3.06	2.06	1.97

Table A1.2 RDE/RRDE results in acid electrolyte. Summary of results and errors in O_2-saturated 0.1 mol L^{-1} H_2SO_4 for onset and half-wave potential, Mass Activity (i_{MA}) at 0.85 V, Tafel slope (*a*: 0.9 to 0.8 V), number of electrons transferred during the ORR (n_{e-}) and percentage of H_2O_2. All measurements were performed at 5 mV s^{-1}, 1600 rpm and 25 °C. Catalyst loading for i) RDE: 0.8 mg_{powder} cm^{-2}; and ii) RRDE: 0.1 mg_{powder} cm^{-2} for M_0, $Fe_{0.5}$, $Fe_{5.0}$, $Co_{0.5}$ and $Co_{5.0}$; i) RDE: 20 μg_{Pt} cm^{-2}; and ii) RRDE: 10 μg_{Pt} cm^{-2} for Pt/C. (*c*: 0.81 to 0.71 V; *d*: 0.82 to 0.8 V; *e*: 0.84 to 0.8 V).

0.1 mol L^{-1} H_2SO_4										
Catalyst	**E_{onset} / V**	**$E_{half-wave}$ / V**	**i_{MA} at 0.85 V / A g_{powder}^{-1}**	**Tafel Slope / mV dec^{-1}**	**n_{e-} / electrons**			**%[H_2O_2]**		
					0.2 V	**0.4 V**	**0.6 V**	**0.2 V**	**0.4 V**	**0.6 V**
M_0	0.81 ± 0.01	0.55 ± 0.02	0.074 ± 0.0044	160 ± 0.4^c	3.23	3.25	3.36	23.9	23.1	19.2
$Fe_{0.5}$	0.92 ± 0.01	0.79 ± 0.01	0.937 ± 0.2338	73 ± 0.5^a	3.53	3.43	3.48	13.4	16.8	14.9
$Fe_{5.0}$	0.90 ± 0.01	0.74 ± 0.02	0.499 ± 0.0941	75 ± 0.7^a	3.49	3.36	3.34	14.7	19.2	19.6
$Co_{0.5}$	0.82 ± 0.01	0.66 ± 0.01	0.078 ± 0.0104	55 ± 1.5^d	2.69	2.96	3.25	48.6	35.2	23.0
$Co_{5.0}$	0.84 ± 0.01	0.73 ± 0.01	0.028 ± 0.0061	37 ± 1.2^e	2.70	2.49	2.45	48.4	60.8	61.5
Pt/C	0.96 ± 0.01	0.84 ± 0.01	34.22 ± 5.535	96 ± 1.0^a	3.96	3.97	3.97	1.10	0.88	0.74

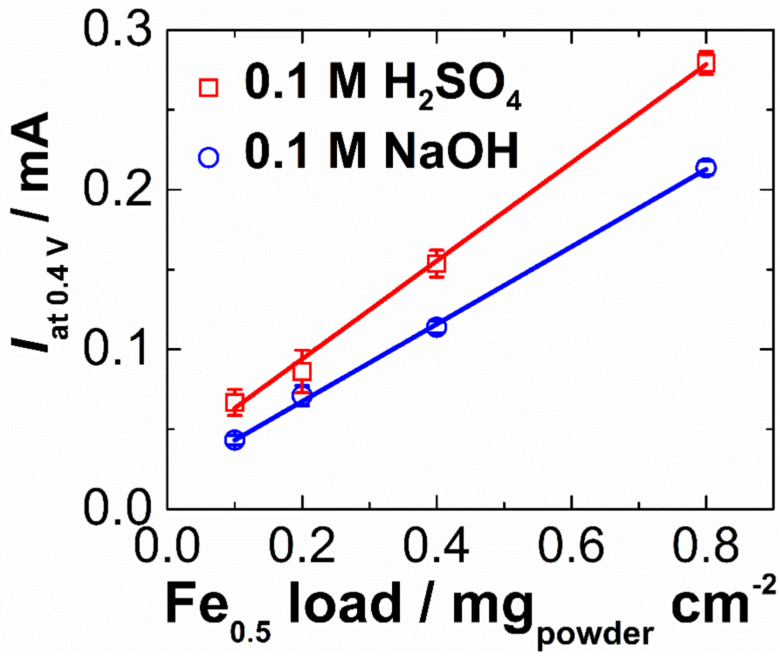

Figure A1.1 Capacitive current trends of different $Fe_{0.5}$ catalyst loadings. Values of capacitive currents collected at 0.4 V in 0.1, 0.2, 0.4 and 0.8 mg_{powder} cm^{-2} catalyst loadings from CVs in Ar-saturated electrolyte 0.1 mol L^{-1} (red) H_2SO_4 and (blue) NaOH at 10 mV s^{-1}. All measurements were performed at 25 °C.

Table A1.3 RDE results in alkaline electrolyte for different $Fe_{0.5}$ catalyst loadings. Summary of results and errors in O_2-saturated 0.1 mol L^{-1} NaOH for onset and half-wave potential, Mass Activity (i_{MA}) at 0.85 V, Tafel slope (a: 0.9 to 0.8 V). All measurements were performed at 5 mV s^{-1}, 1600 rpm and 25 °C.

0.1 mol L^{-1} NaOH				
$Fe_{0.5}$ Load / mg_{powder} cm^{-2}	**E_{onset} / V**	**$E_{half\text{-}wave}$ / V**	**i_{MA} at 0.85 V / A g_{powder}^{-1}**	**Tafel Slope^a / mV dec^{-1}**
0.8	0.95 ± 0.01	0.82 ± 0.01	3.185 ± 0.4084	81 ± 1.5
0.4	0.94 ± 0.01	0.79 ± 0.01	3.557 ± 0.7293	84 ± 1.5
0.2	0.93 ± 0.01	0.75 ± 0.01	3.465 ± 1.3422	79 ± 1.6
0.1	0.93 ± 0.01	0.74 ± 0.01	4.416 ± 1.2669	82 ± 1.5

Table A1.4 RDE results in acid electrolyte for different $Fe_{0.5}$ catalyst loadings. Summary of results and errors in O_2-saturated 0.1 mol L^{-1} H_2SO_4 for onset and half-wave potential, Mass Activity (i_{MA}) at 0.85 V, Tafel slope (*a*: 0.9 to 0.8 V). All measurements were performed at 5 mV s^{-1}, 1600 rpm and 25 °C.

0.1 mol L^{-1} H_2SO_4				
$Fe_{0.5}$ Load / mg_{powder} cm^{-2}	**E_{onset} / V**	**$E_{half\text{-}wave}$ / V**	**i_{MA} at 0.85 V / A g_{powder}^{-1}**	**Tafel Slope^{a} / mV dec^{-1}**
0.8	0.92 ± 0.01	0.79 ± 0.01	0.937 ± 0.2338	73 ± 0.5
0.4	0.91 ± 0.01	0.77 ± 0.01	0.891 ± 0.2129	76 ± 0.3
0.2	0.90 ± 0.01	0.74 ± 0.01	0.825 ± 0.1186	74 ± 0.3
0.1	0.88 ± 0.01	0.70 ± 0.01	0.707 ± 0.1438	75 ± 0.6

Appendix 2

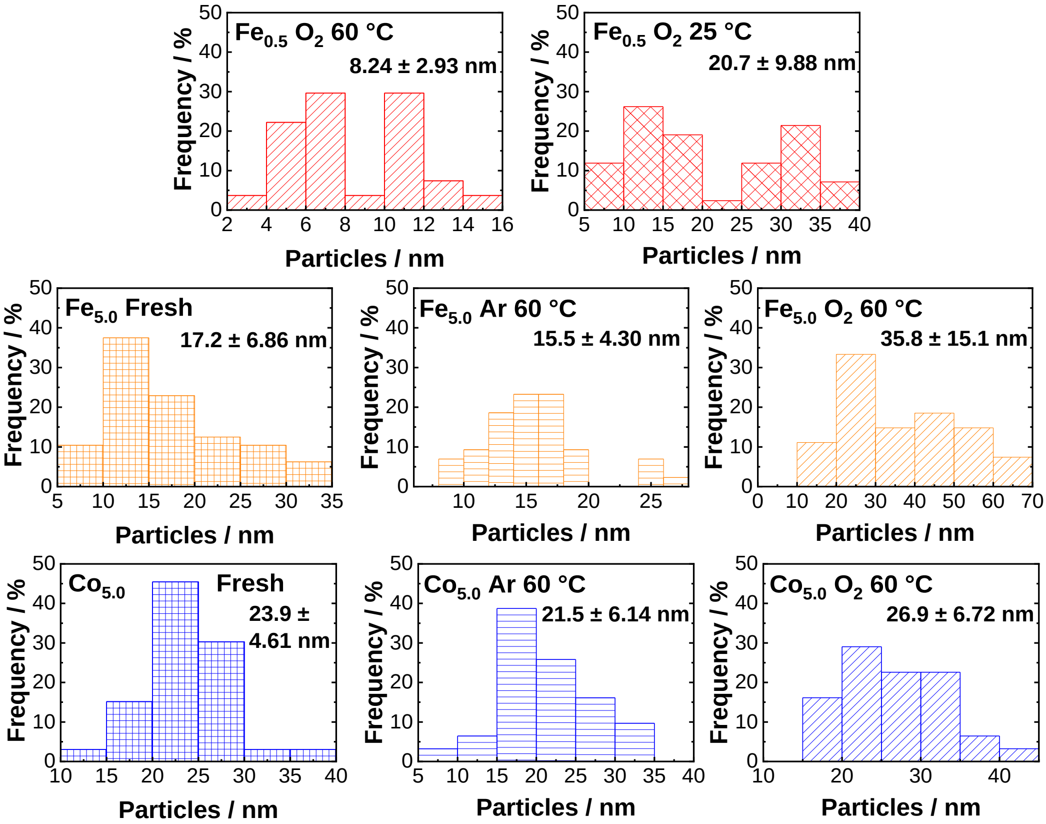

Figure A2.1. Particle size distribution histogram obtained from TEM images for the catalysts before and after 10,000 AST load cycles in Ar and O_2-saturated NaOH 0.1 mol L^{-1} at 60 °C. Also at 25 °C and O_2 for $Fe_{0.5}$ catalyst.

Table A2.1. X-ray photoelectron spectroscopy data of O 1s, N 1s, C1s deconvoluted signals of the $Fe_{0.5}$ and $Fe_{5.0}$ catalysts before and after 10,000 AST loading cycles under Ar-purged 0.1 mol L^{-1} NaOH electrolyte at 60 °C

Catalyst	**O 1s /at.%**			
	C=O/O=C-OH[a] (531.2-531.4 eV)	**C-O-H/C-O-C** (532.1 eV)	**O=C-OH**[b]**/O=C-OR** (533.0-533.3 eV)	**peroxy(ester/acid)** (535.1-535.3 eV)
$Fe_{0.5}$ Fresh	32.3	39.0	8.0	20.7
$Fe_{0.5}$ Ar 60 °C	32.5	37.4	11.0	19.1
$Fe_{5.0}$ Fresh	13.5	55.8	9.6	21.1
$Fe_{5.0}$ Ar 60 °C	28.7	42.8	7.3	21.2

a: O doubly-bonded with C; *b*: O singly-bonded with C

Catalyst	**N 1s /at.%**			
	Pyridinic (398.0-398.4 eV)	**Pyrrolic** (399.8-400.2 eV)	**Graphitic** (401.4 eV)	**Oxidized** (403.4 eV)
$Fe_{0.5}$ Fresh	19.3	69.3	6.9	4.5
$Fe_{0.5}$ Ar 60 °C	18.0	71.6	6.1	4.3
$Fe_{5.0}$ Fresh	13.4	78.6	8.0	0.0
$Fe_{5.0}$ Ar 60 °C	18.1	61.9	14.0	6.0

Catalyst	**C 1s /at.%**			
	C-C (284.3 eV)	**C-O** (285.6 - 286.0 eV)	**C=O** (287.1 - 287.7 eV)	**O=C-O** (289.0 - 289.3 eV)
$Fe_{0.5}$ Fresh	65.7	18.3	9.7	6.3
$Fe_{0.5}$ Ar 60 °C	63.8	19.6	9.9	6.7
$Fe_{5.0}$ Fresh	54.4	21.7	11.3	12.6
$Fe_{5.0}$ Ar 60 °C	63.9	18.8	8.3	9.0

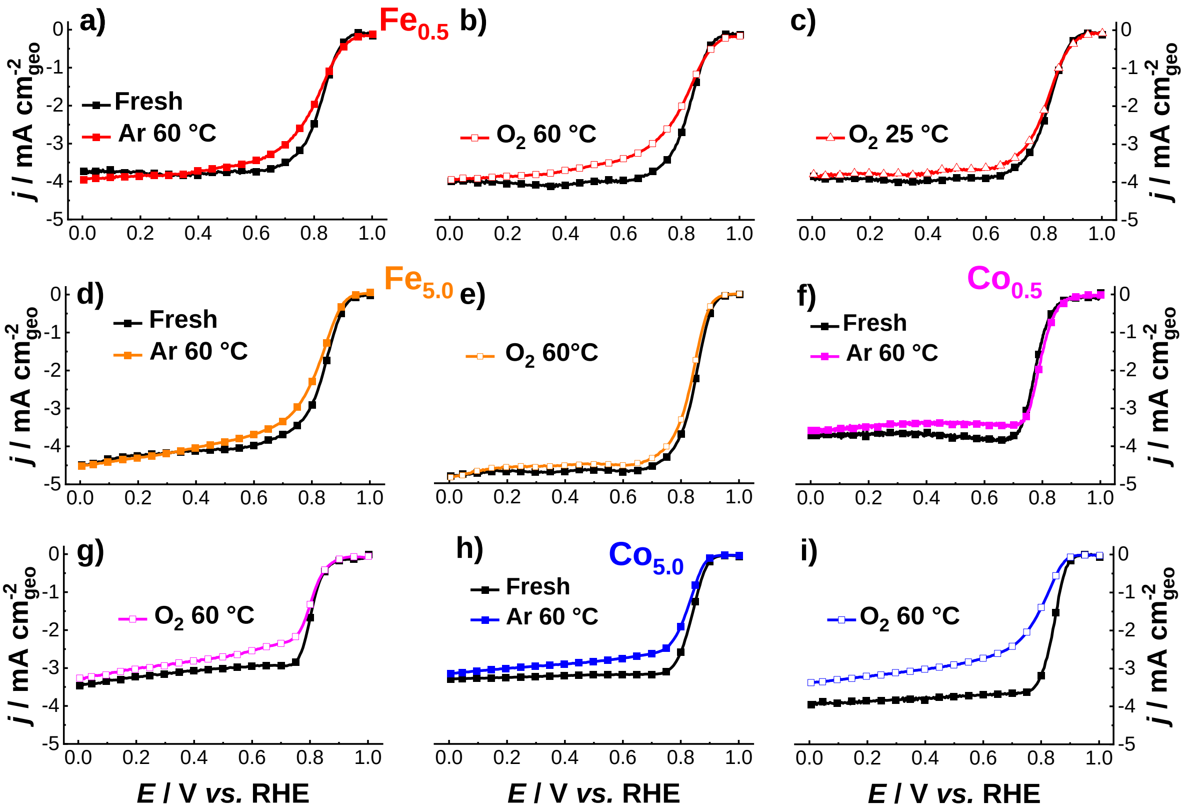

Figure A2.2. ORR polarization curves of the catalysts before and after 10,000 AST loading cycles under Ar-**(a, d, f, h)** and O$_2$-**(b, e, g, i)** saturated 0.1 mol L^{-1} NaOH electrolyte at 60 °C (also **(c)** at 25 °C and O$_2$ for Fe$_{0.5}$). The representative curves were obtained at 5 mV s^{-1}, 1600 rpm, O$_2$-purged electrolytes, 0.8 mg$_{powder}$ cm^{-2} and 25 °C.

Table A2.2. Summary of the results and errors of Metal-N-C catalysts before and after 10,000 AST loading cycles in Ar- and O_2-purged 0.1 mol L^{-1} NaOH electrolytes at 60 °C and 25 °C. The half-wave potential, Mass Activity (i_{MA}) at 0.85 V *vs.* RHE and Tafel slope (from 0.9 to 0.8 V). were obtained from O_2-saturated electrolyte, 5 mV s^{-1}, 1600 rpm, 0.8 mg cm_{powder}^{-2} and 25 °C

Catalyst	**Ageing conditions**	$E_{\text{half-wave}}$ **/ V**	i_{MA} **at 0.85 V / A** g_{powder}^{-1}	**Tafel slope / mV** dec^{-1}
$Fe_{0.5}$	Fresh	0.82 ± 0.01	2.576 ± 0.2785	79 ± 0.7
	Ar 60 °C	0.81 ± 0.01	2.200 ± 0.0645	93 ± 19.1
	O_2 60 °C	0.81 ± 0.01	2.128 ± 0.3741	107 ± 39.6
	O_2 25 °C	0.82 ± 0.01	2.323 ± 0.0612	88 ± 12.7
$Fe_{5.0}$	Fresh	0.85 ± 0.01	5.049 ± 0.9188	78 ± 1.4
	Ar 60 °C	0.83 ± 0.01	3.067 ± 1.0159	82 ± 5.0
	O_2 60 °C	0.84 ± 0.01	3.548 ± 0.0115	81 ± 3.5
$Co_{0.5}$	Fresh	0.80 ± 0.01	0.686 ± 0.0356	58 ± 3.1
	Ar 60 °C	0.79 ± 0.01	0.472 ± 0.0002	66 ± 10.6
	O_2 60 °C	0.80 ± 0.01	0.647 ± 0.0375	73 ± 21.2
$Co_{5.0}$	Fresh	0.84 ± 0.01	2.580 ± 0.4292	51 ± 0.9
	Ar 60 °C	0.83 ± 0.01	1.194 ± 0.1493	55 ± 5.0
	O_2 60 °C	0.81 ± 0.01	0.889 ± 0.0746	57 ± 8.5

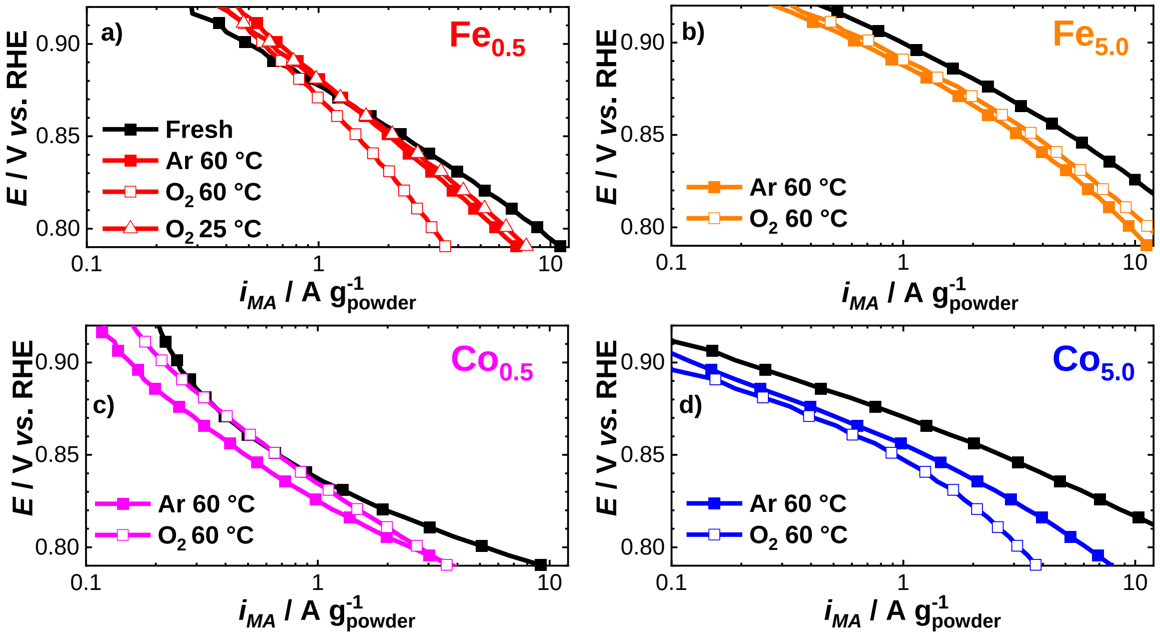

Figure A2.3. Mass-transport-corrected Tafel plots of the **(a)** $Fe_{0.5}$, **(b)** $Fe_{5.0}$, **(c)** $Co_{0.5}$ and **(d)** $Co_{5.0}$ catalysts before and after 10,000 AST loading cycles under Ar- and O_2-purged 0.1 mol L^{-1} NaOH at 60 °C (also in O_2 at 25 °C for $Fe_{0.5}$). The measurements were performed in O_2-saturated electrolyte at 5 mV s^{-1}, 1600 rpm, 0.8 mg_{powder} cm^{-2} and 25 °C.